Title
Hierarchical Material Architecture Design for Better Energy Storage

Author
Wang, Xiaolei

Publication Date
2013

Peer reviewed|Thesis/dissertation

UNIVERSITY OF CALIFORNIA
Los Angeles

Hierarchical Material Architecture Design for Better Energy Storage

A dissertation submitted in partial satisfaction of the
requirements for the degree Doctor of Philosophy
in Chemical Engineering

by

Xiaolei Wang

2013

ABSTRACT OF DISSERTATION

Hierarchical Material Architecture Design for Better Energy Storage

By

Xiaolei Wang

Doctor of Philosophy in Chemical Engineering

University of California, Los Angeles, 2013

Professor Yunfeng Lu, Chair

Human civilization has been driven by energy consumption. The rapid increase in energy consumption for past decades is leading to a fossil-fuel shortage and ecological deterioration. Facing these challenges, humankind has been diligently seeking clean, safe and renewable energy sources, such as solar, wind, waves and tides. At the same time, the search for strategies that can reduce fossil-fuel consumption and decrease CO_2 emission has become an essential endeavor. However, the energy harvested from renewable sources must be stored prior to its connection to electric grids or delivery to customers, and EVs need sufficient on-board power sources. These essential needs have made energy storage a critical component toward sustainable society.

Among all energy storage technologies, electrochemical energy storage within batteries or electrochemical capacitors (ECs) is the most promising approach, since as-stored chemical energy can be effectively delivered as electrical energy with cost effectiveness. However, the performance of current batteries and ECs has been constrained by electrode materials and other factors. The objective of this dissertation is to develop better energy storage materials through rational architecture design of the electrode materials and electrode architectures. To achieve this goal, this dissertation work focuses on the fabrication of multifunctional architectures by integrating active materials with highly conductive scaffolds, creating a new family of high-performance energy storage materials with desired properties.

Different types of energy storage architectures were investigated to demonstrate such design concept. First, Nb_2O_5 nanocrystals of low dimensions were synthesized, and Nb_2O_5/CNTs nanocomposite electrode architecture was designed and fabricated by a physically mixing method. Compared with pure Nb_2O_5 materials, such architecture could create more accessible outer surface, which is very important in fast lithium storage. Synergistic effects between Nb_2O_5 nanocrystals and CNTs resulted in an optimal composition with the highest storage performance. Second, for better electrode conductivity and stability, an *in-situ* intimate growth of Nb_2O_5 nanocrystals on the CNs framework was also developed. Compared with physically mixed composites, such an electrode architecture showed superior cycling stability, while remaining the excellent rate performance and high specific capacitance. Third, various architectures were designed and fabricated by directly coating thin film $LiMn_2O_4$ on conductive indium-tin-oxide (ITO) glass, and by conformably coating nanocrystals on pre-formed CNT papers. Last, electrode architecture obtained by integrating nanocrystals and highly conductive graphene sheets was also designed and fabricated through an aerosol-assisted process using $Li_4Ti_5O_{12}$ nanocrystals as a model system. The pomegranate-like architecture provides an electrode with outstanding rate capability, as well as good electrode stability. It was demonstrated that thick electrodes with high charge capacity, high rate performance and cycling stability rely on functional architecture that simultaneously provides high electronic conductivity,

easy ion diffusion, abundant surface active sites and robust structure and interfaces.

The general conclusion derived from these studies is that the energy storage performance of electrode materials can be significantly improved by constructing rational architectures that provide effective ion diffusion, good electronic conductivity, fast electrode reaction, robust structure and a stable interface, which normally cannot be obtained with conventional materials. This strategy also can be extended to other devices, such as batteries and fuel cells, providing a general design platform for high performance energy materials. Further exploration in this research direction will ultimately lead to high energy, high power, and long life energy storage devices for many applications, including portable electronics, EVs and grid-scale energy storage.

The dissertation of Xiaolei Wang is approved.

Qibing Pei

Selim Senkan

Harold Monbouquette

Yunfeng Lu, Committee Chair

University of California, Los Angeles

2013

TABLE OF CONTENTS

LIST OF FIGURES

ACKNOWLEDGEMENTS

It has been a really long time since I dreamed of today. This thesis records everything I have experienced in UCLA, the laughter and tears, the happiness and sorrows. With this opportunity, I would like to thank many individuals who have been helping me to accomplish this dissertation, and supporting me along the way.

First, I am deeply grateful to Dr. Yunfeng Lu, who has been my thesis advisor, guide and philosopher. This special day would not have come true without his strong support during the past more than five years. The dedicated and careful training I obtained from him in respect of fundamental knowledge and strategy in research and teaching, responsibility and attitudes in life has provided me with continual motivation and guidance to academic and professional success. I am indebted to him not only for the incredible research opportunity, but also for the chance of working with an advisor from whom I can follow and learn so much for my personal and professional development.

I also thank my doctoral committee members, Dr. Harold Monbouquette, Dr. Selim Senkan, and Dr. Qibing Pei for their support of my doctoral candidacy. Their insightful questions and discussions along the way have helped me a lot over the years. Moreover, I would like to give additional thanks to Dr. Selim Senkan for letting me use the instruments in his lab, and the great help and guidance in not only the research but also my career planning.

Thank all the previous and current group members and friends in UCLA for sharing with me their experience and knowledge, through which I have been occasionally able to either generate new ideas or expedite the progress of the whole work. Especially, thank Dr. Zhenglong Yang, Dr. Kun Huang, Dr. Qiangfeng Xiao, Dr. Daocheng Pan, Dr. Ming Yan for their

help and kind advice in the beginning of my PhD; thank Dr. Ding Weng, Dr. Chihning Pao, Dr. Kimberly Cross, Dr. Hiesang Sohn and Dr. Zheng Chen, Dr. Juanjuan Du for their help with my research and life in UCLA.

Also, I would like to thank all the professors and staffs in the department that have been so nice, helpful and supportive all the time. Special thanks to Dr. Yi Tang for his help and support for my life and career; to Professor Yoram Cohen, Professor Robert Hicks and Professor Tatianna Segura for their wonderful lectures; to John Berger, Miguel Perez and Alain C. De Vera for their always being so kind and patient to help me.

Finally, I am indebted to my parents; they have always been so supportive and encouraging. I am deeply grateful to them for their loving me so much and providing me such a great family, which provides me very important morals, values and philosophy. And specially, I would like to thank my wife Ge Li, who is always on my side no matter what happens. Your support and love drive me forward.

VITA

2007	B. S., Chemical Engineering Dalian University of Technology Dalian, Liaoning, P. R. China
2007	M. S., Chemical Engineering Tianjin University Tianjin, P. R. China
2009-2013	Teaching Assistant, Research Assistant Department of Chemical and Biomolecular Engineering University of California, Los Angeles, USA

PUBLICATIONS

1. **Xiaolei Wang**, Zheng Chen, Yunfeng Lu*, *In-Situ* Growth of Nb_2O_5 Nanocrystals on CNTs: A Novel Composite for Ultrafast Reversible Lithium Storage, *ready to submit*, **2013**.
2. **Xiaolei Wang**, Zheng Chen, Chao Lei, Yunfeng Lu*, Ultra-high Power Anode Material Based on Ultrafine $Li_4Ti_5O_{12}$ Nanocrystals, *ready to submit*, **2013**.
3. **Xiaolei Wang**, Zheng Chen, Yaochun Qin, Yunfeng Lu*, Ultrafine $LiMn_2O_4$ Nanocrystals as Building Blocks for High Power Lithium Battery Cathode, *ready to submit*, **2013**.
4. Zheng Chen, **Xiaolei Wang**, Huihui Zhou, Yang Liu, Yunfeng Lu*, High-Performance Pseudocapacitors Based on Carbon-Nanotube-Threaded Nanocrystal Assembling Architecture, *Advanced Materials*, *accepted*, **2013**.
5. **Xiaolei Wang**, Ge Li, Xueming Ma, Yunfeng Lu*, Tetragonal $VNb_9O_{24.9}$-based Nanorods: A Novel Form of Lithium Battery Anode with Superior Cyclability, *ready to submit*, **2013**.
6. Ge Li[§], **Xiaolei Wang**[§],(***equal contribution***) Zheng Chen, Xueming Ma*, Yunfeng Lu*, Characterization of Niobium and Vanadium Oxide Nanocomposites with Improved Rate Performance and Cycling Stablility, *Electrochimica Acta*, **2013**, *102,* 351-357.
7. Ge Li, **Xiaolei Wang***, Xueming Ma, Nb_2O_5-Carbon Core-Shell Nanocomposite as Anode Material for Lithium Ion Battery, *Journal of Energy Chemistry*, **2012**, *accepted*.
8. Xilai Jia, Zheng Chen, Yiting Peng, **Xiaolei Wang**, Fei Wei*, Yunfeng Lu*, Building Robust Architectures of Carbon and Metal Oxide Nanocrystals towards High-Performance Anodes for Lithium Ion Batteries, *ACS Nano*, **2012**, *6*(11), 9911-9919.
9. Zheng Chen, **Xiaolei Wang**, Xilai Jia, Fei Wei, Yunfeng Lu, High-Performance Energy Storage Architectures from Carbon Nanotubes and Nanocrystal Building Blocks, *Advanced*

Materials, **2012**, *24*(15), 2030-2036.

10. Zheng Chen, Ding Weng, **Xiaolei Wang**, Yanhua Cheng, Ge Wang, Yunfeng Lu*, Ready fabrication of thin-film electrodes from building nanocrystals for micro-supercapacitors, *Chemical Communications*, **2012**, *48*, 3736-3738.
11. Xilai Jia, Zheng Chen, Arnold Suwarnasarn, **Xiaolei Wang**, Hiesang Sohn, Qiang Zhang, Benjamin M. Wu, Fei Wei, Yunfeng Lu*, High-performance flexible lithium-ion electrodes based on robust network architecture, Energy and Environmental Science, **2012**, *5*, 6845-6849.
12. **Xiaolei Wang**, Ge Li, Zheng Chen, Veronica Augustyn, Xueming, Ma, Ge Wang, Bruce Dunn, Yunfeng Lu*, High-Performance Supercapacitors Based on CNT/Nb_2O_5 Nanocomposites, *Advanced Energy Materials*, **2011**, *1*(6), 1089-1093.
13. **Xiaolei Wang**, Daocheng Pan, Ding Weng, Chen-Yian Low, Lynn Rice, Jinyu Han, Yunfeng Lu*, A General Synthesis of Cu−In−S Based Multicomponent Solid-Solution Nanocrystals with Tunable Band Gap, Size, and Structure, *The Journal of Physical Chemistry C*, **2010**, *114*(41), 17293-17297.
14. Zheng Chen, Yaochun Qin, Ding Weng, Qiangfeng Xiao, Yiting Peng, **Xiaolei Wang**, Hexing Li, Fei Wei, Yunfeng Lu*, Design and Synthesis of Hierarchical Nanowire Composites for Electrochemical Energy Storage, Advanced Functional Materials, **2009**, *19*(21), 3420-3426.
15. Daocheng Pan, **Xiaolei Wang**, Z. Hong Zhou, Wei Chen, Chuanlai Xu and Yunfeng Lu*, Synthesis of Quaternary Semiconductor Nanocrystals with Tunable Band Gaps, *Chemistry of Materials*, **2009**, *21*(12), 2489-2493.
16. Daocheng Pan, Ding Weng, **Xiaolei Wang**, Qiangfeng Xiao, Wei Chen, Chuanlai

Xu, Zhengzhong Yang, Yunfeng Lu*, Alloyed semiconductor nanocrystals with broad tunable band gaps, *Chemical Communications*, **2009**, *0*, 4221-4223.

17. **Xiaolei Wang**, Jinyu Han, Hua Wang*, Preparation of Lactide Using Ionic Liquid Catalyst, *Journal of Chemical Industry and Engineering*, **2007**, *58*(12), 4-8

1. Introduction

1.1. Background

Nature and human society are driven by energy. The evolution of an ecosystem is supported by chemical energy stored in organic compounds such as carbohydrates, fats and proteins that are converted from sunlight by autotrophs (e.g. plants and algae).[1] Similarly, human activity and society development rely on chemical energy stored in food and electrical energy produced from fossil fuels (e.g. oil, coal and gas). To continue human civilization requires abundant and sustainable supply of energy. During the past decades, global energy consumption has been booming with steadily increased standard of living and quality of civilization. Rapidly increased energy consumption, however, has inevitably resulted in fossil-fuel shortage and ecological deterioration.[2, 3] Facing these challenges, humankind has been diligently seeking for alternative energy sources to offset the diminishing availability or to take place of fossil fuels (**Figure 1.1**), and at the same time, seeking for strategies to increase the efficiency of energy use.[4, 5]

In the respect of alternative sources, biomass conversion may be a potential way to produce high-quality energy (e.g. alcohol, bio-diesel) from renewable sources, such as wood, sugar canes and crop residues. However, growth of biomass decreases total size of fertile land for crops and timber, raising the price of food and wood products. Moreover, to convert and collect biomass energy consumes too much energy and causes serious pollutions.[6-8] Hydropower is an economically effective energy source but it requires building huge dams at locations where special geological conditions have to be met.[9] Electricity produced from nuclear fission has been increasing in the past three decades, but recent failure of Fukushima Daiichi nuclear power plant caused by 2011 Tohoku earthquake in Japan has re-drawn a great concern about nuclear security.[10]

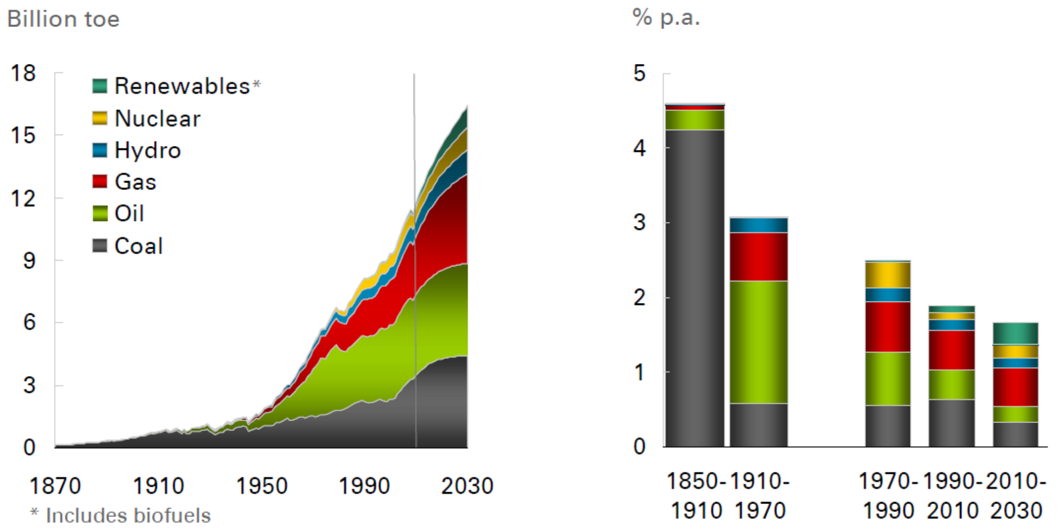

Figure 1.1 World commercial energy use (left) and contribution of each source to total energy growth (right). [4] (toe: term of oil equivalent)

In this context, clean, safe and renewable sources such as solar radiation, wind, waves and tides are considered as more promising sources for energy production.[11] As predicted, increase of renewable energy will be a leading factor contributing to total energy growth by 2030 (**Figure 1.1**). However, these energies are variable with time and diffused in space. The energy harvested from these sources is in such intermittent nature and that must be stored prior to its connection to electric grids or delivery to customers. This requirement has drawn a huge demand for effective energy storage.

On the other hand, to increase the efficiency of energy use, a key step is to replace the current petroleum-based transportation infrastructure by electric transportation.[12, 13] Since energy conversion efficiency of electric motors is 4 to 5 times higher than that of normal engines (90% *vs*. 20%), the net energy consumption and CO_2 production from electric vehicles (EVs) is typically less than one-half of that from traditional vehicles.[14] Moreover, the electricity used to power electrical vehicles (EVs) can be produced from various renewable sources instead of fossil-fuel power plant, which further reduces the use of fossil fuels. However, widespread implementation of EVs also relies on successful on-board rechargeable electricity storage. In addition, other emerging applications such as advanced portable electronics and smart grids demand effective energy storage devices and systems.[3] These growing needs have made energy storage an essential component of creating sustainable society.

1.2. Energy Storage Technologies

Our ancestors used fire wood and charcoal with stored chemical energy to light, cook food and make bronze wares, which created ancient civilization, while modern industries requires more complex and high-performance energy storage technologies. To date, various advanced strategies have been proposed for energy storage,[15, 16] including mechanical energy storage, electrostatic energy storage, hydrogen (H_2)-based chemical energy storage, and electrochemical energy storage. They favor different applications due to their individual characteristics.

Typical mechanical energy storage includes flywheel storage and compressed air storage. Flywheels use vacuum-housed high-speed rotor to reversibly convert electrical energy to kinetic energy; the flywheel's rotational speed is reduced or increased as electrical energy is generated or added.[17, 18] Common spinning speeds are in the range of 20,000 to over 50,000 rotations per minute.[19] The energy density (energy stored per unit mass or volume) is proportional to the mass and the square of the angular velocity of the rotor, the lighter the rotor and the higher the spinning speed, the higher the energy density. To reach high speed, light and high-strength materials such as polymer-reinforced composites are used. Typical energy density may reach 100-130 Wh/kg based on the mass of rotor, while it decreases to ~10 Wh/kg if the whole heavy container is considered. This technology shows advantages of wide range of operation temperatures, high round-trip efficiency and long services life, but is limited by fast energy loss and potential safety issue from shattering.[20] On the other hand, compressed air energy storage is based on compression and expansion of gas to store or release kinetic energy, which is driven by turbo compressor or drives air engine to produce electricity.[21] It is only suitable for storage of a large amount of off-peak electric power when large cavern is available. For vehicle applications, this technology is constrained by low energy density, low efficiency, high-cost vessels and safety concern.[22]

Electrostatic energy storage using dielectrical capacitors shows high frequency response, but can only store a small amount of energy.[23] Therefore, they are only used in small electronics. Using polarized polymers may significantly improve the energy density, but it is too low to be used in large-scale storage.[24]

H_2-based chemical energy storage was considered as a critical technology to develop hydrogen economy. [25] For example, to develop H_2-powered fuel cells for vehicles and other applications. However, after almost two decades' effort, there has been no successful strategy to store H_2 with a capacity, cost and operation condition that can meet general applications.[26]

1.3. Electrochemical Energy Storage

Among all energy storage endeavors, converting electrical energy into chemical energy stored within batteries or electrochemical capacitors (ECs) is probably the most promising approach, since as-stored chemical energy can be effectively delivered as electrical energy with a diversity of energy density and power density (power delivered per unit mass or volume), high efficiency, long service life, effective cost and environmental benignity.[3, 27, 28] Furthermore, batteries and ECs can be highly portable, enabling their broad use in portable electronics, electric vehicles, and other applications. Effectively assembling battery or EC stacks can easily create large-scale energy storage systems for utility applications. In fact, rapid market growth for portable electronics, electric vehicles and grid storage has placed high-performance batteries and ECs at the forefront of technical innovation.

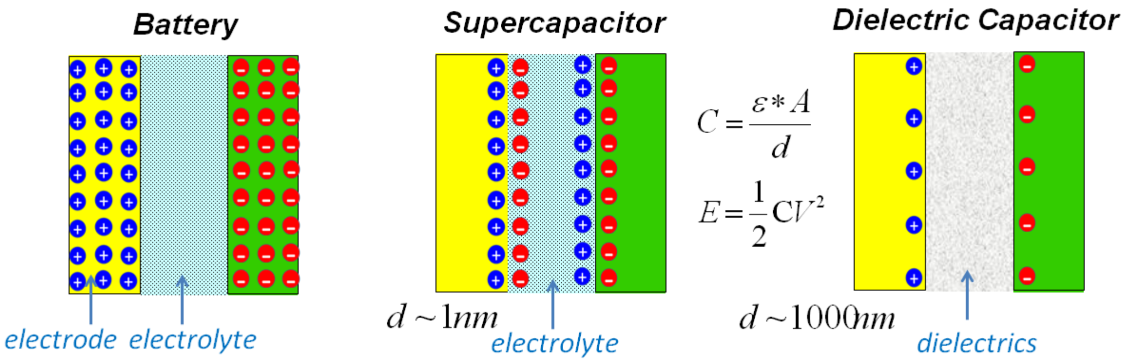

Figure 1.2 Simplified models of different energy storage devices.

The performance of these devices is determined by their structure and storage features. A simple comparison is presented in **Figure 1.2** where simplified device models are presented. Batteries can store a lot of energy using their whole electrode active materials where chemical reactions take place through the bulk of electrodes. ECs, called supercapacitors, store charge on the surface of their electrodes. Chemical or physical processes occur on the interface between electrode and electrolyte, so the total charge is smaller. But according to the equation ($C=\varepsilon*A/d$), since the distance (d) between this two surfaces is in the range of 1 nm, the energy density is still significant. Capacitors use dielectrics which generally have length scale of ~1000 nm; therefore the capacitance and energy density are very low. Therefore, capacitors are not used for major power sources in electronic devices.

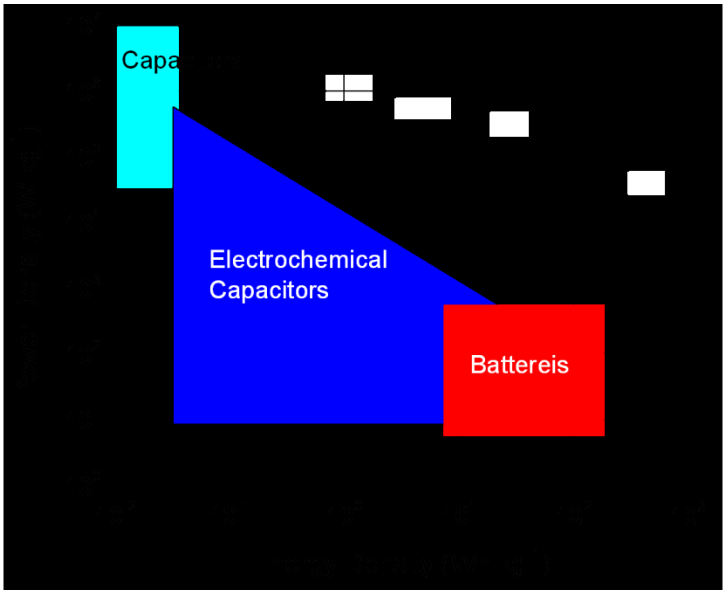

Figure 1.3 A general plot of power density against energy density for capacitors, electrochemical capacitors and batteries.

Generally, energy density and power density are used to quantify the performance of batteries and ECs. **Figure 1.3** shows a plot of power density versus energy density, also called a Ragone plot, for capacitors, ECs and batteries.[29] As illustrated, batteries, which operate based on redox reactions between their cathodes and anodes, offer high energy density but low power density. These features allow them to be used in ordinary electronics where energy density is of primary concern. Capacitors, on the other hand, which are operated based on charge accumulation on parallel electrodes separated by dielectrics, offer much higher power density but much lower energy density. In the aspect of lifetime, capacitors exhibit dramatically longer lifetimes (e.g., > 1,000,000 cycles) than batteries (e.g., 1,000 cycles).[3, 27]

ECs exhibit storage performance intermediate that of capacitors and batteries. They are generally operated based on electrical double-layer capacitance or pseudocapacitance, and are referred to electrical double-layer capacitor (EDLC) and pseudocapacitor, respectively. Supercapacitors can deliver at least 1,000 times more energy than dielectric capacitors and 10 times more power than batteries. In addition, they often exhibit long cycling lives of over

500,000 cycles. Such superior performance is essential for various applications where fast charging, high power and long cycling life are required. Typical applications include energy recovery, energy harvesting from intermittent power sources, back-up power supply, heavy-duty loading and uninterruptible power supplies.[30]

1.3.1. Rechargeable Batteries

Rechargeable batteries can be divided into different categories according to their electrode materials, and mainly include lead-acid, nickel-cadmium, nickel-metal hydride and lithium-ion batteries.[31] Currently, lithium-ion batteries are the most widely used rechargeable batteries due to their high energy density, high cell voltage, low self-discharge, long cycling life and absence of memory effect. To illustrate the working principle of rechargeable batteries, we use lithium-ion battery as an example **(Figure 1.4)**. Such a device contains a cathode and an anode, which are separated and soaked in an electrolyte. The energy is stored by reversible chemical reaction. During a discharge process, lithium ions are extracted from anode materials, such as graphite, and electrons are released at the same time. The electrons are driven to the cathode through external circuit. Lithium-ions diffuse from anode into the cathode through internal circuit (or electrolyte), and then react with cathode materials by combining electrons. As a result, the cell voltage decreases and energy is released. Reverse reactions take place during a charge process. So it can be determined that the following key processes take place in a battery process: 1) ion transport and diffusion; 2) electron transfer and 3) chemical reactions in solid-phase and on electrode/electrolyte interfaces. These complicated processes make the charge storage kinetics to be very slow.

Anode materials used for current commercial lithium-ion battery are mainly graphite, which can take a large amount of lithium ions in the form of LiC_6, of which the theoretical lithium storage capacity is 372 mAh/g. Cathode materials are dominated by lithium metal oxide such as $LiCoO_2$ and $LiMn_2O_4$, which give a lithium capacity of 120-150 mAh/g. Such combination leads to an energy density of 500-600 Wh/kg based on electrode materials or 100-150 Wh/kg if considering the whole device package.[32]

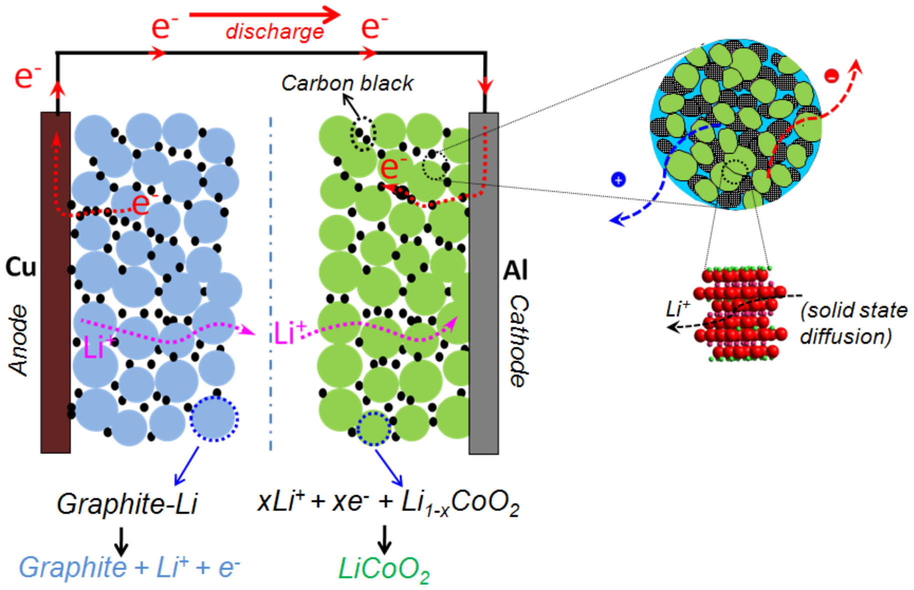

Figure 1.4 Operation principle of a lithium-ion battery (illustrated with a discharging process)

1.3.2. Electrical Double-Layer Capacitors (EDLCs)

For EDLCs, the device structure is similar to that of batteries; there are also two electrodes (a positive and a negative), a separator and electrolyte filled inside the cell, as shown in **Figure 1.4**. The energy storage is based on physical separation and accumulation of charged ions on the electrode/electrolyte interface. Porous materials (such as activated carbon) are normally used to provide large interface for more charge storage. During a charge process, negatively charged ion move to positive side and form a double layer, and electrons move through the external circuit to negative electrode, where positively charged ions are accumulated over there (**Figure 1.5**).[27, 29, 30] As a result, the cell voltage increases and energy is stored. The most critical process that might limit the storage performance is ion transport. Since the electrode capacitance is independent with potential, a linear charge/discharge curve is obtained. Current commercial EDLCs use organic electrolyte and porous carbon electrode which can provide a capacitance of 100-150 F/g.[33, 34]

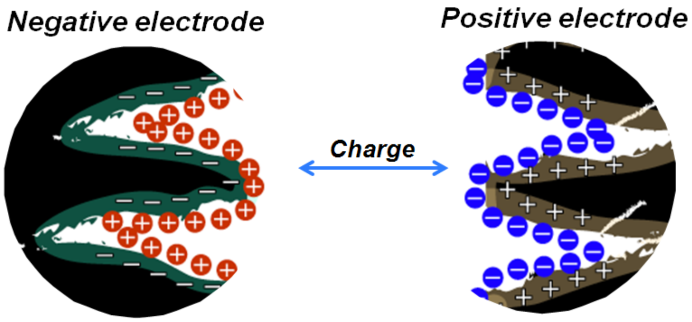

Figure 1.5 Working principle of EDLCs (illustrated with a charging process)

1.3.3. Pseudocapacitors

The other type of supercapacitor is pseudocapacitors, which store energy by fast faradic reactions. In these devices, the ions and electrons move in the same manner with EDLCs, but instead of forming double-layer on the electrode/electrolyte interface, redox reactions take place on the surface or near the surface of the electrodes (**Figure 1.6**).[27, 29, 30] Energy is also stored by chemical reaction which is similar to battery, but the reaction would only involve just the first a few or tens of nanometers of the electrode material and the process is free of solid-state diffusion and phase change, which is similar to EDLCs. The most critical process that might limit the storage performance is ion transport and charge transfer. The best pseudocapacitor materials ($RuO_2\ x H_2O$) so far can provide a capacitance of over 1000F/g.[35] It can be seen that the major electrode process of supercapacitors is ion transport and diffusion; pseudocapacitors have fast charge transfer and surface reactions, which enable fast charge/discharge and high power density.

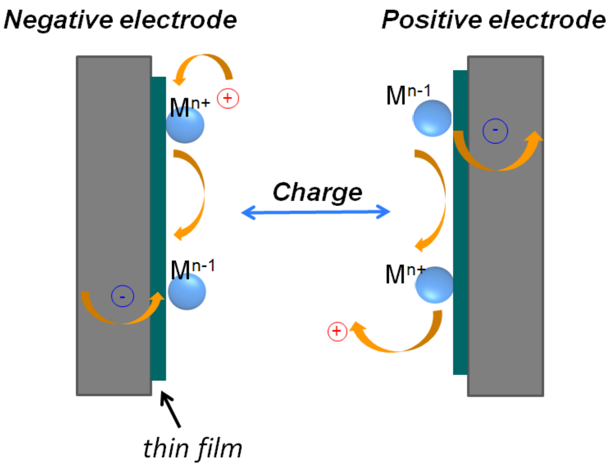

Figure 1.6 Working principle of pseudocapacitors (illustrated with a charging process).

1.4. Development of Electrochemical Energy Storage Materials

1.4.1. Carbon (EDLC) Materials

Conventionally, EDLC utilizes activated carbon as the electrode material; their capacitance comes purely from the electrostatic charge accumulated at the electrode/electrolyte interface. The energy density of an EDLC depends on the surface area of the electrode material that is accessible to electrolyte ions which form electrical double layers at electrode/electrolyte interface.[36, 37] To date, the most advanced EDLCs based on activated carbons may provide capacitance of up to 150 F g^{-1} in organic electrolyte or 250 F g^{-1} in aqueous electrolyte, which approximately corresponds to energy densities of 35 and 8 Wh kg^{-1} (based on the weight of active materials for all energy and power densities hereinafter), respectively.[33, 34, 38] Such energy densities are significantly higher than those of dielectric-based capacitors (e.g., 10^{-2} Wh kg^{-1} for the best tantalum capacitors); however, they are much less than those of batteries (~ 100-150 Wh kg^{-1}).[32] Nevertheless, EDLCs are operated based on electrostatic charge accumulation, which allows rapid charge and discharge with high power density (e.g., 5 kW kg^{-1} at energy density of 5 Wh kg^{-1}).[39]

Towards better EDLCs, various carbon materials have been explored, including activated carbons,[40] carbon nanotubes (CNTs),[41] graphene,[42] templated carbons[43] and carbon aerogels.[44] These efforts have been focused on optimizing the materials' pore structure to enable faster ion transport and to increase their effective surface area. Electrical double layers can be readily formed on CNTs; however, capacitance of CNTs is generally low due to low surface area.[45] Graphene may provide higher surface area; however, it tends to form stacking structure with reduced surface area. Recently, activated graphene with high surface area was reported with capacitance as high as 170 F g^{-1} in organic electrolyte, which is the highest capacitance ever obtained from carbon materials.[34] Compared to activated carbons that are low cost but have less controlled pore structure, templated carbons were synthesized with well-controlled pore structure. The highest capacitance achieved for templated carbons, however, is still less than 120 F g^{-1} in organic electrolyte[43] or 250 F g^{-1} in aqueous electrolyte.[38]

In addition, extensive efforts have also been devoted to developing better organic electrolytes with wider voltage windows and lower ion-transport resistance, since the energy density of EDLCs is proportional to the square of the cell voltage. However, implementation of such electrolytes also requires the fabrication of high-purity carbon materials in order to avoid side reactions occurring at high voltage.[46] In short, despite the extensive efforts made, advances in the field of EDLCs have been quite limited.

1.4.2. Redox-Active Materials (Batteries and Pseudocapacitors)

Batteries and pseudocapacitors share similar characteristics in terms of active materials, device structures and operations. A pseudocapacitor is similar to a high-power thin-film battery. Normally, battery charge/discharge processes show slow solid-state diffusions and may involve tedious bulk reaction and unfavorable phase transformation, which limits the rate capability and charge/discharge life (cycling life). Nevertheless, by decreasing the size or increasing the porosity, battery electrodes may show significantly increased surface-area, which enables enhanced charge storage from surface redox reactions. If suitable electronic conductivity and structure/interface stability can be reached, these materials may be charged and discharged at increased rates, which is similar to pseudocapacitors. In this context, materials used for battery electrode can be also potential candidates for pseudocapacitors. One of the major efforts of my PhD research is to design high-performance materials architectures that could enable traditional redox materials with high capacity, high rate and long cycling life, through improving pseudocapacitive charge storage. In this dissertation, I will discuss all redox materials with a purpose of pseudocapacitor application, though some of them may be considered as conventional battery materials.

Pseudocapacitors rely on fast reversible faradic processes occurring on the surface of sub-surface of redox-active materials such as conductive polymers and metal oxides. Pseudocapacitance arises due to thermodynamic consideration between the charge acceptance (Δq) and the change in voltage ($\Delta\upsilon$), where the derivative ($d\mathrm{q}/d\upsilon$) corresponds to the pseudocapacitance.[47] Compared to carbon materials, metal oxides may offer significantly higher capacitances. For example, hydrous ruthenium oxide ($RuO_2{\cdot}xH_2O$) has a specific capacitance of over 720 F g^{-1} in 1 V acidic electrolytes owning to its excellent proton and electron conduction.[35] Transition metal oxides (e.g., MnO_2,[48] Co_3O_4,[49] TiO_2,[50] MoO_3[51] and Nb_2O_5[52]) also possess theoretical capacitances of up to 1000 F g^{-1}; however, the electrodes made from these oxides generally exhibit very low energy and power densities due to poor ionic and electronic conductivity. To circumvent this barrier, pseudocapacitors are generally prepared from thin-film electrodes or composite electrodes as detailed below.

Thin-Film Pseudocapacitors: To minimize ionic and electronic transport resistance, oxide thin films with thickness of nanometers to hundreds of nanometers were deposited on conductive substrates, exhibiting high gravimetric capacitances and high power.[50, 51, 53, 54] However, their performance decreases rapidly with increasing electrode thickness. With limited thickness, mass loading of active materials, and hence energy density, is extremely low, which precludes their practical application.[55] Recently, thin-film pseudocapacitors were made by coating oxides onto porous conductive substrates such as gold[56] and nickel;[57] their mass loading was improved to some degree but is still too low for actual application.

Composited Pseudocapacitors: To increase mass loading, composite electrodes were fabricated by introducing conductive agents, such as carbon black,[58, 59] graphene[60, 61] and CNTs.[62, 63] Such electrodes can be classified into two categories. The first category was made by coating physical mixtures of active materials, polymeric binders, and conductive agents onto the current collectors. This method is simple, however, such electrodes generally exhibit mediocre storage performance. For example, MnO_2-based electrodes made with 30 wt-% acetylene black exhibit a capacitance of 228 F g^{-1} at a rate of 10 mV s^{-1}, which is significantly lower than the theoretical value of MnO_2.[58] Such mediocre performance can be attributed to poor electrode-structure control, in particular, poor control over the interfaces between active materials and conductive agents.

The second category of pseudocapacitors was made from nanocomposites of oxides and CNTs or graphene. Graphene and CNTs are lightweight and highly conductive materials with large open surface, excellent mechanical strength, and high chemical/electrochemical stability, and have been extensively used to form various nanocomposites. To form the nanocomposites, active materials were deposited on graphene[60, 61, 64] or CNTs[62, 63, 65] or within graphene layers or CNT networks though various techniques, such as sol-gel processing,[66] electrophoresis,[67] electrochemical deposition,[68, 69] electroless deposition,[62, 70] hydrothermal reaction[71, 72] and thermal evaporation.[73] Such nanocomposites possess well-controlled structure and interfaces, making the fabrication of high-performance pseudocapacitors possible. However, many of the nanocomposites reported are based on SnO_2,[64, 65] Fe_3O_4,[74] Mn_3O_4[72] and other high capacitive materials,[75] where charge storage is based on conversion reactions in organic electrolytes. These nanocomposites exhibited impressive capacity of up to 1000 mAh g^{-1}, but at extremely slow charge/discharge rates (a few hours) and at low working potentials. Their tendency to form solid-electrolyte-interface (SEI) layers, as well as their phase transitions and large volume changes during charge and discharge, results in electrodes with short cycling life (e.g., < 100 cycles) and reduced efficiency.[76] In this context, such nanocomposites are more suitable for batteries rather than for supercapacitors where high power, high efficiency and long cycle life are required.

Finding other oxide nanocomposites, which don't form the SEI layers or undergo significant structural and volume changes during charge/discharge, is essential towards the development of high-performance pseudocapacitors. To date, nanocomposites of MnO_2,[60] Co_3O_4,[77] NiO[78] and RuO_2[79]aqueous electrolyte were extensively studied. RuO_2-based nanocomposites exhibit notably good performance; however, their high cost forbids their large-scale application. Nanocomposites based on Co_3O_4 and NiO may provide capacitances of over 1000 F g^{-1} in alkaline electrolytes, but their narrow voltage window (~ 0.3 V) results in low energy density. MnO_2 is low cost, abundant and environmentally benign; however, nanocomposites based on MnO_2 generally exhibit low capacitances of less than 300 F g^{-1}. Adapting organic electrolytes with wider voltage windows may give high energy density, but even then, such nanocomposites would be still limited by their poor cycling stability.

1.5. Design Criteria and Needs for Electrochemical Energy Storage Materials

As mentioned above, batteries and ECs share similar characteristics in terms of active materials, device structures and operations; energy is stored or liberated through reversible redox reactions occurring in two electrodes, which are accompanied by shuttling of ions and electrons between the cathodes and anodes. Therefore, to realize high energy and power densities, sufficient number of ions and electrons need to be rapidly shuttled between the two electrodes. To obtain long cycling life, the electrodes and device structure must keep stable during charge/discharge cycling. These principles imply that high-performance electrodes and devices should meet the following criteria: 1) Large amount of installed active materials for high energy capacity; 2) Rapid transport of ions and electrons; 3) Facile electrochemical reactions on surface and in the bulk of electrodes; 4) Mechanically robust electrode architecture and chemically stable electrode/electrolyte interface. However, none of the existing single materials can meet all these criteria. Typical porous carbon materials show insufficient charge storage density; oxide and phosphate materials usually have low electron conductivity and low ion mobility; and most oxides have poor structure stability. These issues restrain the performance of current energy storage devices. Therefore, the seeking for high performance material architectures to circumvent these issues is highly demanded.

1.6. Thesis Objective and Research Scope

The objective of my dissertation is to address the limitation of current energy storage materials by rational structure design according to the above principles and criteria. The ultimate goal of this research is to develop high energy, high power, low cost and long life electrochemical energy storage devices for various applications, including portable electronics, EVs and grid-scale energy storage. To achieve this goal, my research strategy is to design and fabricate multifunctional architectures by integrating distinct material structures and properties to address the limitation of traditional materials and create a new family of high-performance energy materials with desired properties. Generally, my dissertation is dedicated to the following aspects: 1) understanding of novel charge storage behavior at nanoscale electrochemical interfaces, 2) design and efficient fabrication of new nano-architectured materials with tunable functionality and 3) integration of these materials into electrochemical devices and studying their performance to further guide the materials design.

Specifically, this dissertation includes the following research directions:

High-performance CNTs/Nb_2O_5 nanocomposites electrodes for asymmetric supercapacitors:

Nb_2O_5nanocrystals with low dimensions were synthesized, and Nb_2O_5/CNTs nanocomposites electrode architecture was designed and fabricated by a physically mixing method. By comparison with pure Nb_2O_5 materials, it was found that such architecture could create more accessible outer surface, which was very important in fast lithium storage. Synergistic effects obtained between Nb_2O_5 nanocrystals and CNTs resulted in an optimal composition with the highest storage performance. Secondly, to eliminate the contact resistance resulting from aggregation of nanocrystals and to further enhancing the electrode stability, an *in-situ* growth of Nb_2O_5 nanocrystals on the CNTs framework was also developed to ensure the intimate contact between the two components. Compared with physically mixed composites electrode, such an electrode architecture showed superior cycling stability, while the excellent rate performance and high specific capacitance remained.

High-performance electrodes architectures based on ultrafine nanocrystals and CNTs networks:

Two types of architectures were designed and fabricated using ultrafine $LiMn_2O_4$ nanocrystals as a model system. Electrodes were fabricated by directly coating thin film $LiMn_2O_4$ on conductive Indium-Tin-Oxide (ITO) glass, and by conformably coating nanocrystals on pre-formed CNT papers.

High-performance electrodes architectures based on ultrafine nanocrystals and graphene:

Electrode architecture obtained by integrating nanocrystals and highly conductive graphene sheets was also designed and fabricated through an aerosol-assisted process using $Li_4Ti_5O_{12}$ nanocrystals as a model system. Charge storage capacity, rate performance and cycling stability were compared and pseudocapacitive storage was investigated.

1.7. References

[1] http://en.wikipedia.org/wiki/Autotroph

[2] Armand, M.; Tarascon, J. M., Building better batteries. *Nature* **2008,** 451 (7179), 652-657.

[3] Simon, P.; Gogotsi, Y., Materials for electrochemical capacitors. *Nat Mater* **2008,** 7 (11), 845-854.

[4] BP Energy Outlook 2030, London, United Kingdom, January **2011**.

[5] BP Statistical Review of World Energy, London, United Kingdom, June **2012**.

[6] A. Demirbas, Biomass resource facilities and biomass conversion processing for fuels and chemicals, *Energy Conversion and Management* **2001**, 42(11), 1357-1378.

[7] M. F. Demirbas, M. Balat, H. Balat, Potential contribution of biomass to the sustainable energy development, *Energy Conversion and Management* **2009**, 50(7), 1746-1760.

[8] http://www.altenergy.org/renewables/biomass.html.

[9] http://www.eere.energy.gov/basics/renewable_energy/hydropower.html.

[10] http://en.wikipedia.org/wiki/Fukushima_Daiichi_Nuclear_Power_Plant.

[11] Top 5 Renewable Energy Sources of 2012, www.greenerideal.com.

[12] A. Faiz, C. S. Weaver, M. P. Walsh, Air Pollution from Motor Vehicles: Standards and Technologies for Controlling Emissions, **1996**, The World Bank, Washington, D. C.

[13] Electric car boom-Fiji Times Online, Fijitimes.com, March 4, **2010**.

[14] California Energy Commission's Demonstration of Neighborhood Electric Vehicles Consultant Report P600-02-020F, July 1, **2002**.

[15] Jensen, J.; Sorensen, B., Fundamentals of energy storage. *John Wiley and Sons, Inc.,New York, NY, USA* **1984**.

[16] Liu, C.; Li, F.; Ma, L.-P.; Cheng, H.-M., Advanced Materials for Energy Storage. *Advanced Materials* **2010,** 22 (8), E28-E62.

[17] S. Miller, Flywheel Fundamentals, *Environmental Science and Technology* **1994**, 28(2), 62A.

[18] B. Bolund, H. Bernhoff, M. Leijon, Flywheel energy and power storage systems, *Renewable and Sustainable Energy Reviews* **2007**, 11, 235-258.

[19] Davide Castelvecchi, Spinning into control: High-tech reincarnations of an ancient way of storing energy, *Science News* **2007**, 171(20), 312-313.

[20] http://en.wikipedia.org/wiki/Flywheel.

[21] S. J. Bauer, K. N. Gaither, S. S. Webb, C. Nelson, Compressed Air Energy Storage in Hard Rock Feasibility Study, Sandia Report, SAND2012-0540, February, **2012**.

[22] Distributed Energy Program: Compressed Air Energy Storage, United States Department of Energy, August **2006**.

[23] R. C. Dorf, J. A Svoboda, *Introduction to Electric Circuits* (5th ed.). *John Wiley and Sons, Inc., New York, NY, USA* **2001**.

[24] X. N. Xie, K. L. Lee, J. Z. Wang, K. P. Loh, Polarizable energy-storage membrane based on ionic condensation and decondensation, *Energy and Environmental Science* **2011**, 4, 3960-3965.

[25] J. Rifkin, The hydrogen Economy, *Tarcher/Putnam, Penguin Group Inc., New York, NY, USA* **2002**.

[26] Yang R. T.; Wang Y. H. Catalyzed Hydrogen Spillover for Hydrogen Storage *J. Am. Chem. Soc.* **2009**, 131, 4224–4226.

[27] Winter, M.; Brodd, R. J., What Are Batteries, Fuel Cells, and Supercapacitors? *Chemical Reviews* **2004,** 104, (10), 4245-4270.

[28] Ibrahim, H.; Ilinca, A.; Perron, J., Energy storage systems—Characteristics and comparisons. *Renewable and Sustainable Energy Reviews* **2008,** 12, (5), 1221-1250.

[29] Kötz, R.; Carlen, M., Principles and applications of electrochemical capacitors. *Electrochimica Acta* **2000,** 45, (15-16), 2483-2498.

[30] John R. Miller, A. F. B., Electrochemical Capacitors: Challenges and Opportunities for Real-World Applications. *The Electrochemical Society Interface* **2008**, 53-57.

[31] T. B. Reddy, Linden's Handbook of Batteries, 4th Edition, The McGraw-Hill, Inc., *New York, NY, USA,* USA 2011.

[32] Rechargeable Li-ion OEM Battery Products, Panasonic.com, April 23, **2010**.

[33] J. Chmiola, G. Yushin, Y. Gogotsi, C. Portet, P. Simon, P. L. Taberna, *Science* **2006**, *313*, 1760.

[34] Y. Zhu, S. Murali, M. D. Stoller, K. J. Ganesh, W. Cai, P. J. Ferreira, A. Pirkle, R. M. Wallace, K. A. Cychosz, M. Thommes, D. Su, E. A. Stach, R. S. Ruoff, *Science* **2011**, *14*, B70.

[35] Zheng, J. P.; Cygan, P. J.; Jow, T. R., Hydrous Ruthenium Oxide as an Electrode Material for Electrochemical Capacitors. *Journal of The Electrochemical Society* **1995,** 142, (8), 2699-2703.

[36] Liu, H.; Zhu, G., The electrochemical capacitance of nanoporous carbons in aqueous and ionic liquids. *Journal of Power Sources* **2007,** 171, (2), 1054-1061.

[37] Frackowiak, E., Carbon materials for supercapacitor application. *Phys. Chem. Chem. Phys.* **2007,** 9, 1774-1785.

[38] A. Kajdos, A. Kvit, F. Jones, J. Jagiello, G. Yushin, *Journal of the American Chemical*

Society **2010**, *132*, 3252.

[39] Burke, A., Ultracapacitors: why, how, and where is the technology. *Journal of Power Sources* **2000,** 91, (1), 37-50.

[40] Kierzek, K.; Frackowiak, E.; Lota, G.; Gryglewicz, G.; Machnikowski, J., Electrochemical capacitors based on highly porous carbons prepared by KOH activation. *Electrochimica Acta* **2004,** 49, (4), 515-523.

[41] An, K. H.; Kim, W. S.; Park, Y. S.; Choi, Y. C.; Lee, S. M.; Chung, D. C.; Bae, D. J.; Lim, S. C.; Lee, Y. H., Supercapacitors using single-walled carbon nanotube electrodes. *Advanced Materials* **2001,** 13, (7), 4.

[42] Stoller, M. D.; Park, S.; Zhu, Y.; An, J.; Ruoff, R. S., Graphene-Based Ultracapacitors. *Nano Letters* **2008,** 8, (10), 3498-3502.

[43] Li, H.-Q.; Liu, R.-L.; Zhao, D.-Y.; Xia, Y.-Y., Electrochemical properties of an ordered mesoporous carbon prepared by direct tri-constituent co-assembly. *Carbon* **2007,** 45, (13), 2628-2635.

[44] Hwang, S. W.; Hyun, S. H., Capacitance control of carbon aerogel electrodes. *Journal of Non-Crystalline Solids* **2004,** 347, (1-3), 238-245.

[45] Chunsheng Du, N. P., High power density supercapacitor electrodes of carbon nanotube films by electrophoretic deposition. *Nanotechnology* **2006,** 17, 5314-5318.

[46] Naoi, K., 'Nanohybrid Capacitor': The Next Generation Electrochemical Capacitors. *Fuel Cells* **2010**, 10(5), 825-833.

[47] Conway, B. E.; Birss, V.; Wojtowicz, J., The role and utilization of pseudocapacitance for energy storage by supercapacitors. *Journal of Power Sources* **1997,** 66, (1-2), 1-14.

[48] Toupin, M.; Brousse, T.; Belanger, D., Charge Storage Mechanism of MnO_2 Electrode Used in Aqueous Electrochemical Capacitor. *Chemistry of Materials* **2004,** 16, (16), 3184-3190.

[49] Wei, T.-Y.; Chen, C.-H.; Chang, K.-H.; Lu, S.-Y.; Hu, C.-C., Cobalt Oxide Aerogels of Ideal Supercapacitive Properties Prepared with an Epoxide Synthetic Route. *Chemistry of Materials* **2009,** 21, (14), 3228-3233.

[50] Brezesinski, T.; Wang, J.; Polleux, J.; Dunn, B.; Tolbert, S. H., Templated Nanocrystal-Based Porous TiO_2 Films for Next-Generation Electrochemical Capacitors. *Journal of the American Chemical Society* **2009,** 131, (5), 8.

[51] Brezesinski, T.; Wang, J.; Tolbert, S. H.; Dunn, B., Ordered mesoporous α-MoO_3 with iso-oriented nanocrystalline walls for thin-film pseudocapacitors. *Nat Mater* **2009**, (2), 146-151.

[52] Wang, X.; Li, G.; Chen, Z.; Augustyn, V.; Ma, X.; Wang, G.; Dunn, B.; Lu, Y., High-Performance Supercapacitors Based on Nanocomposites of Nb_2O_5 Nanocrystals and Carbon Nanotubes. *Advanced Energy Materials* **2011**, 1(6), 1089-1093.

[53] Toupin, M.; Brousse, T.; Belanger, D., Influence of Microstucture on the Charge Storage Properties of Chemically Synthesized Manganese Dioxide. *Chemistry of Materials* **2002,** 14, (9), 3946-3952.

[54] Pang, S.-C.; Anderson, M. A.; Chapman, T. W., Novel Electrode Materials for Thin-Film Ultracapacitors: Comparison of Electrochemical Properties of Sol-Gel-Derived and Electrodeposited Manganese Dioxide. *Journal of The Electrochemical Society* **2000,** 147, (2), 444-450.

[55] Gogotsi, Y.; Simon, P., True Performance Metrics in Electrochemical Energy Storage. *Science* 334, (6058), 917-918.

[56] Lang, X.; Hirata, A.; Fujita, T.; Chen, M., Nanoporous metal/oxide hybrid electrodes for electrochemical supercapacitors. *Nat Nano* **2011**, 6, 232-236.

[57] Zhang, H.; Yu, X.; Braun, P. V., Three-dimensional bicontinuous ultrafast-charge and -discharge bulk battery electrodes. *Nat Nano* **2011**, 6, 277-281.

[58]. Wang, H.-Q.; Li, Z.-S.; Huang, Y.-G.; Li, Q.-Y.; Wang, X.-Y., A novel hybrid supercapacitor based on spherical activated carbon and spherical MnO_2 in a non-aqueous electrolyte. *Journal of Materials Chemistry* 20, (19).

[59] Kawaoka, H.; Hibino, M.; Zhou, H.; Honma, I., Enhancement of Specific Capacity of Manganese Oxide/Carbon Composite Synthesized by Sonochemical Method. *Electrochemical and Solid-State Letters* **2005,** 8, (5), A253-A255.

[60] Chen, S.; Zhu, J.; Wu, X.; Han, Q.; Wang, X., Graphene Oxide−MnO_2 Nanocomposites for Supercapacitors. *ACS Nano* 4, (5), 2822-2830.

[61] Yan, J.; Fan, Z.; Wei, T.; Qian, W.; Zhang, M.; Wei, F., Fast and reversible surface redox reaction of graphene-MnO_2 composites as supercapacitor electrodes. *Carbon* 48, (13), 3825-3833.

[62] Ma, S.-B.; Nam, K.-W.; Yoon, W.-S.; Yang, X.-Q.; Ahn, K.-Y.; Oh, K.-H.; Kim, K.-B., Electrochemical properties of manganese oxide coated onto carbon nanotubes for energy-storage applications. *Journal of Power Sources* **2008,** 178, (1), 483-489.

[63] Bordjiba, T.; Belanger, D., Direct Redox Deposition of Manganese Oxide on Multiscaled Carbon Nanotube/Microfiber Carbon Electrode for Electrochemical Capacitor. *Journal of The Electrochemical Society* **2009,** 156, (5), A378-A384.

[64] Paek, S.-M.; Yoo, E.; Honma, I., Enhanced Cyclic Performance and Lithium Storage Capacity of SnO_2/Graphene Nanoporous Electrodes with Three-Dimensionally Delaminated Flexible Structure. *Nano Letters* **2008,** 9, (1), 72-75.

[65] Zhang, H.-X.; Feng, C.; Zhai, Y.-C.; Jiang, K.-L.; Li, Q.-Q.; Fan, S.-S., Cross-Stacked Carbon Nanotube Sheets Uniformly Loaded with SnO_2 Nanoparticles: A Novel Binder-Free and High-Capacity Anode Material for Lithium-Ion Batteries. *Advanced Materials* **2009,** 21, (22), 2299-2304.

[66] Ko, J. M.; Kim, K. M., Electrochemical properties of MnO_2/activated carbon nanotube composite as an electrode material for supercapacitor. *Materials Chemistry and Physics* **2009,** 114, (2–3), 837-841.

[67] Wang, Y.; Zhitomirsky, I., Electrophoretic Deposition of Manganese Dioxide-Multiwalled Carbon Nanotube Composites for Electrochemical Supercapacitors. *Langmuir* **2009**, 25 (17), 9684-9689.

[68] Nam, K.-W.; Lee, C.-W.; Yang, X.-Q.; Cho, B. W.; Yoon, W.-S.; Kim, K.-B., Electrodeposited manganese oxides on three-dimensional carbon nanotube substrate: Supercapacitive behaviour in aqueous and organic electrolytes. *Journal of Power Sources* **2009,** 188, (1), 323-331.

[69] Zhang, H.; Cao, G.; Wang, Z.; Yang, Y.; Shi, Z.; Gu, Z., Growth of Manganese Oxide Nanoflowers on Vertically-Aligned Carbon Nanotube Arrays for High-Rate Electrochemical Capacitive Energy Storage. *Nano Letters* **2008,** 8, (9), 2664-2668.

[70] Fischer, A. E.; Pettigrew, K. A.; Rolison, D. R.; Stroud, R. M.; Long, J. W., Incorporation of Homogeneous, Nanoscale MnO_2 within Ultraporous Carbon Structures via Self-Limiting Electroless Deposition: Implications for Electrochemical Capacitors. *Nano Letters* **2007,** 7, (2), 281-286.

[71] Li, L.; Qin, Z.-Y.; Wang, L.-F.; Liu, H.-J.; Zhu, M.-F., Anchoring alpha-manganese oxide nanocrystallites on multi-walled carbon nanotubes as electrode materials for supercapacitor. *Journal of Nanoparticle Research* **2010***,* 12, (7), 2349-2353.

[72] Wang, H.; Cui, L.-F.; Yang, Y.; Sanchez Casalongue, H.; Robinson, J. T.; Liang, Y.; Cui, Y.; Dai, H., Mn_3O_4−Graphene Hybrid as a High-Capacity Anode Material for Lithium Ion Batteries. *Journal of the American Chemical Society* **2010***,* 132, (40), 13978-13980.

[73] Ji, L.; Tan, Z.; Kuykendall, T.; An, E. J.; Fu, Y.; Battaglia, V.; Zhang, Y., Multilayer

nanoassembly of Sn-nanopillar arrays sandwiched between graphene layers for high-capacity lithium storage. *Energy & Environmental Science* **2011**, 4, (9), 3611-3616.

[74] Wang, J.-Z.; Zhong, C.; Wexler, D.; Idris, N. H.; Wang, Z.-X.; Chen, L.-Q.; Liu, H.-K., Graphene-Encapsulated Fe_3O_4 Nanoparticles with 3D Laminated Structure as Superior Anode in Lithium Ion Batteries. *Chemistry – A European Journal* **2011***,* 17, (2), 661-667.

[75] Wang, B.; Wu, X.-L.; Shu, C.-Y.; Guo, Y.-G.; Wang, C.-R., Synthesis of CuO/graphene nanocomposite as a high-performance anode material for lithium-ion batteries. *Journal of Materials Chemistry* **2010**, 20, 10661-10664.

[76] Cabana, J.; Monconduit, L.; Larcher, D.; Palacín, M. R., Beyond Intercalation-Based Li-Ion Batteries: The State of the Art and Challenges of Electrode Materials Reacting Through Conversion Reactions. *Advanced Materials* **2010**, 22, (35), E170-E192.

[77] Zhou, W.; Liu, J.; Chen, T.; Tan, K. S.; Jia, X.; Luo, Z.; Cong, C.; Yang, H.; Li, C. M.; Yu, T., Fabrication of Co_3O_4-reduced graphene oxide scrolls for high-performance supercapacitor electrodes. *Physical Chemistry Chemical Physics* **2011**, 13 (32), 14462-14465.

[78] Wang, H.; Liang, Y.; Mirfakhrai, T.; Chen, Z.; Casalongue, H.; Dai, H., Advanced asymmetrical supercapacitors based on graphene hybrid materials. *Nano Research* **2011**, 4, (8), 729-736.

[79] Kim, I.-H.; Kim, J.-H.; Lee, Y.-H.; Kim, K.-B., Synthesis and Characterization of Electrochemically Prepared Ruthenium Oxide on Carbon Nanotube Film Substrate for Supercapacitor Applications. *Journal of The Electrochemical Society* **2005,** 152, (11), A2170-A2178.

2. High-Performance Supercapacitors Based on Nanocomposites of Nb_2O_5 Nanocrystals and Carbon Nanotubes

2.1. Introduction

Electrical-energy storage devices, including batteries and supercapacitors, are commonly used for consumer electronics, portable electric devices, electric vehicles and other applications.[1,2] Compared with batteries, supercapacitors often deliver significantly higher power densities with longer cycling life but lower energy densities. Developing supercapacitors with improved energy density therefore becomes a highly attractive topic.

Generally, energy densities of supercapacitors (E) are determined by $E = \frac{1}{2} CV^2$, where C is the cell capacitance and V is the cell potential; higher cell voltage and capacitance lead to higher energy density.[3] Porous carbon, the most commonly used electrode material, possesses a double layer capacitance of 100~150 F g^{-1} in organic-electrolyte, while transition metal oxides may exhibit significantly higher pseudo-capacitances. Designing asymmetric supercapacitors consisting of a carbon cathode and a transition-metal anode is therefore considered as the most effective solution.[4] For instance, asymmetric cells based on $Li_4Ti_5O_{12}$ anode and activated carbon cathode can achieve an energy density of 40 Wh kg^{-1} in organic-electrolyte system,[5,6] which is much higher than those of carbon-based symmetric devices. Seeking better anode materials with high specific capacitance, low working potential, and long cycling stability therefore become a main theme of the field.

Compared with $Li_4Ti_5O_{12}$ with a working potential of 1.5 V and a specific capacity of 140 mA h g^{-1},[7] niobium pentoxide (Nb_2O_5) exhibits a higher capacity (~200 mA h g^{-1}) and a relatively low average working voltage (1.0~1.5 V versus Li^+/Li).[8-10] In this context, niobium pentoxide is considered as a highly promising material candidate. Nevertheless, due to its poor electric conductivity ($\sigma\sim3\times10^{-6}$ S cm^{-1}),[11] most efforts have been focused on their use for low-voltage lithium batteries rather than supercapacitors. To date, several methods have been explored to overcome this barrier. One strategy is to use more conductive agent such as carbon black, which can improve electrode rate capability but may reduces the overall capacity.[10] Increasing intrinsic conductivity of Nb_2O_5 through annealing and reducing process at high temperature (e.g., 1000 ºC) is another approach.[11] Recently, Dunn *et al*. reported the formation of mesoporous Nb_2O_5 thin-film electrode (~200 nm) with excellent rate capability.[12]

Herein, we report the fabrication of thick Nb_2O_5 electrodes from the nanocomposites of Nb_2O_5 nanocrystals and carbon nanotubes (CNTs). **Figure 1** illustrates the structure of the composite electrode, which consists of interpenetrative CNTs networks and intimately mixed Nb_2O_5 nanocrystals. CNTs are commonly used for supercapacitors due to their high conductivity, strong mechanical properties, and chemical stability.[13-16] The intimate contacts between the nanocrystals and the CNTs networks enable fast electron transport and effective current collection. The small dimension of the nanocrystals shortens lithium-ion diffusion length. Moreover, the nanocomposites contain interconnected porous channels for effective ion transport. These unique features endow the electrodes with high energy and power densities.

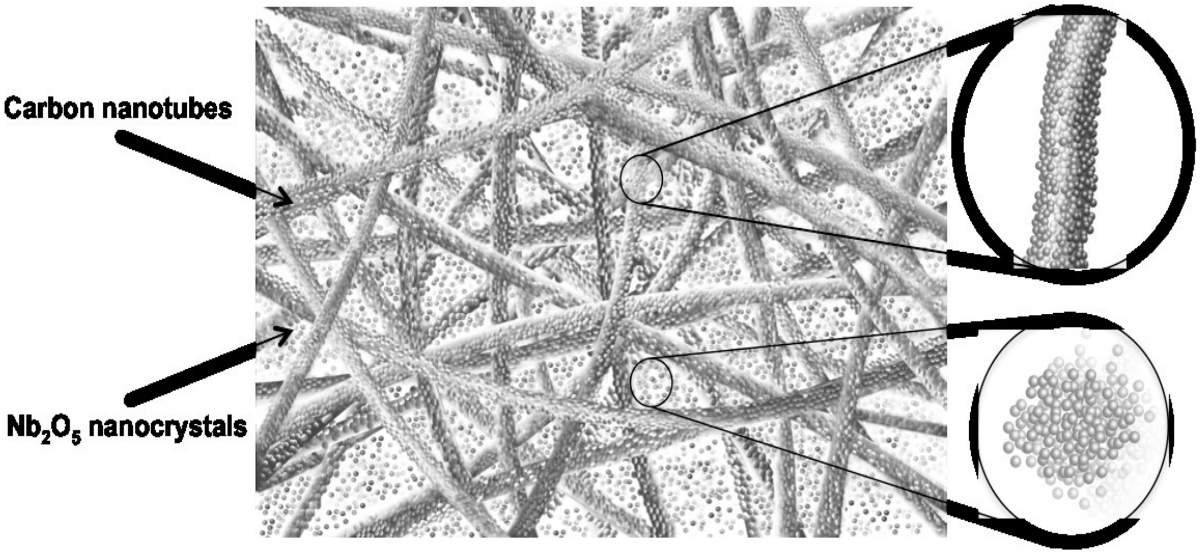

Figure 2.1 Scheme of a composite electrode of Nb2O5 nanocrystals and CNTs

2.2. Results and Discussion

Figure 2A presents a representative transmission electron microscopy (TEM) image of the as-synthesized Nb_2O_5 nanocrystals. Such nanocrystals are uniformed in size with an average diameter of 5 nm. **Figure 2B** shows a high-resolution TEM image of the nanocrystals, revealing an ordered crystalline structure. The observed lattice spacing of 0.39 nm is consistent with the (002) plane of pseudo-hexagonal structure, which is confirmed by X-ray diffraction (XRD) study shown in **Figure 3**. These nanocrystals can be well dispersed within CNTs and other additives ensuring the formation of homogeneous composite electrodes. **Figure 2C** shows a representative scanning electron microscopic (SEM) image of the composite electrode made from CNC-20. A continuous homogenous structure with CNTs entangled through the whole composite (inset, **Figure 2C**) is clearly observed. **Figure 2D** shows a cross-section SEM image exhibiting a continuous electrode structure with a thickness around 3 micrometers.

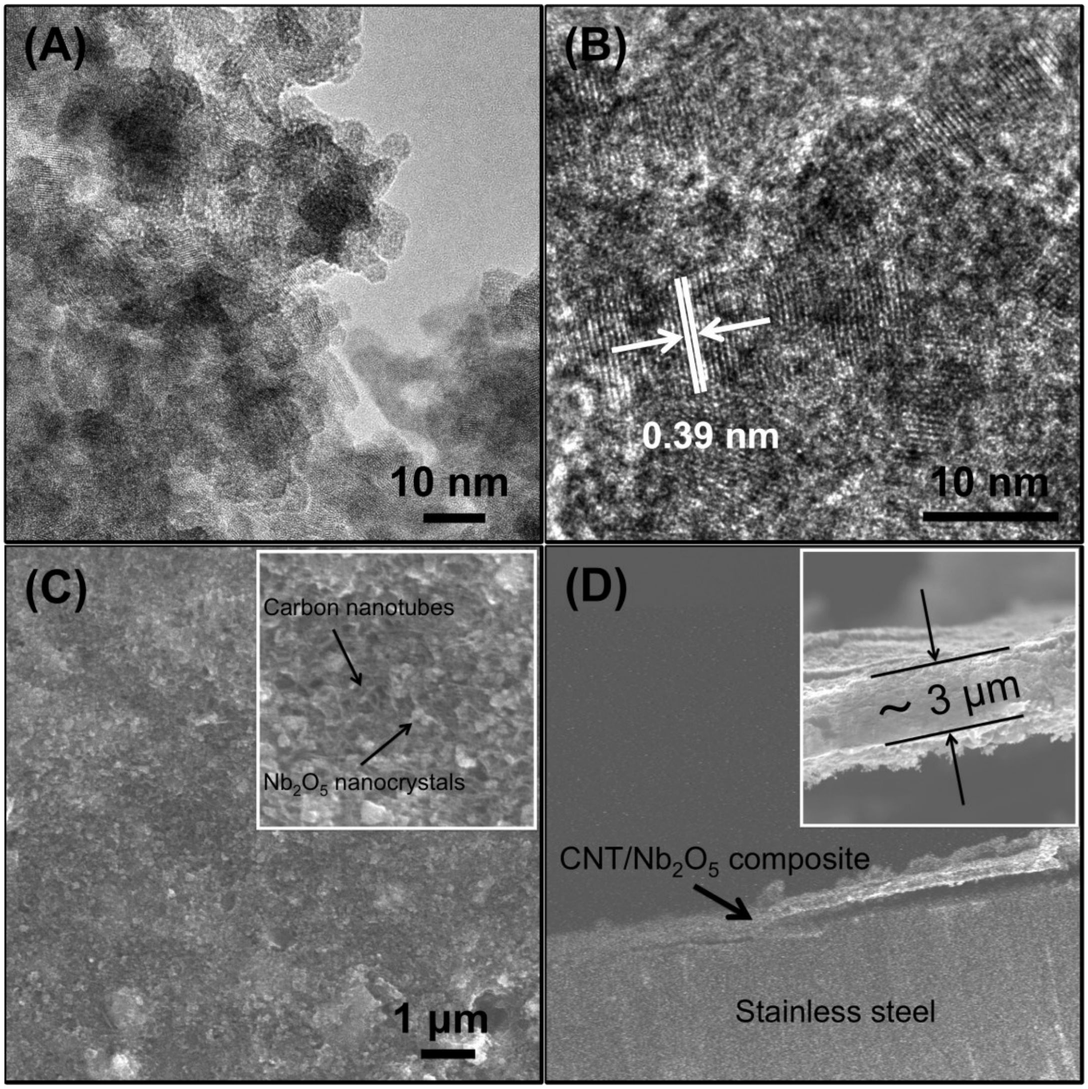

Figure 2.2 (A) Low- and (B) high-resolution TEM images of the as-synthesized Nb_2O_5 nanocrystals and SEM images of (C) the surface and (D) cross-section of a composite electrode made from CNC-20. Insets: high-magnitude SEM images of the (C) surface and (D) cross-section of CNC-20 electrode.

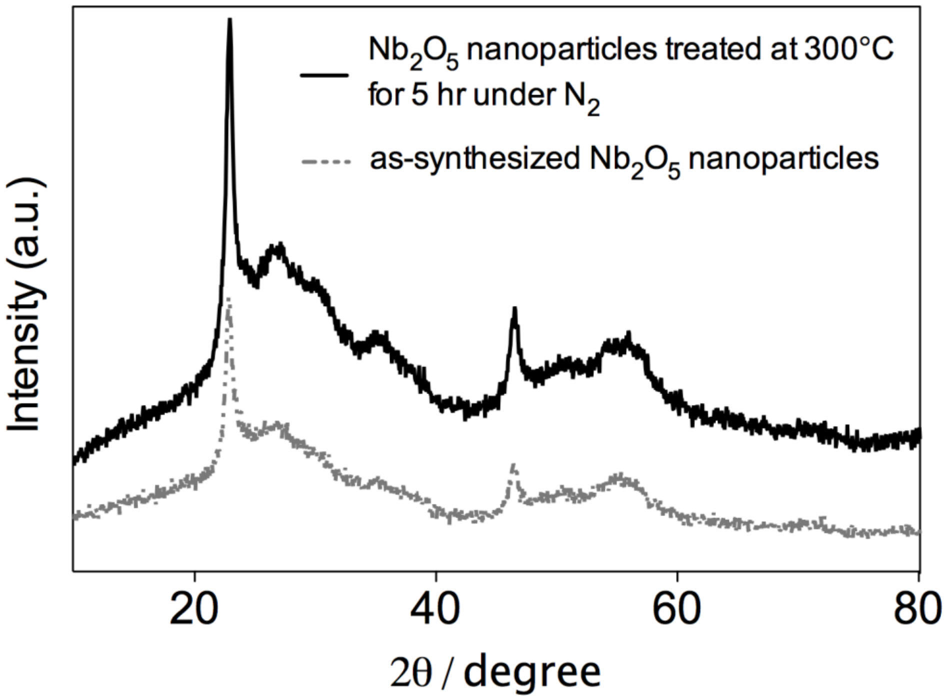

Figure 2.3 XRD patterns of the (a) as-synthesized Nb_2O_5 nanopaticles, and (b) nanocrystals treated at 300ºC for 5 h in N_2

Electrochemical behavior of the composite electrodes was investigated using three-electrode cells, in which lithium foils were used as both the counter and reference electrodes. The charge storage behavior was characterized by cyclic voltammetry (CV). Generally, electrochemical Li^+ insertion process occurring at Nb_2O_5 electrodes can be described by $Nb_2O_5 + xLi^+ + xe^- \leftrightarrow Li_xNb_2O_5$, where x is the mole fraction of the inserted lithium ions.[18-19] **Figure 4A** compares the cyclic voltammograms of the electrodes of Nb_2O_5 nanocrystals, CNTs, and CNT/Nb_2O_5 composite using a sweeping rate of 2 mV s^{-1}. The CNT electrode shows a typical double-layer capacitive performance; while the nanocrystals electrode shows symmetric cathodic and anodic peaks at around 1.5 V, indicating a reversible lithium intercalation and de-intercalation process. In contrast, the nanocomposite electrode (CNC-20) exhibits broader peaks, consisting with intercalation-type electrochemical reactions with broader distribution of energy.[11] The larger area of within the CV curve indicates a higher capacitance, which may be resulted from the conductive CNT networks that facilitate more effective electron transport and the current collection.

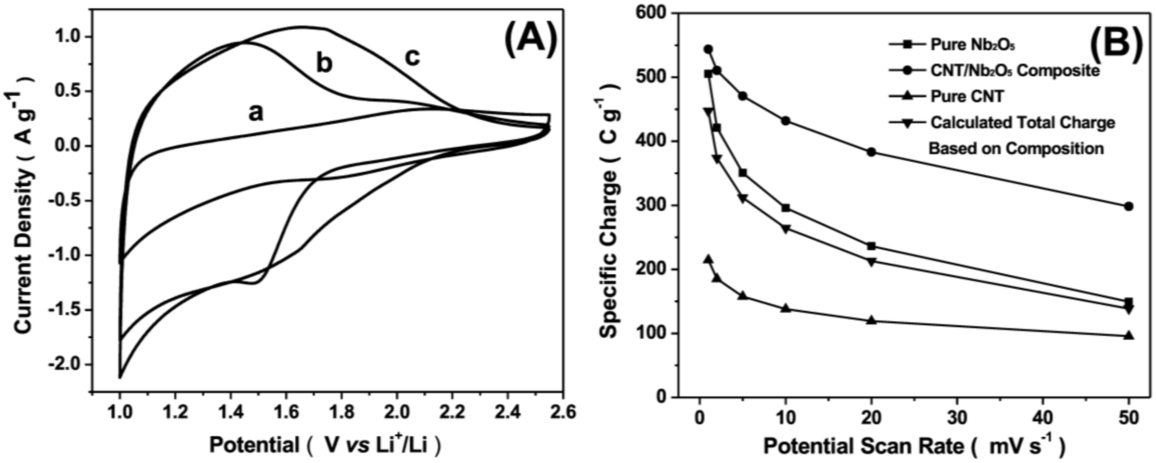

Figure 2.4 (A) Cyclic voltammograms of the electrodes of (a) CNTs, (b) Nb_2O_5 nanocrystals and (c) CNC-20 at a scanning rate of 2 mV s^{-1} in 1 M $LiClO_4$ in PC at room temperature; (B) Comparison of the rate capability of CNTs, Nb_2O_5 nanocrystals, and CNC-20 based electrodes, and the total charge storage by simply adding the capacity contribution of each constituent of the composite electrode. The specific charge of Nb_2O_5 nanocrystals and CNC-20 electrodes are calculated between 1.20 and 2.55 V

Figure 4B compares the charge storage of the electrodes of Nb_2O_5 nanocrystals, CNTs and the composite CNC-20 at sweeping rates of 1 to 50 mV s^{-1} (equal to charge/discharge times from 1350 to 27 s, respectively) (see **Figure 5** for details). As expected, the CNT electrode shows a high rate capability but low capacitance contributed from the electrical double-layer capacitance (**Figure 6**). At 1 mV s^{-1}, the electrodes of CNTs and Nb_2O_5 nanocrystals show a capacity of 215 and 397 C g^{-1}, respectively. Simply adding the capacity contribution of each constituent component (CNTs and the nanocrystals) at this sweep rate would give a capacity of 361 C g^{-1}, which is significantly lower than the measured capacity for the composite electrode (445 C g^{-1}). Interestingly, the measured capacity of the composite electrode is even higher than that of the pure nanocrystal electrode, suggesting that the addition of the CNTs leads to improved charge transfer for the nanocrystals. This effect becomes more pronounced at higher scan rates. For example, at 50 mV s^{-1}, the pure Nb_2O_5 electrode exhibits only 31% (125 C g^{-1}) of the capacity measured at 1 mV s^{-1}. In contrast, the CNTs/Nb_2O_5 composite electrode exhibits substantially higher capacity (267 C g^{-1}) at 50 mV s^{-1}, which is 60% of its value at 1 mV s^{-1}. Such observation is similar to that of nanocomposite electrodes consisting of interpenetrative network of CNTs and V_2O_5 nanowires,[16] indicating a general route to constructing high-performance electrode with improved rate and capacity performance through constructing the CNTs-based electrode nanocomposites.

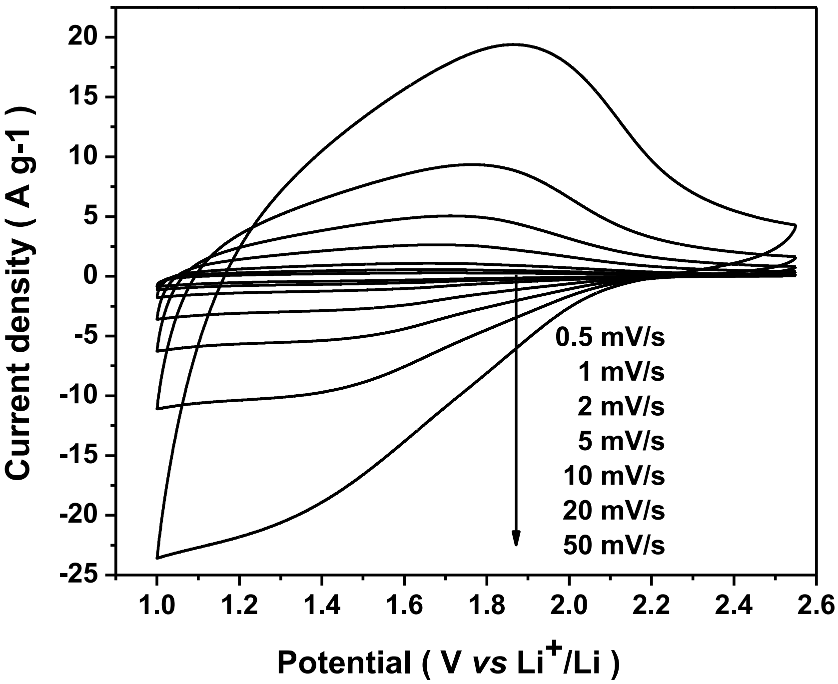

Figure 2.5 CV curves of the CNT/Nb_2O_5 composite electrode (CNC-20) at various potential scanning rates from 1.0 to 50 mV s^{-1} in 1 M $LiClO_4$ in PC solution at room temperature

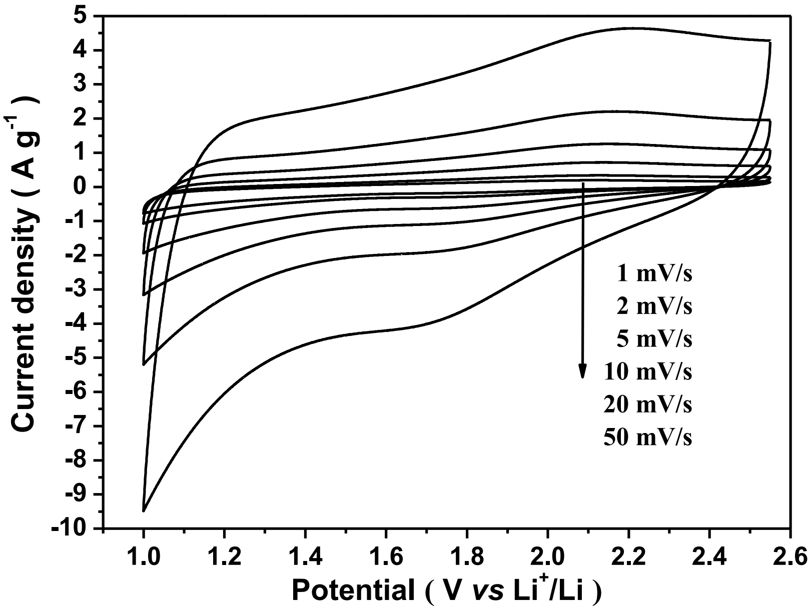

Figure 2.6 Cyclic voltammograms of the CNTs electrode

To further understand how the integration of CNTs into the nanocomposites leads to improved rate capability, we further analyzed the contribution of the total charge stored based on Trasatti's method.[20] Generally, the scan rate (v) dependence of total stored charge q involves in the slow access of Li$^+$ into the "inner" region of surface, in another word, q is a function of diffusion time. According to diffusion law, q is linearly related to the reciprocal of the square root of the scan rate, which can be described by the following equation:

$$q(v) = q_0 + k^*(v^{-1/2}) \qquad (1)$$

where q_0 is the stored charge that related to the accessible outer surface, k is a constant and $k^*(v^{-1/2})$ represents the diffusion-controlled charge. Simply plotting the $v^{-1/2}$ dependence of the total stored charge from 1 to 20 mV s^{-1}, and extrapolating the straight line to the y-axis intercept point allows us to determine the outer surface charge. **Figure 7A** compares the total charges stored for the electrodes of CNC-20 and Nb_2O_5 nanocrystals at 1 mV s^{-1} and 20 mV s^{-1}, respectively. The composite electrode shows more total charge and outer surface charge than that of the Nb_2O_5 nanocrystals electrode. This comparison quantitatively proves that constructing networks of CNTs and Nb_2O_5 nanocrystals makes the Nb_2O_5 surface sites more accessible, which is consistent with the observed enhanced electronic conductivity and rates performance.

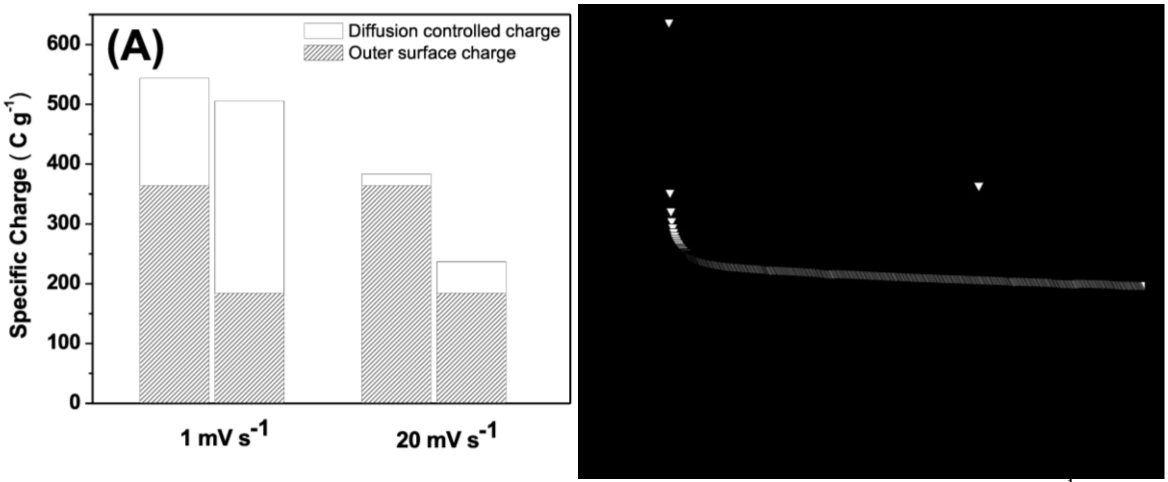

Figure 2.7 (A) Comparison of the total charge stored at scan rates of 1 and 20 mVs^{-1}. For the both scan rates, the left columns refer to composite electrodes (CNC-20) while the right columns refers to the Nb_2O_5 nanocrystal electrodes; (B) cyclic performance of the CNT/Nb_2O_5 composite electrode operated at potential range 1.2 to 2.5 V.

In addition to the enhanced capacity and rate capability, the composite electrodes also exhibited excellent cycling properties. **Figure 7B** shows the cycling stability of the composite electrode. It retained specific capacitances higher than 288 C g^{-1} (80 mA h g^{-1}) after 500 cycles at a 20 C charge/discharge rate. It has been commonly observed that nano-dimensional materials, such as MnO_2 nanocrystals, may lose most of their initial capacitance during cycling, mainly due to agglomeration and reduced surface area exposed to the electrolyte.[21] The long cycling stability observed could be attributed to its unique composite structure that effectively preserves the structure integrity. Similar effect was also observed for the nanocomposites of CNTs and V_2O_5 nanowires,[16] MnO_2 and polymer coaxial nanowires,[29, 30] further confirming that constructing the CNTs based nanocomposites not only leads to improved rate and capacity performance but also cycling stability.

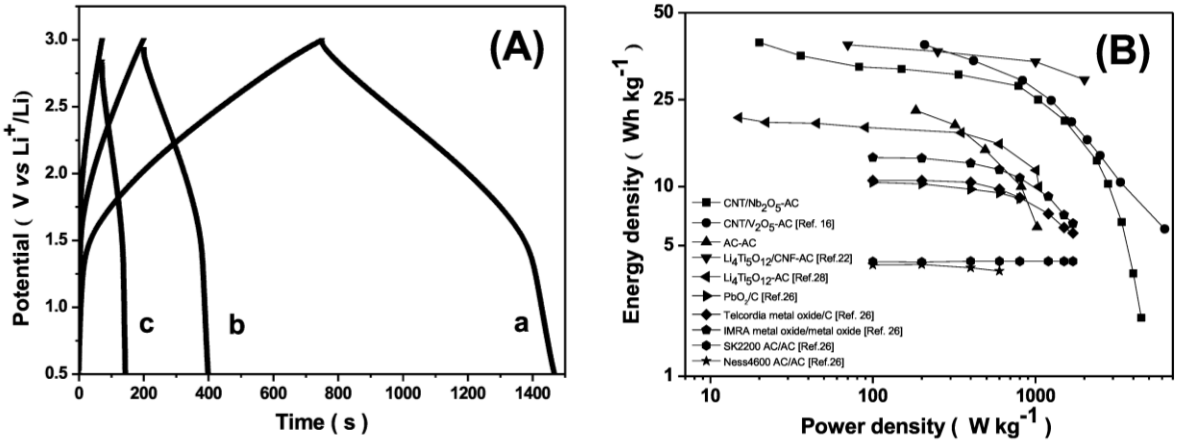

Figure 2.8 (A) Galvanostatic charge-discharge curves of an asymmetric supercapacitor at current density of (a) 0.74 A g^{-1}, (b) 2.35 A g^{-1} and (c) 5.66 A g^{-1} in 1 M LiClO$_4$ at room temperature; (B) Ragone plots of an asymmetric supercapacitor made from active carbon (AC) cathode and a CNT/Nb$_2$O$_5$ composite anode, a symmetric supercapacitor made from the same AC electrodes, and various supercapacitor types developed recently.[22,23] All data are based on the mass of the electrode materials. For the devices reported in Ref. [26], the mass of the electrode materials was estimated to be 40% of the total device weight. A packaging factor on the order of 0.4 was used by several authors.[24-26]

To assess the feasibility of using such composites for actual device fabrication, asymmetric supercapacitors were assembled using the composite as an anode and a commercial active carbon (AC) as the cathode. According to the capacity and operation window of each electrode, a cathode to anode mass ratio was chosen to be 3:1.[16] **Figure 8A** shows the typical galvanostatic charge/discharge curves of the asymmetric device at different current densities. An energy density of 33.5 Wh kg^{-1} (based on the total weight of the anode and cathode materials) was achieved at the current density of 0.74 A g^{-1} (corresponding to a power density of 82 W kg^{-1}). Even at a power density of 4000 W kg^{-1} (charge and discharge time of 3.6 s), the device still possesses an energy density of 3.6 Wh kg^{-1}, an indication of high-power performance. **Figure 8B** further compares the Ragone plots derived from constant current charge/discharge characteristics for different prototype supercapacitors, as well as the symmetric supercapacitors made from AC for comparison. Also shown here are the recent results of hybrid supercapacitors based on CNF-grafted nanocrystalline $Li_4Ti_5O_{12}$. This asymmetric supercapacitor shows a competitive energy and power performance with that of graphitic carbon[27], $Li_4Ti_5O_{12}$,[28] or other metal oxide based hybrid systems,[16,23] which represents a significant improvement over the current state-of-the-art electric double-layer capacitor (EDLC) technology.

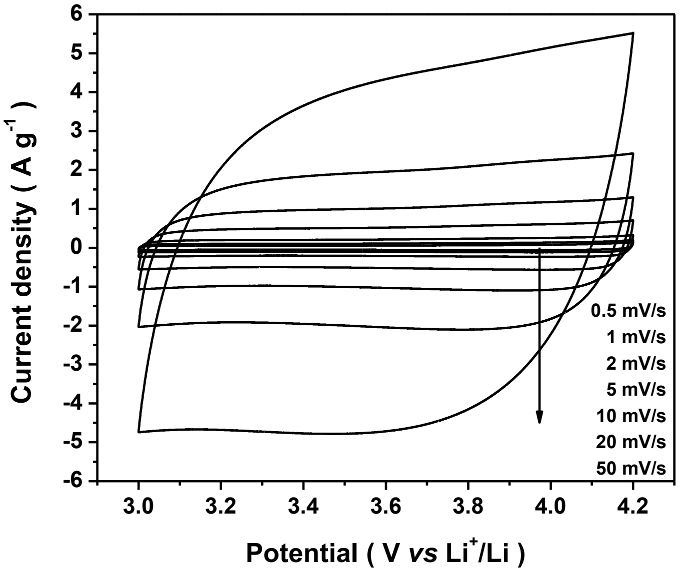

Figure 2.9 Cyclic voltammograms of the electrodes made from commercial activated carbon with a loading mass of 0.4 mg (5 μL)

2.3. Conclusion

In summary, we have developed nanocomposites of Nb_2O_5 nanocrystals and CNTs for supercapacitor application. This composite possesses high capacitance and excellent rate capability and cycling stability. Prototype asymmetric supercapacitors were fabricated with highly promising performance. This work provides an effective structure design by integrating metal-oxide nanocrystals and conductive CNTs networks into robust nanocomposite structure, which may be generalized to synthesize other nanocomposites for better-performance energy storage.

2.4. Experimental Section

Synthesis of Nb_2O_5 nanocrystals and CNTs/Nb_2O_5 nanocomposites: A one-pot hydrothermal method was used to synthesize Nb_2O_5 nanocrystals. In a typical reaction, ammonium niobate oxalate hydrate (0.2 g) and surfactant P123 ($EO_{20}PO_{70}EO_{20}$, where EO and PO are ethylene oxide and propylene oxide, respectively, 0.8 g) were dissolved in deionized water (60 mL) under ultrasonication for 30 min. HCl (2 M, 0.5 mL) was added into the solution before it was transferred to an 80 mL Teflon-lined autoclave and heated at 200 ºC for 24 h. The resulted precipitates were rinsed with water and ethanol and dried at 80 ºC for 12 h under vacuum. Multi-wall carbon nanotubes (CNTs) were functionalized by generating carboxylic groups on their surface using a method similar to that by Gao *et al.*.[17] Details of the materials synthesis were described in our previous publication.[15] X-ray diffraction (XRD) experiments were conducted on a X'Pert Pro X-ray diffractometer (Panalytical B.V.); scanning electron microscopic (SEM) experiments were conducted on a JEOL JSM-6700 FE-SEM (JEOL); transmission electron microscopic (TEM) experiments were conducted on a Philips CM120 operated at 120 kV (Philips/FEI), and high resolution TEM experiments were conducted on a Titan STEM (Philips/FEI).

Electrode Fabrication and Electrochemical Measurements: Appropriate ratios of Nb_2O_5 nanocrystals and CNTs were dispersed in *N*-methylpyrrolidinone (NMP) and ultrasonicated to form homogeneous and stable dispersions, where PVDF and carbon black were also added. The composites with 10, 20 and 30 wt-% of the CNTs were denoted as CNC-10, CNC-20 and CNC-30, respectively. The CNT/Nb_2O_5 composites electrodes were prepared by coating the slurries containing 10 wt-% carbon black, 10 wt-% polyvinylidenedifluoride (PVDF) and 80 wt-% of the composites onto stainless steel current collectors. The electrodes were dried at a room temperature for 8 h and then annealed at 300 ºC for 5 h under N_2. The thickness of the electrodes can be controlled from ~1 to 20 microns. The activated carbon (AC) cathode was assembled with the same ratio of carbon black and PVDF. The activated carbon with a surface area of ~ 1,900 m^2 g^{-1} has a gravimetric capacitances of 110 F g^{-1} or 72 F g^{-1} at the scan rates of 1 and 50 mV s^{-1} respectively (**Figure 9**, Supporting Information).

Electrochemical measurements were carried out on a VMP3 potentiostat/galvanostat (Bio-Logic LLC, Knoxville, TN). The electrolyte solution was a 1 M $LiClO_4$ in propylene carbonate (PC) and lithium foils were used as both the counter and reference electrodes. Cyclic voltammetric (CV) measurements were carried out in an argon-filled glove box using cutoff voltages of 2.55 and 1.0 V versus Li^+/Li. The asymmetric device was assembled with an anode of composite electrode and a cathode of AC electrode, and built in an open cell. The capacities of the composite electrodes with different loadings at different scanning rates were shown in Figure S5 (Supporting Information). Asymmetric cells were charged and discharged between 3.0 and 0.5 V, and AC-based symmetric cells were charged and discharged between 2.7 and 0 V. The specific capacitance, power and energy density were calculated based on the total mass of anode and cathode materials. Energy density was calculated using $E = \frac{1}{2} CV^2$, where C is the total cell capacitance and V is the maximum cell potential.

Reference:

[1] B. E. Conway, *Electrochemical Supercapacitors; Scientific Fundamentals and Technological Applications*, Kluwer Academic/Plenum Pblishers, New York, **1999**.

[2] A. S. Arico, P. Bruce, B. Scrosati, J.-M. Tarascon, W. van Schalkwijk, *Nat. Mater.* **2005**, *4*, 366.

[3] L. L. Zhang, X. S. Zhao, *Chem. Soc. Rev.* **2009**, *38*, 2520.

[4] P.-C. Chen, G. Shen, Y. Shi, H. Chen, C. Zhou, *ACS Nano* **2010**, *4*, 4403.

[5] J. P. Zheng, *J. Electrochem. Soc.* **2003**, *150*, A484.

[6] C. M. Ionica-Bousquet, D. MuÒoz-Rojas, W. J. Casteel Jr, R. M. Pearlstein, G. G. Kumar, G. P. Pez, M. R. PalacÌn, *J. Power Sources* **2011**, *196*, 1626.

[7] S.-H. Kang, D. P. Abraham, W.-S. Yoon, K.-W. Nam, X.-Q. Yang, *Electrochim. Acta* **2008**, *54*, 684.

[8] J.-T. Han, D.-Q. Liu, S.-H. Song, Y. Kim, J. B. Goodenough, *Chem. Mater.* **2009**, *21*, 4753.

[9] J.-T. Han, Y.-H. Huang, J. B. Goodenough, *Chem. Mater.* **2011**, *23*, 2027.

[10] M. Wei, K. Wei, M. Ichihara, H. Zhou, *Electrochem. Commun.* **2008**, *10*, 980.

[11] A. L. Viet, M. V. Reddy, R. Jose, B. V. R. Chowdari, S. Ramakrishna, *J. Phys. Chem. C* **2009**, *114*, 664.

[12] K. Brezesinski, J. Wang, J. Haetge, C. Reitz, S. O. Steinmueller, S. H. Tolbert, B. M. Smarsly, B. Dunn, T. Brezesinski, *J. Am. Chem. Soc.* **2010**, *132*, 6982.

[13] J. P. Zheng, P. J. Cygan, T. R. Jow, *J. Electrochem. Soc.* **1995**, *142*, 2699.

[14] Y. U. Jeong, A. Manthiram, *J. Electrochem. Soc.* **2002**, *149*, A1419.

[15] Z. Chen, Y. Qin, D. Weng, Q. Xiao, Y. Peng, X. Wang, H. Li, F. Wei, Y. Lu, *Adv. Func. Mater.* **2009**, *19*, 3420.

[16] Z. Chen, V. Augustyn, J. Wen, Y. Zhang, M. Shen, B. Dunn, Y. Lu, *Adv. Mater.* **2011**, *23*, 791.

[17] C. Gao, C. D. Vo, Y. Z. Jin, W. Li, S. P. Armes, *Macromolecules* **2005**, *38*, 8634.

[18] N. Ozer, D.-G. Chen, C. M. Lampert, *Thin Solid Films* **1996**, *277*, 162.

[19] R. Kodama, Y. Terada, I. Nakai, S. Komaba, N. Kumagai, *J. Electrochem. Soc.* **2006**, *153*, A583.

[20] S. Ardizzone, G. Fregonara, S. Trasatti, *Electrochim. Acta* **1990**, *35*, 263.

[21] M. Toupin, T. Brousse, D. Belanger, *Chem. Mater.* **2002**, *14*, 3946.

[22] K. Naoi, *Fuel Cells* **2010**, *10*, 825.

[23] A. Burke, presented at Vehicle Power and Propulsion, 2005 IEEE Conference, The present and projected performance and cost of double-layer pseudo-capacitive ultracapacitors for hybrid vehicle applications, Chicago, Sept. **2005**.

[24] S. W. Lee, N. Yabuuchi, B. M. Gallant, S. Chen, B.-S. Kim, P. T. Hammond, Y. Shao-Horn, *Nat. Nano.* **2010**, *5*, 531.

[25] S. Eaves, J. Eaves, *J. Power Sources* **2004**, *130*, 208.

[26] G. B. Appetecchi, P. P. Prosini, *J. Power Sources* **2005**, *146*, 793.

[27] Advanced Capacitor Technologies, Inc., http://www.act.jp/eng/premlis/premlis.htm (accessed May, 2011).

[28] Telcordia Energy Storage Research Group, http://www.argreenhouse.com/ESR/ah (accessed May, 2011).

[29] R. Liu, S. B. Lee, *J. Am. Chem. Soc.* **2008**, *130*, 2942.

[30] R. Liu, J. Duay, S. B. Lee, *Chem. Comm.* **2011**, *47*, 1384.

3. *In-Situ* Growth of Nb_2O_5 Nanocrystals on CNTs: A Novel Composite for Ultrafast Reversible Lithium Storage

3.1. Introduction

Supercapacitors are emerging as a class of high-power energy-storage devices[1–4]; their broader uses, however, are still limited by their energy density[5–7]. Generally, a supercapacitor is based on the electrical double layers formed along carbon electrodes, which may provide capacitance of up to 300 F/g in an aqueous electrolyte[8, 9]. Oxides of transition metals, such as RuO_2 [10–12], MnO_2 [13–16], NiO [17, 18], Co_3O_4 [19] and V_2O_5 [20, 21], possess significantly higher capacitances; however, harvesting such capacitance has been limited by their low conductivity and redox kinetics. To address such intrinsic limitations, a common strategy is to integrate low-dimensional oxide materials with conductive components, such as carbon, which has led to the development of various nanocomposites with significantly improved energy density [22–24]. Nevertheless, many essential questions about such composites, such as how the structure, composition and interfaces of the composites may affect the capacitive performance, remain open.

We recently developed a new class of pseudocapacitive nanocomposite materials for asymmetric supercapacitors by physically mixing Nb_2O_5 nanocrystals and CNTs. In this paper, we report a facile solvo-thermal synthesis of CNT/Nb_2O_5 nanocomposites with outstanding rate capability, as well as long term cycling stability. As shown in **Figure 1**, Nb_2O_5 nanocrystals *in-situ* grow on CNTs scaffold, forming intimate contact between the two components. Such a unique architecture provides several major advantages: (i) the small dimension of the nanocrystals efficiently shortens lithium-ion diffusion length, leading to better utilization of

Nb_2O_5; (ii) the CNTs network creates interconnected porous channels, enabling both effective electrolyte transport and fast active material accessibility; (iii) the *in-situ* growth ensures the intimate contacts and robust structure, endowing the electrode with high power density and cycling stability.

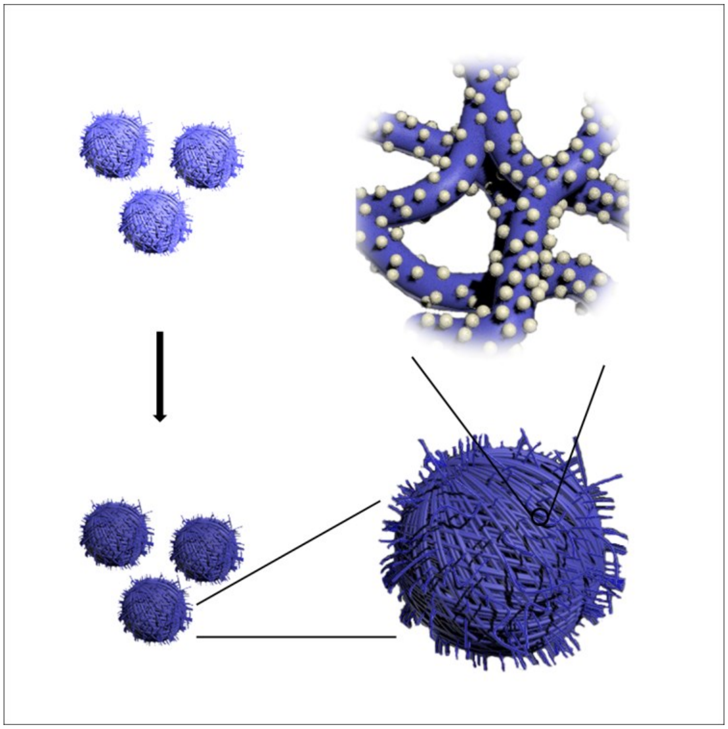

Figure 3.1 Schematic of *in-situ* growing Nb_2O_5 nanocrystals on CNTs scaffold after post sintering process.

3.2. Results and Discussions

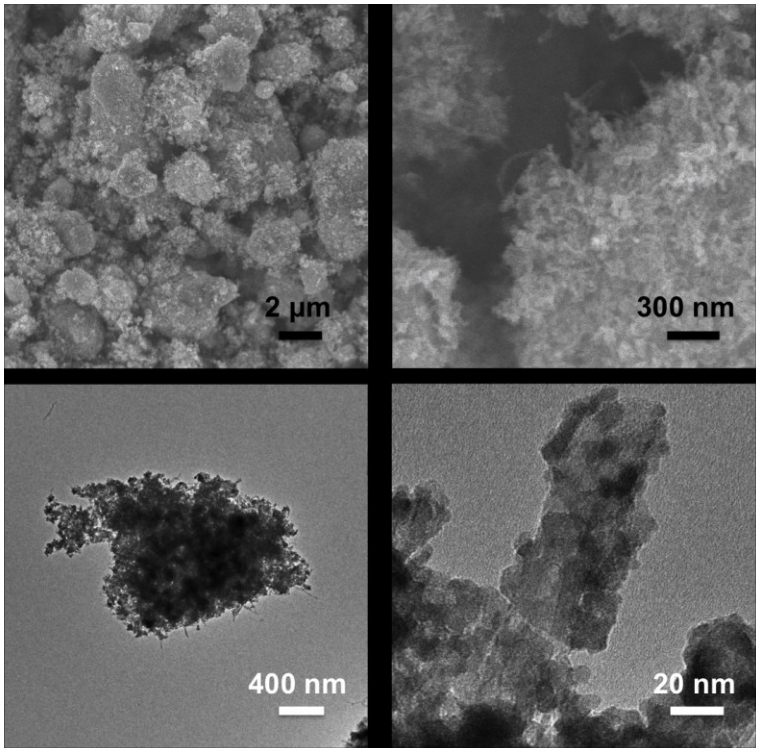

Figure 3.2 Representative low- (A) and high- (B) magnification SEM images of CNT/Nb_2O_5 composites; (C) Representative TEM image of a single CNT/Nb_2O_5 composites sphere; (D) High-magnification TEM image of a piece of CNT covered with *in-situ* grown Nb_2O_5 nanocrystals

Figure 2A shows a representative scanning electron microscopic (SEM) image of the as-synthesized CNT/Nb_2O_5 composites. The composites possess spherical morphology with sizes ranging from hundreds of nanometers to several microns. A high-magnification SEM image (**Figure 2B**) clearly shows the composite structure where CNTs build a network through the whole composite sphere. **Figure 2C** presents a representative transmission electron microscopic (TEM) image of a single composite sphere with the size of around 2 microns. The Nb_2O_5 NCs and CNTs are firmly combined with no obvious separated and isolated NCs or CNTs can be observed, indicating a strong bonding between the two components. The successful *in-situ* growth of Nb_2O_5 nanocrystals on CNTs is further confirmed by TEM observation in **Figure 2D**. Nb_2O_5 nanocrystals with average size of 6 nm grow on CNTs directly and uniformly. Such a structure ensures short diffusion length, continuous conductive pathway, and intimate interface contacts between the NCs and the CNTs, which endows the electrodes with excellent lithium-storage ability.

Figure 3A shows X-ray diffraction (XRD) patterns of CNT/Nb_2O_5 composite before and after annealing at 600ºC. The composites without annealing process show amorphous feature. By comparison, the annealed Nb_2O_5 NCs in CNT/Nb_2O_5 composites possess an orthorhombic crystal structure (JCPDS card No. 28-0317), which is the same as the pure Nb_2O_5 crystals synthesized in identical conditions without using CNTs (**Figure 3B**). The average size of Nb_2O_5 crystals in composites is calculated to be around 6 nm from Scherrer's equation, which is consistent with TEM observation. **Figure 3C** shows the nitrogen adsorption-desorption isotherms of pure Nb_2O_5 crystals and CNT/Nb_2O_5 composite after annealing. The composite exhibits a Brunauer–Emmett–Teller (BET) surface area of 120 m^2 g^{-1} and a pore diameter distribution centered at ~8 nm. In contrast, without the CNT scaffold, pure Nb_2O_5 gave a BET surface area of only ~45 m^2 g^{-1}). This result indicates that the presence of CNTs effectively prevents the growth of NC size, which is essential to retain their shortened ion-transport distance. Moreover, as-formed hierarchical structure with high surface area provides the electrodes with efficient ion transport and abundant active sites. **Figure 3D** shows thermogravimetric analysis (TGA) curves of the CNTs and CNT/Nb_2O_5 composite in air. No appreciable weight loss can be observed for the CNTs at temperature below around 400ºC, while the sintered composites consist of 77 wt.% of Nb_2O_5 and 24 wt.% of CNTs. The mass ratio of Nb_2O_5 and CNTs can be easily adjusted to synthesize a class of composites with tunable properties. In this paper, we mainly focused on the composite with 77 wt.% of Nb_2O_5 and 24 wt.% of CNTs to demonstrate the outstanding performance of *in-situ* growth of Nb_2O_5 on CNTs composites.

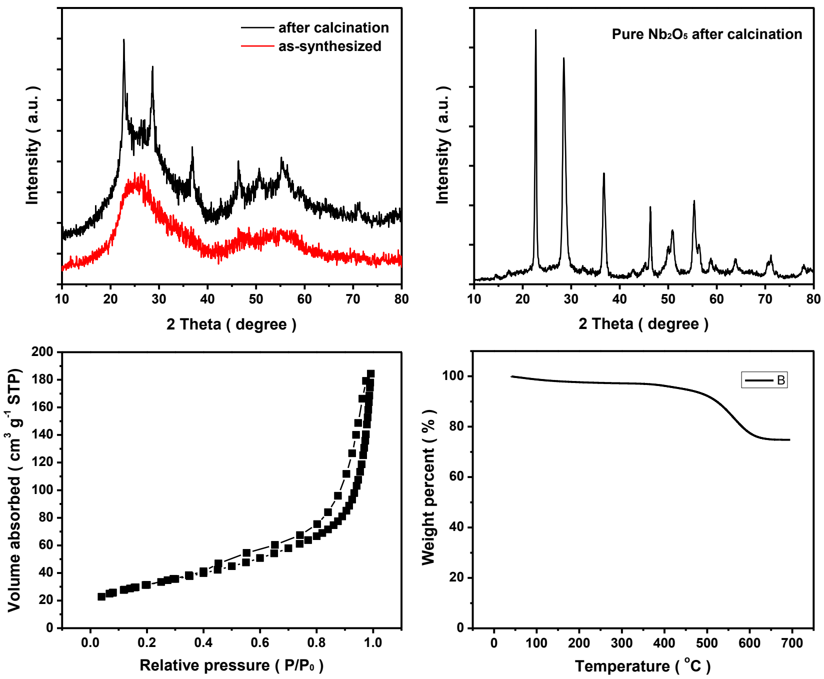

Figure 3.3 (A) XRD patterns of CNTs-Nb_2O_5 composites before and after calcination at 600°C; (B) XRD pattern of pure Nb_2O_5 material synthesized in identical condition; (C) Nitrogen absorption-desorption isotherms of CNTs-Nb_2O_5 composites after calcination; and (D) thermogravimetric analysis curve of the CNTs-Nb_2O_5 composites in air.

The charge storage behavior of the CNT/Nb_2O_5 composites was characterized by cyclic voltammetry (CV) using coin-type half-cells. Generally, electrochemical Li^+ intercalation/de-intercalation processes occurring at Nb_2O_5 electrode can be described by $Nb_2O_5 + xLi^+ + xe^- \leftrightarrow Li_xNb_2O_5$, where x ($0<x<2$) is the mole fraction of the inserted lithium ions. **Figure 4A** compares the representative cyclic voltammograms of pure Nb_2O_5, CNTs, and CNT/Nb_2O_5 composite using a sweep rate of 2 mV s^{-1}. The CNTs shows a typical double-layer capacitive performance; while the nanocrystals electrode shows symmetric cathodic and anodic peaks at around 1.5 V, indicating a reversible lithium intercalation and de-intercalation process. In contrast, the composite exhibits broader peaks, consisting with intercalation-type electrochemical reactions with broader distribution of energy. The larger area of within the CV curve indicates a higher capacitance, which is resulted from the conductive CNT networks that facilitate more effective electron transport and the current collection.

Figure 4B compares the charge storage of pure Nb_2O_5, CNTs, and CNT/Nb_2O_5 composite at sweeping rate of 1 to 50 mV s^{-1} (corresponding to charge/discharge times from 2000 to 40 s, respectively)(Figure S2). Obviously, the CNTs show a high rate capability but low capacitance contributed from the electrical double-layer capacitance. At 1 mV s^{-1}, the electrodes of CNTs and Nb_2O_5 nanocrystals show a capacity of 215 and 397 C g^{-1}, respectively. Simply adding the capacity contribution of each constituent component (CNTs and the nanocrystals) at this sweep rate would give a capacity of 361 C g^{-1}, which is significantly lower than the measured capacity for the composite electrode (445 C g^{-1}). Interestingly, the measured capacity of the composite electrode is even higher than that of the pure nanocrystal electrode, suggesting that the addition of the CNTs leads to improved charge transfer for the nanocrystals. This effect becomes more pronounced at higher scan rates. For example, at 50 mV s^{-1}, the pure Nb_2O_5 electrode exhibits only 31% (125 C g^{-1}) of the capacity measured at 1 mV s^{-1}. In contrast, the CNTs/Nb_2O_5 composite electrode exhibits substantially higher capacity (267 C g^{-1}) at 50 mV s^{-1}, which is 60% of its value at 1 mV s^{-1}.

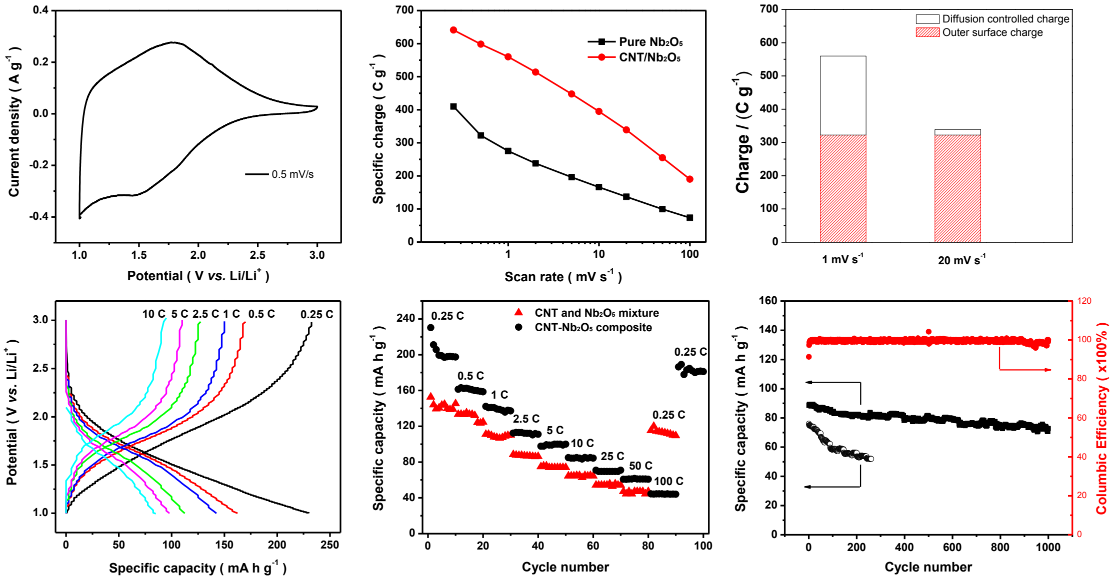

Figure 3.4 (A) Representative cyclic voltammograms of CNTs-Nb_2O_5 composites electrode at a scan rate of 0.5 mV s^{-1}; (B) Comparison of charge storage behaviors between CNTs-Nb_2O_5 composites electrode and pure Nb_2O_5 electrode; (C) Analysis of charge storage behavior of CNTs-Nb_2O_5 composites electrode; (D) charge/discharge curves of the composites electrode at various C-rates; (E) Rate performance of composites electrode; and (F) long-term cycling performance of the composites electrode and physically mixed composites electrode.

Such an excellent rate performance of CNT/Nb_2O_5 composite can also be observed from galvanostatic charge/discharge curves. **Figure 4D** shows charge/discharge curves of the composite at different C-rates (1C = 200 mA $g_{composite}^{-1}$). In good agreement with electrode based on pure Nb_2O_5, the typical sloped feature could be observed indicating the nature of intercalation-type electrochemical reaction, which means that the lithium intercalation remains a single-phase process after repeated cycling. The initial discharge capacity at 0.25C obtained is 232 mA h g^{-1}, corresponding to ~2.32 Li^+ intercalated into the composite. The CNT/Nb_2O_5 composite delivers a reversible capacity of ~160 and 85 mA h g^{-1} at a rate of 0.5C and 10C, respectively.

Remarkably, the composite electrode retains a high capacity even at an extremely high rate. As shown in **Figure 4E**, the composite still possesses a specific capacity of ~60 mA h g^{-1} at a rate of 50C (corresponding to charge/discharge in 10 s). Even at 100C (charge/discharge in

4 s), a capacity of 40 mA h g^{-1} still remains, which is the best data reported so far.

In addition to the enhanced rate capability, the CNT/Nb_2O_5 composite also exhibits impressive cycling properties. **Figure 4F** displays a long-term cycling performance of the composite electrode. It retains a specific capacity of ~80 mA h g^{-1} after 1000 cycles at a rate of 5C, more than 80% of its initial capacity remains. The gradual capacity fading might be caused by increased loss of active materials and irreversible reactions. By comparison, simply mixing pure Nb_2O_5 and CNTs leads to the electrode with poor cycling stability. At the same 5C-rate, the mixture electrode shows a dramatic capacity deterioration.

The durable performance of the electrodes is attributed to their robust structure, which can be probed using electrochemical impedance spectroscopy (EIS) study. Nyquist plots of the CNT–NC electrodes at different cycling status are shown in SI, Figure S6. It was found that the fresh electrode exhibits a relatively large single semicircle and an intercept at high frequency range, which is associated with a combination of ohmic and charge-transfer resistance. The low-frequency Warburg tail presents a relatively low slope, implying a surface-wetting process is required for such thick electrodes (over 100 The diameter of the semicircle decreases and the slope of the Warburg tail increases dramatically after 10 cycles at 1C, indicating a decreased charge-transfer resistance and improved lithium-diffusion rate (see insets). The impedance behavior shows similar features after 400 cycles, confirming the robust electrode structure. After cycling at high rate (20C) for 200 cycles followed by 100 cycles at 2C, slight increase of diffusion resistance can be detected from the Warburg region. Nevertheless, the total electrode resistance remains small due to the robust CNT network, which is consistent with its excellent long-term cycling stability.

To further verify the role of the CNT–NC intimate structure in the electrode performance, we also made electrodes using the traditional process in which binder was used. In this work, TiO2 NC powders were mixed with CNTs at a mass ratio of 3:1; the mixture was sintered at the same condition as that used for the CNT–NC hybrid electrode. The resulted powder was used to fabricate the electrodes with TiO2, CNTs, carbon and binder at a mass ratio of 3:1:1:1, which provided comparable TiO2 content with the 3D CNT–NC electrodes. **Figure 4A** shows a representa- tive SEM image of this electrode. Significantly different from the conformal CNT–NC electrodes, such electrodes display appreciable NC aggregation without a clear CNT conductive scaffold. Consistently, such electrodes show much larger impedance (~80 than those of the conformal electrodes (55 in the first cycle (Figure 4B). After 10 cycles of galvanostaic charge–discharge,

3.3. Conclusion

In summary, we have developed nanocomposites of Nb_2O_5 nanocrystals and CNTs for supercapacitor application. This composite electrode architecture is based on in-situ growing Nb_2O_5 nanocrystals onto CNTs networks. Therefore, such electrodes possess high capacitance and excellent rate capability and cycling stability. This work provides an effective structure design by integrating metal-oxide nanocrystals and conductive CNTs networks into robust nanocomposite structure, which may be generalized to synthesize other nanocomposites for better-performance energy storage.

3.4. Experimental Section

Synthesis of Nb_2O_5 nanocrystals and CNTs/Nb_2O_5 nanocomposites: A one-pot hydrothermal method was used to synthesize Nb_2O_5 nanocrystals. In a typical reaction, ammonium niobate oxalate hydrate (0.2 g) and surfactant P123 ($EO_{20}PO_{70}EO_{20}$, where EO and PO are ethylene oxide and propylene oxide, respectively, 0.8 g) were dissolved in deionized water (60 mL) under ultrasonication for 30 min. HCl (2 M, 0.5 mL) was added into the solution before it was transferred to an 80 mL Teflon-lined autoclave and heated at 200 ºC for 24 h. The resulted precipitates were rinsed with water and ethanol and dried at 80 ºC for 12 h under vacuum. Multi-wall carbon nanotubes (CNTs) were functionalized by generating carboxylic groups on their surface using a method similar to that by Gao *et al.*.[17] Details of the materials synthesis were described in our previous publication.[15] X-ray diffraction (XRD) experiments were conducted on a X'Pert Pro X-ray diffractometer (Panalytical B.V.); scanning electron microscopic (SEM) experiments were conducted on a JEOL JSM-6700 FE-SEM (JEOL); transmission electron microscopic (TEM) experiments were conducted on a Philips CM120 operated at 120 kV (Philips/FEI), and high resolution TEM experiments were conducted on a

Titan STEM (Philips/FEI).

Electrode Fabrication and Electrochemical Measurements: Appropriate ratios of Nb_2O_5 nanocrystals and CNTs were dispersed in *N*-methylpyrrolidinone (NMP) and ultrasonicated to form homogeneous and stable dispersions, where PVDF and carbon black were also added. The composites with 10, 20 and 30 wt-% of the CNTs were denoted as CNC-10, CNC-20 and CNC-30, respectively. The CNT/Nb_2O_5 composites electrodes were prepared by coating the slurries containing 10 wt-% carbon black, 10 wt-% polyvinylidenedifluoride (PVDF) and 80 wt-% of the composites onto stainless steel current collectors. The electrodes were dried at a room temperature for 8 h and then annealed at 300 ºC for 5 h under N_2. The thickness of the electrodes can be controlled from ~1 to 20 microns. The activated carbon (AC) cathode was assembled with the same ratio of carbon black and PVDF. The activated carbon with a surface area of ~ 1,900 m^2 g^{-1} has a gravimetric capacitances of 110 F g^{-1} or 72 F g^{-1} at the scan rates of 1 and 50 mV s^{-1} respectively (**Figure 9**, Supporting Information).

Electrochemical measurements were carried out on a VMP3 potentiostat/galvanostat (Bio-Logic LLC, Knoxville, TN). The electrolyte solution was a 1 M $LiClO_4$ in propylene carbonate (PC) and lithium foils were used as both the counter and reference electrodes. Cyclic voltammetric (CV) measurements were carried out in an argon-filled glove box using cutoff voltages of 2.55 and 1.0 V versus Li^+/Li. The asymmetric device was assembled with an anode of composite electrode and a cathode of AC electrode, and built in an open cell. The capacities of the composite electrodes with different loadings at different scanning rates were shown in Figure S5 (Supporting Information). Asymmetric cells were charged and discharged between 3.0 and 0.5 V, and AC-based symmetric cells were charged and discharged between 2.7 and 0 V. The specific capacitance, power and energy density were calculated based on the total mass of anode and cathode materials. Energy density was calculated using $E = \frac{1}{2} CV^2$, where C is the total cell capacitance and V is the maximum cell potential.

Reference:

[1] B. E. Conway, *Electrochemical Supercapacitors; Scientific Fundamentals and Technological Applications*, Kluwer Academic/Plenum Pblishers, New York, **1999**.

[2] A. S. Arico, P. Bruce, B. Scrosati, J.-M. Tarascon, W. van Schalkwijk, *Nat. Mater.* **2005**, *4*, 366.

[3] L. L. Zhang, X. S. Zhao, *Chem. Soc. Rev.* **2009**, *38*, 2520.

[4] P.-C. Chen, G. Shen, Y. Shi, H. Chen, C. Zhou, *ACS Nano* **2010**, *4*, 4403.

[5] J. P. Zheng, *J. Electrochem. Soc.* **2003**, *150*, A484.

[6] C. M. Ionica-Bousquet, D. MuÒoz-Rojas, W. J. Casteel Jr, R. M. Pearlstein, G. G. Kumar, G. P. Pez, M. R. PalacÌn, *J. Power Sources* **2011**, *196*, 1626.

[7] S.-H. Kang, D. P. Abraham, W.-S. Yoon, K.-W. Nam, X.-Q. Yang, *Electrochim. Acta* **2008**, *54*, 684.

[8] J.-T. Han, D.-Q. Liu, S.-H. Song, Y. Kim, J. B. Goodenough, *Chem. Mater.* **2009**, *21*, 4753.

[9] J.-T. Han, Y.-H. Huang, J. B. Goodenough, *Chem. Mater.* **2011**, *23*, 2027.

[10] M. Wei, K. Wei, M. Ichihara, H. Zhou, *Electrochem. Commun.* **2008**, *10*, 980.

[11] A. L. Viet, M. V. Reddy, R. Jose, B. V. R. Chowdari, S. Ramakrishna, *J. Phys. Chem. C* **2009**, *114*, 664.

[12] K. Brezesinski, J. Wang, J. Haetge, C. Reitz, S. O. Steinmueller, S. H. Tolbert, B. M. Smarsly, B. Dunn, T. Brezesinski, *J. Am. Chem. Soc.* **2010**, *132*, 6982.

[13] J. P. Zheng, P. J. Cygan, T. R. Jow, *J. Electrochem. Soc.* **1995**, *142*, 2699.

[14] Y. U. Jeong, A. Manthiram, *J. Electrochem. Soc.* **2002**, *149*, A1419.

[15] Z. Chen, Y. Qin, D. Weng, Q. Xiao, Y. Peng, X. Wang, H. Li, F. Wei, Y. Lu, *Adv. Func. Mater.* **2009**, *19*, 3420.

[16] Z. Chen, V. Augustyn, J. Wen, Y. Zhang, M. Shen, B. Dunn, Y. Lu, *Adv. Mater.* **2011**, *23*, 791.

[17] C. Gao, C. D. Vo, Y. Z. Jin, W. Li, S. P. Armes, *Macromolecules* **2005**, *38*, 8634.

[18] N. Ozer, D.-G. Chen, C. M. Lampert, *Thin Solid Films* **1996**, *277*, 162.

[19] R. Kodama, Y. Terada, I. Nakai, S. Komaba, N. Kumagai, *J. Electrochem. Soc.* **2006**, *153*, A583.

[20] S. Ardizzone, G. Fregonara, S. Trasatti, *Electrochim. Acta* **1990**, *35*, 263.

[21] M. Toupin, T. Brousse, D. Belanger, *Chem. Mater.* **2002**, *14*, 3946.

[22] K. Naoi, *Fuel Cells* **2010**, *10*, 825.

[23] A. Burke, presented at Vehicle Power and Propulsion, 2005 IEEE Conference, The present and projected performance and cost of double-layer pseudo-capacitive ultracapacitors for hybrid vehicle applications, Chicago, Sept. **2005**.

[24] S. W. Lee, N. Yabuuchi, B. M. Gallant, S. Chen, B.-S. Kim, P. T. Hammond, Y. Shao-Horn, *Nat. Nano.* **2010**, *5*, 531.

[25] S. Eaves, J. Eaves, *J. Power Sources* **2004**, *130*, 208.

[26] G. B. Appetecchi, P. P. Prosini, *J. Power Sources* **2005**, *146*, 793.

[27] Advanced Capacitor Technologies, Inc., http://www.act.jp/eng/premlis/premlis.htm (accessed May, 2011).

[28] Telcordia Energy Storage Research Group, http://www.argreenhouse.com/ESR/ah (accessed May, 2011).

[29] R. Liu, S. B. Lee, *J. Am. Chem. Soc.* **2008**, *130*, 2942.

[30] R. Liu, J. Duay, S. B. Lee, *Chem. Comm.* **2011**, *47*, 1384.

4. Fabrication of Thin-Film Electrode from Building Nanocrystals for Microsupercapacitors

4.1. Introduction

Micro-power-sources, which are commonly based on thin-film batteries and supercapacitors, are essential for micro-electronics, such as non-volatile memory, smart sensors, radio frequency identification tags (RFIT), implantable medical devices and micro-electromechanical systems (MEMS).1 Their current fabrication mainly relies on complicated processes that often involve the use of expensive equipment with high operation cost, leading to solid-state devices often with low rate-capability and poor durability.2 Although lower-cost micro-supercapacitors could also be made from activated carbons with higher power,1c activated carbons generally possess large particle size in the range of microns, which limits their use for thin devices. Note that thinner carbon-based devices may be made by controlled etching of metal carbide films.1d Such an etching process, however, brings up the fabrication cost significantly. In addition, such carbon-based devices are generally operated based on double-layer capacitance, which offers energy densities that are much lower than those of micro-batteries.

Towards better micro-devices, one promising direction is to fabricate micro-pseudocapacitors using thin films of transition metal oxides. Compared with the carbon-based devices, such devices could store a significantly larger amount of charge by fast redox reactions, providing new opportunities for high-energy and high-power micro-devices. For example, thin-films of RuO_2 and MnO_2 may provide specific capacitance up to 700 and 1200 F g^{-1},[3] respectively, which is an-order-of-magnitude larger than those of the carbon materials (∼100–200 F g^{-1}).[4] However, current fabrication of such RuO_2-based thin films relies on the electrophoresis deposition techniques[3a] or an evaporation-induced self-assembly process with the aid of copolymers.[3b] Similarly, MnO_2 thin films were normally made by electrochemical deposition on porous metallic templates.[3c] Although other methods, including sputtering,[5a] pulse laser deposition[5b] and chemical vapor deposition,[5c] were also used to fabricate the oxide-based thin films, the processes developed so far are not effective enough for low-cost and large-scale device fabrication.

Herein, we report a facile coating technique that enables effective fabrication of high-performance micro-pseudocapacitor electrodes at low cost. Our strategy is based on a simple wet-chemical approach using nanocrystals (NCs) of transition metal oxides as the building materials. The past decade has witnessed a rapid advance in NCs synthesis; large families of NCs were effectively synthesized with controlled structure, morphology, and composition,[6] which offers a large variety of building NCs for the fabrication of micro-pseudocapacitors. To demonstrate this concept, NCs of lithium manganese oxide ($LiMn_2O_4$) was used as the model system.

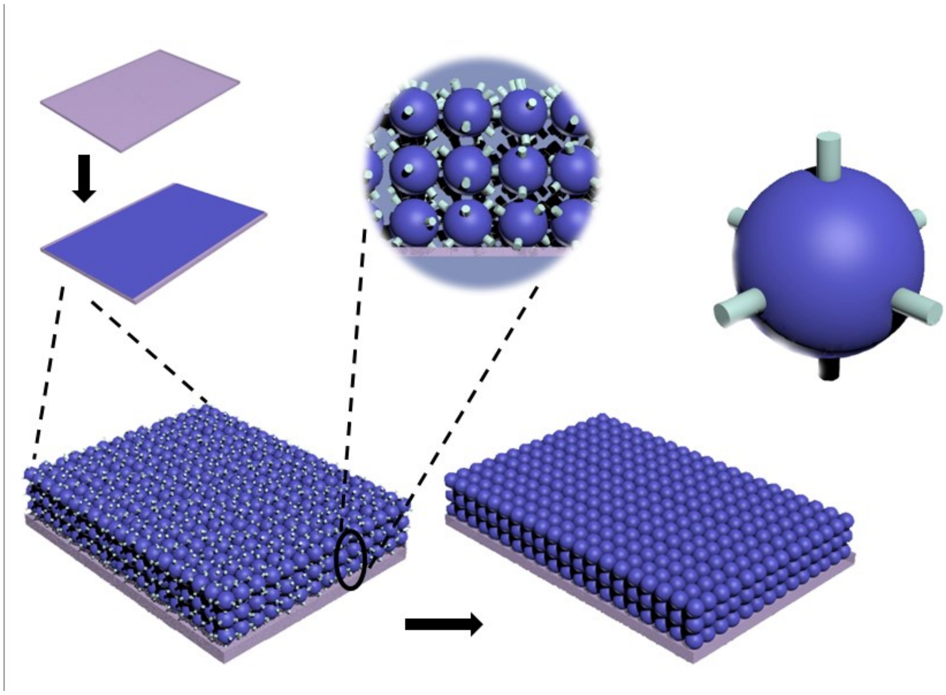

Figure 4.1 Scheme of forming thin-film electrode based on ultrafine $LiMn_2O_4$ nanocrystals.

4.2. Results and Discussion

Figure 1A displays a representative transmission electron microscopic (TEM) image of the as-synthesized ultrafine $LiMn_2O_4$ NCs. The nanocrystals are well dispersed and show relatively narrow size-distribution. An average crystal size is calculated to be 6.67±1.01 nm. Although the crystals are ultrafine, they are highly crystallized as shown in high-resolution TEM (inset, **Figure 1A**). **Figure 1B** shows x-ray powder diffraction patterns of as-synthesized NCs. The diffraction pattern matches well to that of spinel $LiMn_2O_4$ (according to JCPDS reference card No. 35-0782) with no obvious indications for α-MnO_2 or other impurities. The broadening of peaks originated from the small crystal size, which is calculated to be 5.87 nm from Scherrer equation, a little smaller than the average size observed from TEM. X-ray photoelectron spectroscopy was carried out to find the manganese valence. **Figure 1C** shows the core level experimental spectra for Mn 2*p* in $LiMn_2O_4$ NCs. The two peaks located at 652.4 (±0.2) eV and 640.7 (±0.2) eV correspond to Mn^{3+} and Mn^{4+}, respectively. The total peak area of Mn^{3+}

peak is slightly higher than that of the Mn^{4+}, which indicates the slightly higher content of the Mn^{3+} amount in the compound. Removal of the capping ligands creates a porous structure confirmed by the nitrogen adsorption–desorption isotherms shown in **Figure 1D**. It gives a type-IV isotherm with an H1-type hysteresis loop at a relative pressure between 0.45 and 0.9, which is typical of mesoporous structure. The calcined NCs exhibit a high Brunauer-Emmett-Teller (BET) surface area of ~136 m^2 g^{-1} and a pore diameter less than 8 nm. Overall, the above analysis indicates that the $LiMn_2O_4$ is ultrafine nanocrystals, which is critical for fast lithium insertion and extraction.

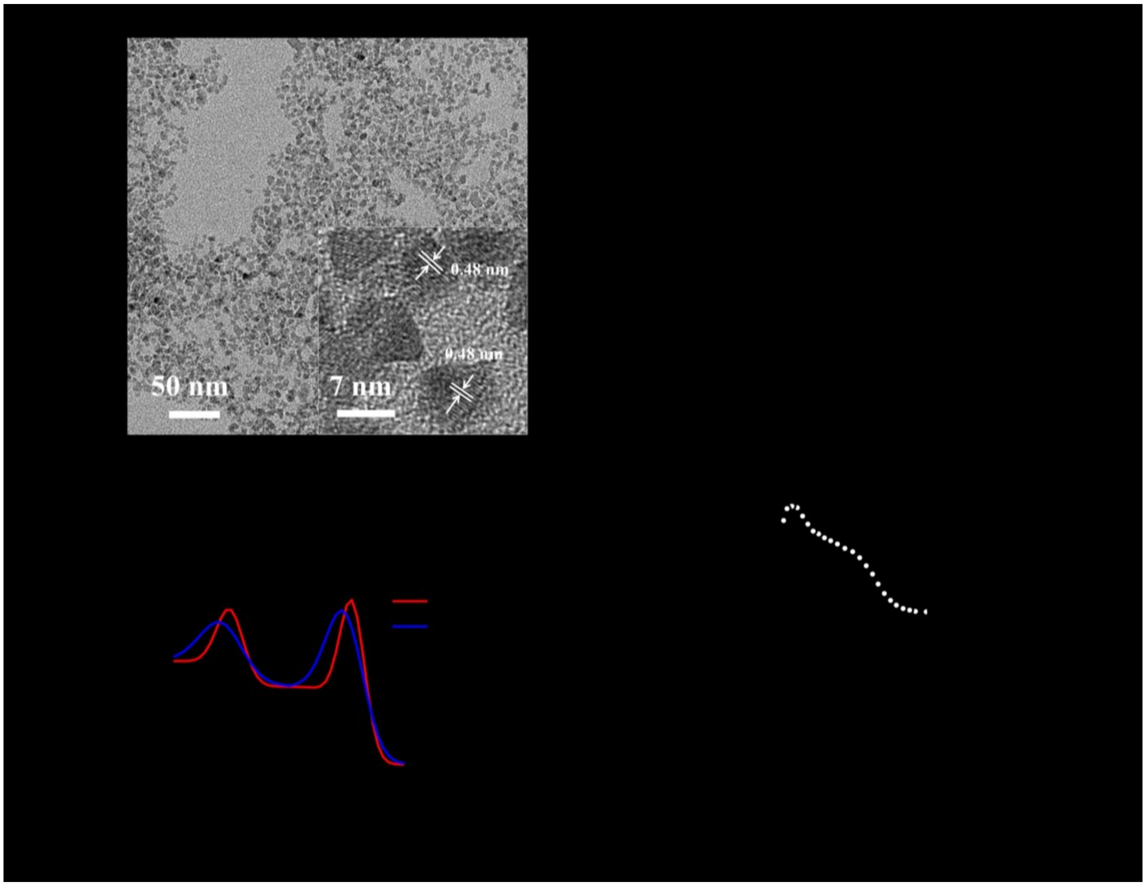

Figure 4.2 (A) Representative TEM image of as-synthesized $LiMn_2O_4$ NCs (inset: high-resolution TEM image of a few NCs showing (111) lattice); (B) XRD pattern of as-synthesized NCs; (C) Mn $2p_{3/2}$ and Mn $2p_{1/2}$ XPS spectra of $LiMn_2O_4$ NCs; (D) Nitrogen adsorption isotherms of $LiMn_2O_4$ NCs with sintering treatment (the inset shows the corresponding pore-size distribution).

Such ultrafine $LiMn_2O_4$ NCs can be well dispersed in toluene, forming homogeneous nano-ink stable for a few months without precipitation. The nano-ink can be coated on ITO substrate to form nanoporous thin film after the organic ligands removal (See **Figure 3**).

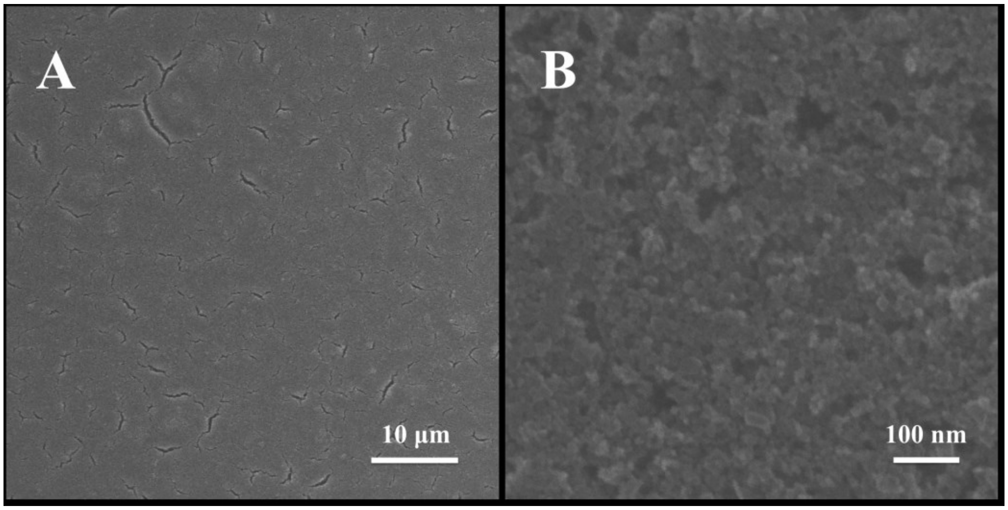

Figure 4.3 (A) Low- and (B) high-magnitude SEM images of $LiMn_2O_4$ NCs-based thin film after organic ligands removal at 450 ºC in air.

The electrochemical behavior of the $LiMn_2O_4$ NCs-based thin film was investigated using three-electrode cells, in which lithium foils were used as both the counter and the reference electrodes. Charge storage behavior was characterized by cyclic voltammetry (CV). **Figure 4A** shows the representative cyclic voltammograms for thin film electrodes at a sweep rate of 0.2 mV s^{-1} for the 1st and 2nd cycles. The electrochemical Li^+ insertion and extraction process occurring at spinel $LiMn_2O_4$ electrodes can be expressed by $LiMn_2O_4 \leftrightarrow Li_{1-x}Mn_2O_4 + xLi^+ + xe^-$, where x is the mole fraction of the inserted lithium ions.[24] Two well-defined current peaks are observed at 4.01 and 4.15 V for cathodic reaction, and 3.97 and 4.11 V for anodic reaction, respectively, which are corresponding to the typical reversible electrochemical Li+ insertion/extraction from the tetrahedral sites of spinel $LiMn_2O_4$.[25] This further confirms the formation of spinel $LiMn_2O_4$ NCs. The area under the CV curve represents the total stored charge on the electrode during charge-discharge process. The ultrafine NCs-based thin film electrodes exhibit a high rate capability calculated from CV curves at various sweep rates from 0.2 to 5 mV s^{-1} (**Figure 5**). For example, the thin film electrode possesses 275 C g^{-1} at 1 mV s^{-1}, and still preserves ~253 C g^{-1} (~70 mA h g^{-1}) at 5 mV s^{-1} (corresponding to a charge-discharge time of 3.6 min), around 92% capacity retention can be achieved.

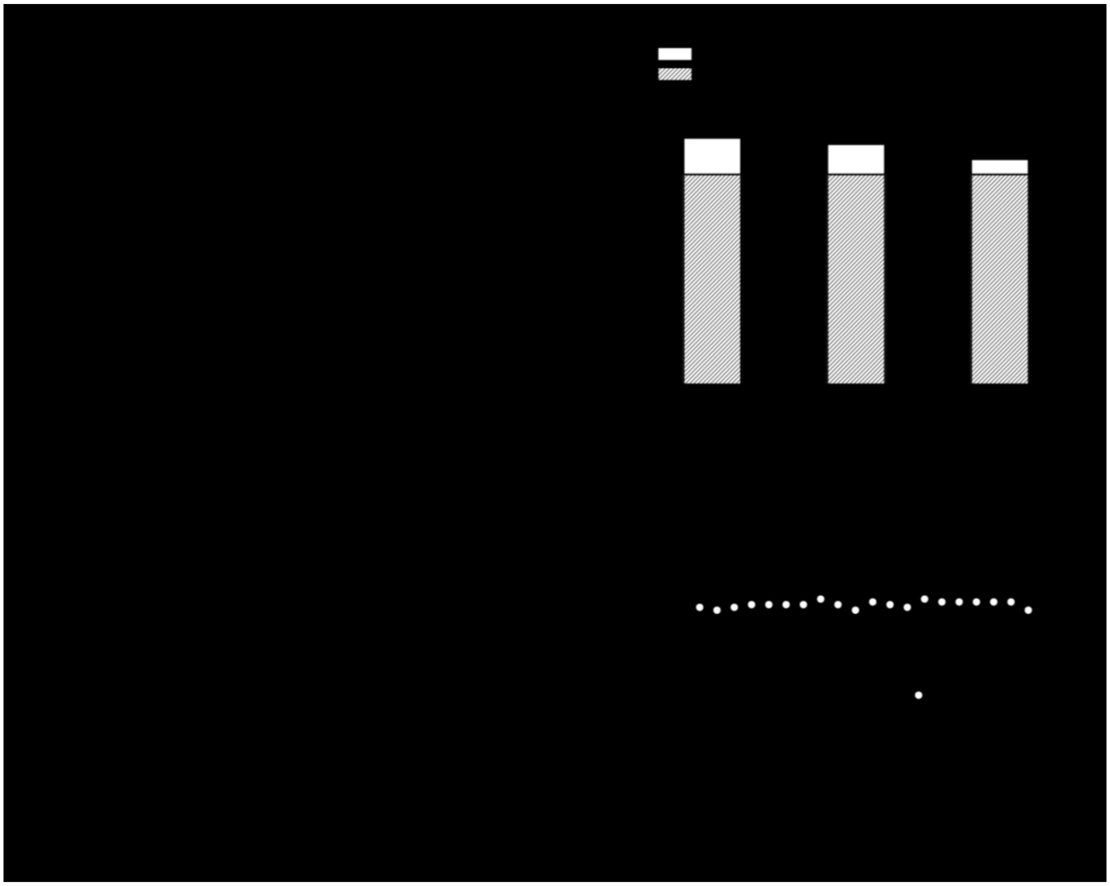

Figure 4.4 (A) CV plots of thin film electrode for the 1st and 2nd cycles at the sweep rate of 0.2 mV s^{-1}; (B) Comparison of the total charge stored at the scan rates of 1, 2, and 5 mV s^{-1}; (C) Galvanostatic charge-discharge curves of the thin film electrode at current density of (a) 26.9 mA g^{-1}, (b) 58.6 mA g^{-1} and (c) 114.4 mA g^{-1} in 1 M $LiClO_4$ at room temperature; and (D) Cycling performance of the thin film electrode at the current density of 50 mA g^{-1}.

To elucidate how these ultrafine NCs can provide a superior rate capability, we borrow idea from Trasatti's method[26] to analyze the contribution of the total charge stored on the electrode. Based on this method, the total voltammetric charge (q_T) of the electrode materials was separated into two parts: surface charge (q_s) and diffusion controlled charge (q_d) by:

$$q_T = q_s + q_d \quad (1)$$

where q_s is the stored charge that related to the accessible outer surface, while q_d mainly depends on the lithium intercalation inside the bulk crystal. Based on the semi-infinite linear diffusion law, within a reasonable range of sweep rates, q_s can be derived by plotting the total voltammetric charge q_T against the reciprocal of the square root of the potential sweep rate (v) and extrapolating v to ∞, according to the following equation:

$$q_T = q_s + k^*(v^{-1/2}) \quad (2)$$

A separation of surface and diffusion controlled charge contribution to total capacity is displayed in **Figure 4B.** It clearly shows that the ultrafine NCs based thin film electrode possesses a high surface contribution of 235 C g^{-1} (~65 mA h g^{-1}), which accounts for 85 % of the total capacity at 1 mV s^{-1} and 93 % at 5 mV s^{-1}, playing an important part at various sweep rates. Such a large fraction of q_s is mainly resulted from the fast kinetics by reducing the particle size and increased interface between active materials and the electrolyte. As a result, the rate capability can be significantly improved by alleviating the slow diffusion process. This phenomenon can also be observed in galvanostatic charge-discharge curves of the thin film electrode, as shown in **Figure 4C**. At low current density (long charge-discharge time), two distinct plateaus appear in both the charge and discharge curves, corresponding to two different Li^+ insertion/extraction process of $LiMn_2O_4$, which is also consistent with the CV result. In comparison, the slope feature of the charge-discharge curves without obvious plateaus at high current density (short charge-discharge time) show capacitive-like character, indicating that most of the charge stored on the thin film electrode involves in the Li^+ intercalation on the "outer" surface of the ultrafine NCs. Besides, the ultrafine NCs based thin film electrode also shows an improved cycle performance (**Figure 4D**). No obvious capacity fading can be observed for the first 20 cycles during the charge-discharge at a current density of 50 mA h g^{-1}.

[redacted]

Figure 4.5 CV plots of thin film electrode at various sweep rates from 0.2 to 5.0 mV s^{-1} in 1 M $LiClO_4$ in PC solution at room temperature.

4.3. Conlusion

References:

1. B. Xu, D. Qian, Z. Wang and Y. S. Meng, *Materials Science and Engineering: R: Reports*, 2012, **73**, 51-65.
2. S. Yang, Y. Song, K. Ngala, P. Y. Zavalij and M. Stanley Whittingham, *Journal of Power Sources*, 2003, **119,Äì121**, 239-246.
3. M. M. Thackeray, P. J. Johnson, L. A. de Picciotto, P. G. Bruce and J. B. Goodenough, *Materials Research Bulletin*, 1984, **19**, 179-187.
4. W. Liu, G. C. Farrington, F. Chaput and B. Dunn, *Journal of The Electrochemical Society*, 1996, **143**, 879-884.
5. K. M. Shaju and P. G. Bruce, *Chemistry of Materials*, 2008, **20**, 5557-5562.

6. Y.-L. Ding, J. Xie, G.-S. Cao, T.-J. Zhu, H.-M. Yu and X.-B. Zhao, *Advanced Functional Materials*, 2011, **21**, 348-355.

7. Q. Qu, L. Fu, X. Zhan, D. Samuelis, J. Maier, L. Li, S. Tian, Z. Li and Y. Wu, *Energy & Environmental Science*, 2011, **4**, 3985-3990.

8. T. Doi, T. Yahiro, S. Okada and J.-i. Yamaki, *Electrochimica Acta*, 2008, **53**, 8064-8069.

9. J. Cabana, T. Valdds-Solis, M. R. Palacin, J. Oro-Sole, A. Fuertes, G. Marban and A. B. Fuertes, *Journal of Power Sources*, 2007, **166**, 492-498.

10. F. Jiao, J. Bao, A. H. Hill and P. G. Bruce, *Angewandte Chemie*, 2008, **120**, 9857-9862.

11. J.-y. Luo, Y.-g. Wang, H.-m. Xiong and Y.-y. Xia, *Chemistry of Materials*, 2007, **19**, 4791-4795.

12. D. K. Kim, P. Muralidharan, H.-W. Lee, R. Ruffo, Y. Yang, C. K. Chan, H. Peng, R. A. Huggins and Y. Cui, *Nano Letters*, 2008, **8**, 3948-3952.

13. E. Hosono, T. Kudo, I. Honma, H. Matsuda and H. Zhou, *Nano Letters*, 2009, **9**, 1045-1051.

14. H.-W. Lee, P. Muralidharan, R. Ruffo, C. M. Mari, Y. Cui and D. K. Kim, *Nano Letters*, 2010, null-null.

15. D. Kovacheva, H. Gadjov, K. Petrov, S. Mandal, M. G. Lazarraga, L. Pascual, J. M. Amarilla, R. M. Rojas, P. Herrero and J. M. Rojo, *Journal of Materials Chemistry*, 2002, **12**, 1184-1188.

16. P. Ragupathy, H. N. Vasan and N. Munichandraiah, *Materials Chemistry and Physics*, 2010, **124**, 870-875.

17. X. Wang, G. Li, Z. Chen, V. Augustyn, X. Ma, G. Wang, B. Dunn and Y. Lu, *Advanced Energy Materials*, 2011, **1**, 1089-1093.

18. Z. Chen, D. Zhang, X. Wang, X. Jia, F. Wei, H. Li and Y. Lu, *Advanced Materials*, 2012, **24**, 2030-2036.
19. H. Xia, K. R. Ragavendran, J. Xie and L. Lu, *Journal of Power Sources*, 2012, **212**, 28-34.
20. M. Tang, A. Yuan, H. Zhao and J. Xu, *Journal of Power Sources*, 2013, **235**, 5-13.
21. X. Zhao, C. M. Hayner and H. H. Kung, *Journal of Materials Chemistry*, 2011, **21**, 17297-17303.
22. S.-M. Bak, K.-W. Nam, C.-W. Lee, K.-H. Kim, H.-C. Jung, X.-Q. Yang and K.-B. Kim, *Journal of Materials Chemistry*, 2011, **21**, 17309-17315.
23. S. Lee, Y. Cho, H.-K. Song, K. T. Lee and J. Cho, *Angewandte Chemie International Edition*, 2012, **51**, 8748-8752.
24. M. B. Sassin, S. G. Greenbaum, P. E. Stallworth, A. N. Mansour, B. P. Hahn, K. A. Pettigrew, D. R. Rolison and J. W. Long, *Journal of Materials Chemistry A*, 2013, **1**, 2431-2440.
25. X. Zhao, M. V. Reddy, H. Liu, S. Ramakrishna, G. V. S. Rao and B. V. R. Chowdari, *RSC Advances*, 2012, **2**, 7462-7469.
26. S. Ardizzone, G. Fregonara and S. Trasatti, *Electrochimica Acta*, 1990, **35**, 263-267.

5. Ultrafine $LiMn_2O_4$ Nanocrystals as Building Blocks for High-Power Lithium Battery Cathode

5.1. Introduction

The increasing demand for rechargeable lithium-ion batteries with high-power performance brings tremendous interest in development of cathode materials, which play an important role in the determination of lithium-ion transportation rate, as well as cell voltage and capacity.[1, 2] Among various types of cathode candidates, spinel $LiMn_2O_4$ has been considered highly promising on account of its natural abundance, environmental benignity, better safety, and its theoretical capacity of 148 mA h g^{-1}.[3, 4] However, the applications of $LiMn_2O_4$-based electrodes are still limited in high-power systems. The main reasons involve in the lack of efficient synthesis of high-quality $LiMn_2O_4$ and the fabrication of fast kinetic electrodes.[5-7]

To date, tremendous efforts have been dedicated to synthesizing nanostructured $LiMn_2O_4$, which not only shortens the diffusion path of lithium ions but also ensures a high surface area allowing the well contact between active material and electrolyte.[8, 9] For example, ordered mesoporous $LiMn_2O_4$ cathodes[10, 11] have been successfully prepared by templating method, while $LiMn_2O_4$ nanorods[12] and nanowires[13, 14] can be synthesized from hydrothermal with following cation exchange and post treatment. Although these nanomaterials exhibit a good rate capability, the syntheses are generally complex and costly. Other approach such as combustion[15] and microwave[16] have also been reported, however, well-defined nanocrystals with narrow size distribution are hard to obtain, which are critical for high performance cathodes. On the other hand, design of electrodes with fast kinetics is also crucial for high power density.[17,

[18] Most research mainly involves in combination of $LiMn_2O_4$ with conductive scaffolds built from different carbon such as carbon nanotubes (CNTs)[19, 20] and graphene.[21] For example, graphene/$LiMn_2O_4$[22] and carbon-coated $LiMn_2O_4$[23] nanocomposites electrodes still possesses around 100 mA h g^{-1} and 80 mA h g^{-1} at 100 C-rate, respectively. However, the fabrication of such electrodes was inefficient with extremely low active-material loading in the form of ultra-thin coating.

Herein, we report the synthesis of ultrafine $LiMn_2O_4$ NCs through a facile two-phase approach, and the fabrication of high-power cathodes based on such NCs building blocks. As illustrated in **Figure 1**, these ultrafine NCs capped with organic ligands possess a highly hydrophobic surface, and can be well dispersed in organic solvent, forming homogeneous nano-ink. By casting a large amount of the same ink into pre-formed 3-D CNT paper substrates, freestanding and flexible thick electrodes can be fabricated. Post-sintering treatment removes all the organic ligands on the surface of NCs and enables fast ion access to the open channels in NCs onto various substrates. As-resulted electrodes show capacitive-like high rate-capability and long-term cycling stability, offering a material platform for high-rate lithium cathode.

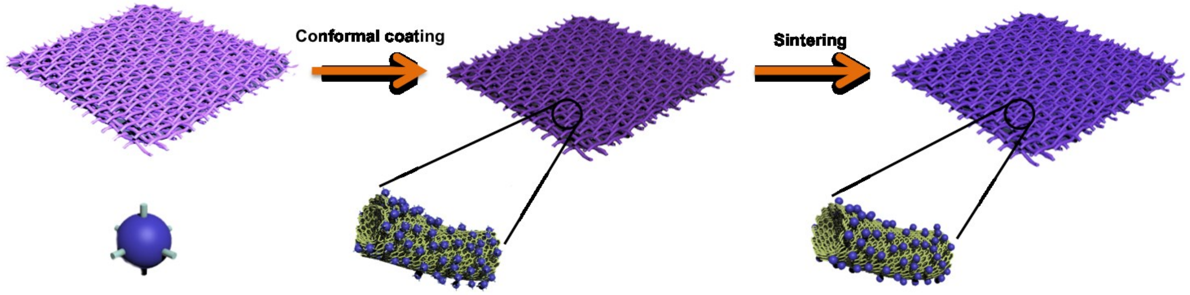

Figure 0.1 Schematic of forming flexible electrode based on ultrafine LiMn2O4 nanocrystals and preformed 3-D CNTs paper.

5.2. Results and Discussion

Figure 0.2 Digital photographs of a freestanding and highly flexible CNT-$LiMn_2O_4$ NCs electrode.

Compared with thin-film electrodes, NCs-based bulk electrodes have always been more attractive because they can store a large quantity of energy in a compact area or volume.[18] However, fabricating such electrodes is more difficult due to a lower density and increased contact resistance. Common solutions may mix more binder and conductive agent (normally 30-75 wt-%) with the active materials, though this process significantly sacrifices the overall capacity of the whole electrode. In contrast, by directly casting the ligand-stabilized $LiMn_2O_4$ NCs into a pre-formed three-dimensional (3-D) carbon nanotube (CNT) sheet, a bulk electrode with a high active material loading can successfully be constructed. Such a CNT sheet current collector with a thickness of ~ 100 μm has a density of ~3 mg cm^{-2}, which is about two orders of magnitude lighter than the aluminum foil used in a commercial lithium cathode.[18] Furthermore, as-resulted CNT/$LiMn_2O_4$ NCs hybrid electrodes are binder-free, freestanding and highly flexible (**Figure 2**). SEM image in **Figure 3** clearly shows the 3-D network structure of the electrode. The roughness of CNT surface reveals that the $LiMn_2O_4$ NCs are uniformly coated with slight aggregates.

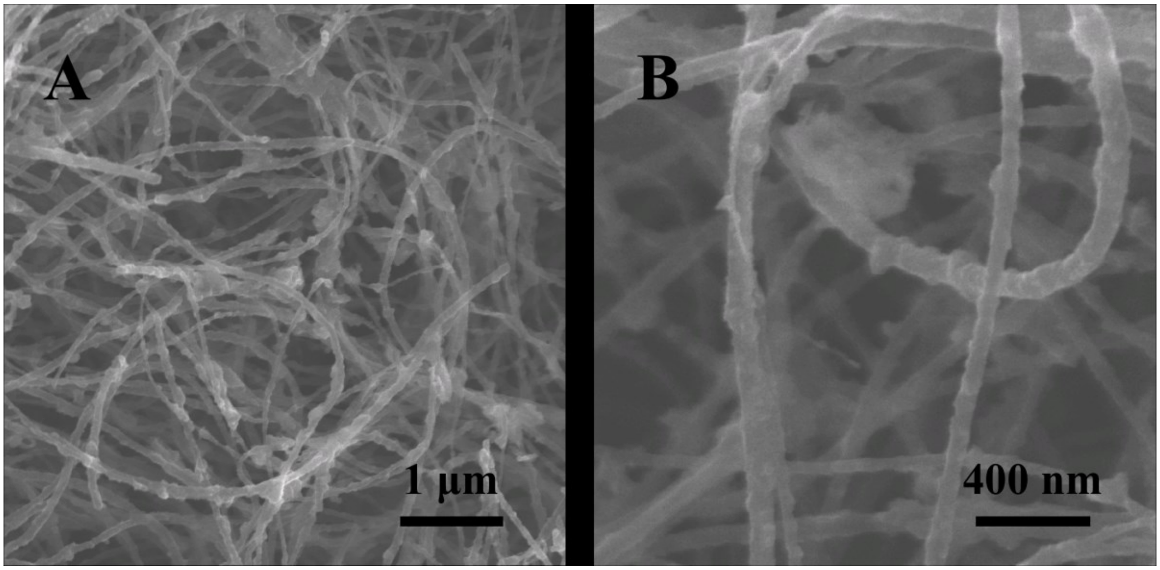

Figure 0.3 (A) Low magnification SEM image of a 3D CNT-$LiMn_2O_4$ NCs electrode showing the CNT scaffold coated with NCs; (B) High-magnification SEM image confirming the conformal coating of NCs on CNT surface.

Such a 3-D porous network structure endows the thick electrodes with excellent lithium storage performance. **Figure 4A** shows the representative CV curves for CNT/$LiMn_2O_4$ NCs hybrid electrode at a sweep rate of 0.5 mV s^{-1} for the first 3 cycles. In good agreement with the thin film electrodes, two pairs of cathodic/anodic peaks can be observed at 4.15/4.08 V and 4.01/3.95 V, respectively, providing a signature of a spinel $LiMn_2O_4$. To investigate the rate-capability, the electrode was charged and discharged at various C-rates. **Figure 4B** shows the galvanostatic charge-discharge curves of the hybrid electrode at 1 C, 5 C, and 20 C, respectively (1 C = 120 mA $g_{\text{hybrid electrode}}^{-1}$). The CNT/$LiMn_2O_4$ NCs electrode exhibited a charge capacity of 108 mA h g^{-1} and a discharge capacity of 102 mA h g^{-1} at 1 C rate. Correspondingly, the electrode retained 91.2 % charge capacity at 5 C (9.3 min), and 74.5 % charge capacity at 20 C (114 s). Even at 50 C (corresponding to charging time of ~ 30 s), the electrode still held a charge capacity of 50 mA h g^{-1}, implying that the hybrid electrode possessed excellent rate-capability. Such a rate performance is mainly attributed to the unique ultrafine NCs and the strong surface connectivity between the NCs and the CNT network. On one hand, the high surface area of ultrafine NCs allowing the well contact between electrolyte and the active material, allowing fast ion transportation. On the other hand, the intimate interaction between the $LiMn_2O_4$ NCs and the highly conductive CNTs ensures the fast electrons transportation.

Figure 0.4 Typical thermogravimetric analysis (TGA) curve for ultrafine $LiMn_2O_4$ NCs over temperature range.

Figure 4C compares the rate performance of the binder-free CNT/$LiMn_2O_4$ NCs hybrid electrode with several high-rate $LiMn_2O_4$-based electrodes from literatures.[26-31] Although some $LiMn_2O_4$-based materials can also achieve high rate-capability, the overall capacity of these electrode are sacrificed a lot by using a large amount of conductive agents, binder, and the metal current collector. For example, a carbon-coated single-crystal $LiMn_2O_4$ nanoparticles cluster based electrode (16 μm thick)[23] could deliver a discharge capacity of 121 and 108 mA h g^{-1} at 1 C and 50 C based on active material. Once considering the total effective mass, the capacity decreases to 79 and 70 mA h g^{-1}; once considering the mass of aluminum current collector, the real capacity of the electrode even decreases to only ~ 24 and ~ 21 mA h g^{-1}. In comparison, the binder-free CNT/$LiMn_2O_4$ NCs hybrid electrode provides a discharge capacity of 102 mA h g^{-1} at 1 C and 55 mA h g^{-1} at 50 C based on the mass of total cathode electrode, since the CNT network serves as both the conductive agent and the current collector.

Besides the outstanding rate performance, the CNT/$LiMn_2O_4$ NCs hybrid electrode also shows an impressive cycling stability. **Figure 4D** displays the discharge and discharge capacity retentions of the electrode at 5 C-rate for 100 cycles after the rate performance test. The electrode exhibited a very high stability during the cycling. After 100 cycles, ~ 91.2 % of both discharge and charge capacities could still be retained. In addition, the electrode also exhibited a high Coulombic efficiency, indicating the highly stable surface of the CNT/$LiMn_2O_4$ NCs cathode. This result is mainly due to the strong interaction between the stable CNT network structure and the surface of the $LiMn_2O_4$ NCs, which has not only improved the conductivity but also prevented the loss of active materials and irreversible reactions.

5.3. Conclusion

In conclusion, we have demonstrated a type of binder-free electrode based on ultrafine $LiMn_2O_4$ NCs synthesized through a two-phase reaction. The electrodes exhibits outstanding lithium storage performance, mainly arising from the surface effect of the unique ultrafine NCs. The strong surface connectivity between super-long CNT network and NCs in CNT/ $LiMn_2O_4$ NCs hybrid electrode ensures the fast electrons transport, enabling the electrode with excellent rate performance and high stability.

5.4. Experimental

Synthesis of $LiMn_2O_4$ NCs: The $LiMn_2O_4$ NCs were synthesized using a two-phase hydrothermal reaction. In a typical synthesis, 1.0 g of lithium hydroxide monohydrate was dissolved in 30 mL of water and the solution was transferred into a 100 mL Teflon-line stainless-steel autoclave. Subsequently, 0.2 g of manganese (II) stearate and 1.5 g of dodecylamine were dissolved in 30 mL of toluene in air and the solution was transferred into the autoclave without any stirring. The autoclave was sealed and maintained at 170 °C for 8 h and cooled to room temperature with tap water. The crude solution of $LiMn_2O_4$ NCs was precipitated with methanol and further isolated by centrifugation and decantation. The purified $LiMn_2O_4$ NCs were re-dispersed in toluene to form a NCs ink with desired concentration.

Fabrication of $LiMn_2O_4$ NCs thin films and binder-free CNT/$LiMn_2O_4$ hybrid electrode: To make thin films, 5 μL of 5 wt-% NC ink was directly coated on clean indium tin oxide (ITO) substrates. After solvent evaporation at room temperature, the films were sintered at 450 °C for 2h at a ramp rate of 2 °C min^{-1} under moist nitrogen to remove the ligands (**Figure S5†**). Such thin films have an active mass density of ~ 0.2 mg cm^{-2}. To fabricate binder-free CNT/TiO_2 hybrid electrodes, we made super-long CNT paper sheet reported previously.[18] 50 μL of 5 wt-% NC ink was directly casted in to the CNT current collectors and the solvent was automatically evaporated in air. This process was repeated to increase the $LiMn_2O_4$ loading. Then the electrodes were sintered at 450 °C for 2h at a ramp rate of 2 °C min^{-1}, resulting in flexible, binder-free and light-weight CNT/$LiMn_2O_4$ hybrid electrodes. The loading of $LiMn_2O_4$ was further confirmed by TGA and comparing the mass difference between the CNT sheet and CNT/ $LiMn_2O_4$ hybrid electrode.

Material and Electrode Characterization: The X-ray diffraction measurements were taken on Panalytical X'Pert Pro X-ray powder diffractometer using the copper Kα radiation (λ=1.54 Å). Scanning electron microscopy (SEM) experiments were conducted on a JEOL JSM-6700 FE-SEM. Transmission electron microscopy (TEM) experiments were conducted on a Philips CM120 operated at 120 kV.

To test thin films, CV measurements were carried out in three-electrode flood cells in an argon-filled glove box. The measurements were carried out on a Solartron 1860/1287 electrochemical interface. The electrolyte solution was a 1 M $LiClO_4$ in propylene carbonate (PC) solution and lithium foils were used as both the counter and reference electrodes. To evaluate binder-free CNT/TiO_2 hybrid electrodes, 2032-type coin cells were assembled in the glovebox. To make coin cells, glass fiber (GF/D) from Whatman was used as the separator; lithium foils were used as both the counter and the reference electrodes; and 1 M $LiPF_6$ in a 1:1 (w/w) mixture of ethylene carbonate and diethyl carbonate was used as the electrolyte. Galvanostatic charge-discharge measurements were carried out on a LAND CT2000 battery tester at different rates.

Reference:

1. B. Xu, D. Qian, Z. Wang and Y. S. Meng, *Materials Science and Engineering: R: Reports*, 2012, **73**, 51-65.
2. S. Yang, Y. Song, K. Ngala, P. Y. Zavalij and M. Stanley Whittingham, *Journal of Power Sources*, 2003, **119,Äì121**, 239-246.
3. M. M. Thackeray, P. J. Johnson, L. A. de Picciotto, P. G. Bruce and J. B. Goodenough, *Materials Research Bulletin*, 1984, **19**, 179-187.
4. W. Liu, G. C. Farrington, F. Chaput and B. Dunn, *Journal of The Electrochemical Society*, 1996, **143**, 879-884.
5. K. M. Shaju and P. G. Bruce, *Chemistry of Materials*, 2008, **20**, 5557-5562.

6. Y.-L. Ding, J. Xie, G.-S. Cao, T.-J. Zhu, H.-M. Yu and X.-B. Zhao, *Advanced Functional Materials*, 2011, **21**, 348-355.

7. Q. Qu, L. Fu, X. Zhan, D. Samuelis, J. Maier, L. Li, S. Tian, Z. Li and Y. Wu, *Energy & Environmental Science*, 2011, **4**, 3985-3990.

8. T. Doi, T. Yahiro, S. Okada and J.-i. Yamaki, *Electrochimica Acta*, 2008, **53**, 8064-8069.

9. J. Cabana, T. Valdds-Solis, M. R. Palacin, J. Oro-Sole, A. Fuertes, G. Marban and A. B. Fuertes, *Journal of Power Sources*, 2007, **166**, 492-498.

10. F. Jiao, J. Bao, A. H. Hill and P. G. Bruce, *Angewandte Chemie*, 2008, **120**, 9857-9862.

11. J.-y. Luo, Y.-g. Wang, H.-m. Xiong and Y.-y. Xia, *Chemistry of Materials*, 2007, **19**, 4791-4795.

12. D. K. Kim, P. Muralidharan, H.-W. Lee, R. Ruffo, Y. Yang, C. K. Chan, H. Peng, R. A. Huggins and Y. Cui, *Nano Letters*, 2008, **8**, 3948-3952.

13. E. Hosono, T. Kudo, I. Honma, H. Matsuda and H. Zhou, *Nano Letters*, 2009, **9**, 1045-1051.

14. H.-W. Lee, P. Muralidharan, R. Ruffo, C. M. Mari, Y. Cui and D. K. Kim, *Nano Letters*, 2010, null-null.

15. D. Kovacheva, H. Gadjov, K. Petrov, S. Mandal, M. G. Lazarraga, L. Pascual, J. M. Amarilla, R. M. Rojas, P. Herrero and J. M. Rojo, *Journal of Materials Chemistry*, 2002, **12**, 1184-1188.

16. P. Ragupathy, H. N. Vasan and N. Munichandraiah, *Materials Chemistry and Physics*, 2010, **124**, 870-875.

17. X. Wang, G. Li, Z. Chen, V. Augustyn, X. Ma, G. Wang, B. Dunn and Y. Lu, *Advanced Energy Materials*, 2011, **1**, 1089-1093.

18. Z. Chen, D. Zhang, X. Wang, X. Jia, F. Wei, H. Li and Y. Lu, *Advanced Materials*, 2012, **24**, 2030-2036.

19. H. Xia, K. R. Ragavendran, J. Xie and L. Lu, *Journal of Power Sources*, 2012, **212**, 28-34.

20. M. Tang, A. Yuan, H. Zhao and J. Xu, *Journal of Power Sources*, 2013, **235**, 5-13.

21. X. Zhao, C. M. Hayner and H. H. Kung, *Journal of Materials Chemistry*, 2011, **21**, 17297-17303.

22. S.-M. Bak, K.-W. Nam, C.-W. Lee, K.-H. Kim, H.-C. Jung, X.-Q. Yang and K.-B. Kim, *Journal of Materials Chemistry*, 2011, **21**, 17309-17315.

23. S. Lee, Y. Cho, H.-K. Song, K. T. Lee and J. Cho, *Angewandte Chemie International Edition*, 2012, **51**, 8748-8752.

24. M. B. Sassin, S. G. Greenbaum, P. E. Stallworth, A. N. Mansour, B. P. Hahn, K. A. Pettigrew, D. R. Rolison and J. W. Long, *Journal of Materials Chemistry A*, 2013, **1**, 2431-2440.

25. X. Zhao, M. V. Reddy, H. Liu, S. Ramakrishna, G. V. S. Rao and B. V. R. Chowdari, *RSC Advances*, 2012, **2**, 7462-7469.

26. S. Ardizzone, G. Fregonara and S. Trasatti, *Electrochimica Acta*, 1990, **35**, 263-267.

6. Ultrafine $Li_4Ti_5O_{12}$ Nanocrystals as Building Blocks for High-Power Lithium Battery Anode

6.1. Introduction

Rechargeable lithium-ion batteries (LIBs) have been attracting tremendous attention as clean and recyclable power sources for electric vehicles (EVs) and hybrid electric vehicles (HEVs).[1] However, the performance of current LIBs cannot meet the requirements in electric transportation applications in terms of high power density, long cycle life and safety.[2] Generally, most commercial LIBs utilize carbonaceous products such as graphite as anode materials.[3] Its low lithiation potential at ~0.2 V (*vs.* Li/Li^+) is close to lithium stripping voltage,[4] which may lead to lithium plating and dendrite growth,[5] bringing significant safety concerns. In addition, the insulating solid-electrolyte interphase (SEI) layer formed below 1.0 V (vs. Li/Li^+)[6] and a ~9% volume variation during lithium insertion and extraction[7] result in not only the kinetic problem of LIBs but also a deterioration of cycle life. As an alternative anode material, spinel $Li_4Ti_5O_{12}$ possesses a relatively high working potential of ~1.5 V (*vs.* Li/Li^+) which avoids the formation of SEI.[8] Moreover, it has excellent cycling performance due to the zero-strain feature.[9] Although these advantages make $Li_4Ti_5O_{12}$ a promising anode candidate for long-life and safe LIBs, the implementation is still limited in high power density devices by its low electronic conductivity (~10^{-13} S cm^{-1}) and moderate Li^+ diffusion coefficient (10^{-9}~10^{-13} cm^2 s^{-1}).[10]

So far, extensive efforts have been dedicated to improving the rate performance of spinel

$Li_4Ti_5O_{12}$.[11] The most effective approaches include (1) tailoring the crystal size of $Li_4Ti_5O_{12}$ to efficiently reduce the paths for both the ions diffusion and electrons migration;[12] (2) building conductive matrix to enhance the electrode conductivity such as surface carbon coating[13] or preparing CNT-$Li_4Ti_5O_{12}$ composites.[14] Therefore, composites based on nano-sized $Li_4Ti_5O_{12}$ crystals and efficient conductive structures are considered to be ideal to realize high rate capability. For example, carbon-coated $Li_4Ti_5O_{12}$ delivers a high capacity of mA h g-1 at C. Although some wet chemistry methods size, the products suffer from poor crystalinity which is critical to the electrochemical performance.

Herein, we report a practical and efficient strategy for synthesizing $Li_4Ti_5O_{12}$/graphene nanocomposites, where ultrafine $Li_4Ti_5O_{12}$ nanocrystals with an average size of around 10 nm are intimately contacting to conducting graphene. As shown in **Figure 1**, ultrafine $Li_4Ti_5O_{12}$ nanocrystals and conductive carbon black are encapsulated in graphene forming a conductive outer shell. Moreover, the graphene sheets within the composites sphere and the carbon black entangle together forming an inner highly conductive network. Therefore, the $Li_4Ti_5O_{12}$/graphene hybrid nanostructures can provide fast ionic and electronic conduction, resulting in high rate performance.

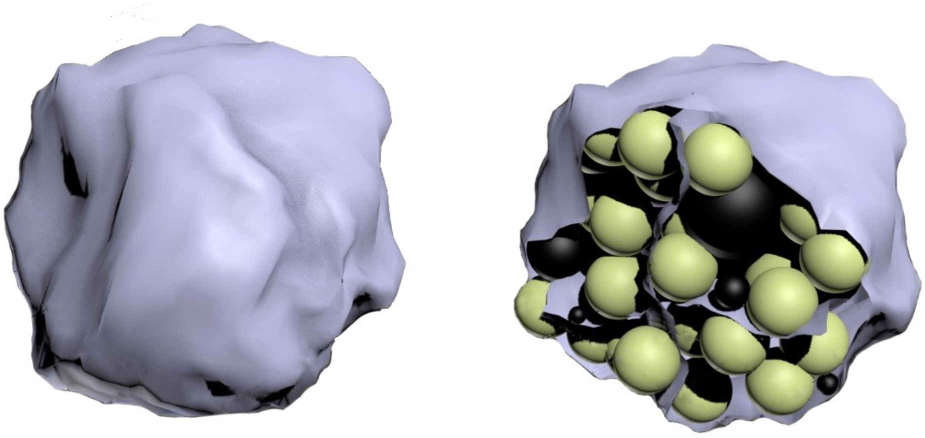

Figure 6.1 Scheme of $Li_4Ti_5O_{12}$/graphene nanocomposites

6.2. Results and Discussion

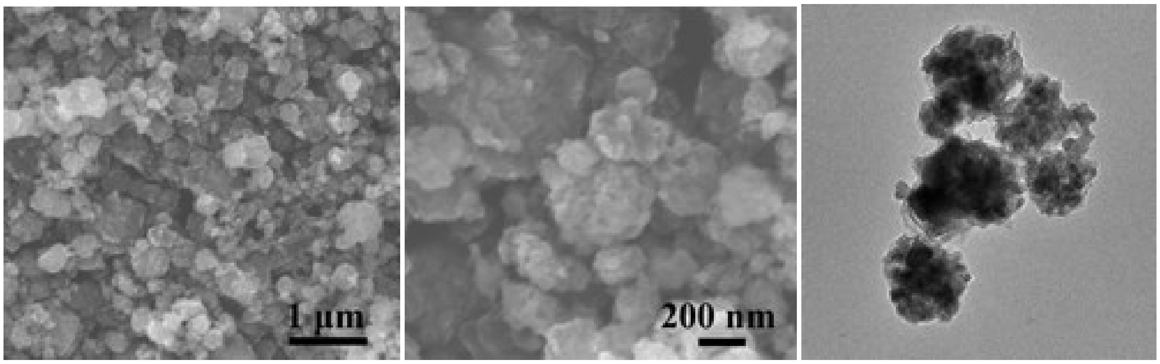

Figure 6.2 (A) Low- and (B) high-resolution SEM images and (C) TEM image of $Li_4Ti_5O_{12}$/graphene nanocomposites

Figure 2A shows the representative SEM image of $Li_4Ti_5O_{12}$/graphene nanocomposites after calcinating at 600°C in N_2. The composites spheres have an average size ranging from tens of nanometers to several microns. **Figure 2B** shows a high resolution SEM image of $Li_4Ti_5O_{12}$/graphene nanocomposites sphere. It can be found that all carbon blacks and ultrafine $Li_4Ti_5O_{12}$ are wrapped inside the graphene shell without separated or isolated particles can be observed. **Figure 2C** show a representative TEM image of the $Li_4Ti_5O_{12}$/graphene nanocomposites. It can be observed clearly that the highly crystalline $Li_4Ti_5O_{12}$ and amorphous carbon black are wrapped inside and the intimate contact between $Li_4Ti_5O_{12}$ and graphene, $Li_4Ti_5O_{12}$ and carbon black can form.

Figure 3 shows the XRD pattern of $Li_4Ti_5O_{12}$/graphene nanocomposites. The $Li_4Ti_5O_{12}$ possesses a cubic spinel structure, which is consistent with literatures. Peaks from TiO_2 can also be observed, indicating a small amount of TiO_2 exists.

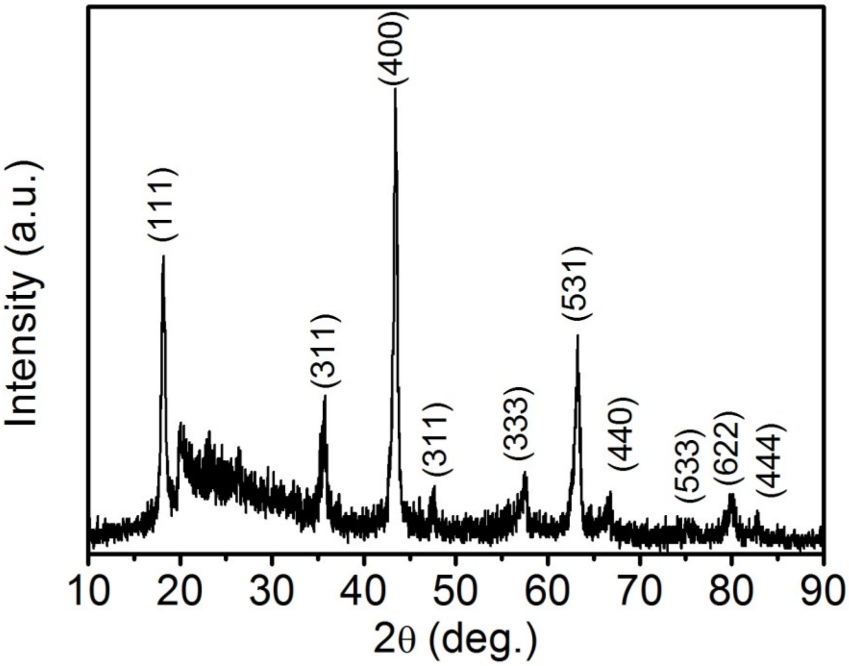

Figure 6.3 XRD pattern of $Li_4Ti_5O_{12}$/graphene nanocomposites after calcination at 600°C in N_2.

Such a $Li_4Ti_5O_{12}$/graphene nanocomposites electrode shows an excellent rate performance from galvanostatic charge/discharge curves. **Figure 4A** shows charge/discharge curves of the composite at different C-rates (1C = 175 mA $g_{composite}^{-1}$). The initial discharge capacity at 1 C obtained is 160 mA h g^{-1}. The $Li_4Ti_5O_{12}$/graphene nanocomposites electrode delivers a reversible capacity of ~110 at a rate of 30 C.

Remarkably, the composite electrode retains a high capacity even at an extremely high rate. As shown in **Figure 4B**, the composite still possesses a specific capacity of more than 90 mA h g^{-1} at a rate of 60 C. Even at 100 C, a capacity of ~80 mA h g^{-1} still remains, which is the best data reported so far.

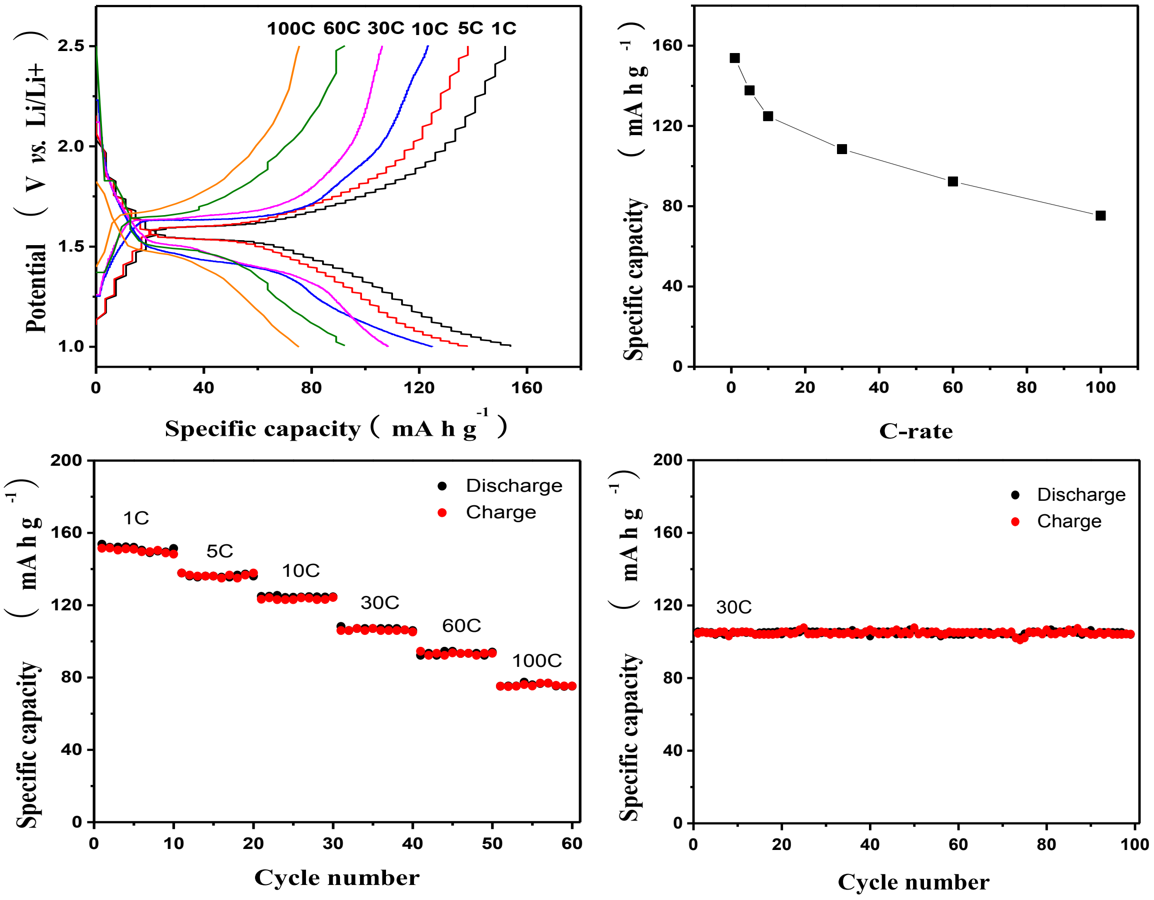

Figure 6.4 (A) Charge-discharge curves of $Li_4Ti_5O_{12}$/graphene nanocomposites electrode at various C-rates; (B) Rate performance of $Li_4Ti_5O_{12}$/graphene nanocomposites electrode; (C) $Li_4Ti_5O_{12}$/graphene nanocomposites at various C-rate from 1 C to 100 C; and (D) Cycling performance of $Li_4Ti_5O_{12}$/graphene nanocomposites electrode at 30 C-rate.

In addition to the enhanced rate capability, the CNT/Nb_2O_5 composite also exhibits impressive cycling properties. **Figure 4C** and **4D** displays a long-term cycling performance of the composite electrode. It retains a specific capacity of ~105 mA h g^{-1} after 100 cycles at a rate of 30 C, no obvious capacity decay can be observed.

The durable performance of the electrodes is attributed to their robust structure, which can be probed using electrochemical impedance spectroscopy (EIS) study. Nyquist plots at different cycling status are shown in SI, Figure S6. It was found that the fresh electrode exhibits a relatively large single semicircle and an intercept at high frequency range, which is associated with a combination of ohmic and charge-transfer resistance. The low-frequency Warburg tail presents a relatively low slope, implying a surface-wetting process is required for such thick electrodes (over 100 The diameter of the semicircle decreases and the slope of the Warburg tail increases dramatically after 10 cycles at 30C, indicating a decreased charge-transfer resistance and improved lithium-diffusion rate (see insets). The impedance behavior shows similar features after 400 cycles, confirming the robust electrode structure. After cycling at high rate (20C) for 200 cycles followed by 100 cycles at 2C, slight increase of diffusion resistance can be detected from the Warburg region. Nevertheless, the total electrode resistance remains small due to the robust CNT network, which is consistent with its excellent long-term cycling stability.

6.3. Conclusion

In conclusion, we have designed and synthesized a $Li_4Ti_5O_{12}$/graphene nanocomposites electrode architecture as an advanced anode material for high performance LIBs. The hybrid nanostructures endow the composites with high-rate transportation for both Li^+ and electrons (especially at high rates) because the hybrid nanostructure is capable of effectively utilising the good conductivity, high surface area, good electrochemical performance of graphene and the good stability of fine $Li_4Ti_5O_{12}$. It is the synergy of the two parts that leads to a high rate capability, high rate and stable lithium storage material.

6.4. Experimental Section

Synthesis of Graphene Oxide and Ultrafine $Li_4Ti_5O_{12}$ Precursors: Graphene oxide (GO) was prepared from powdered flake graphite (400 mesh) by a modified Hummers method as described previously. A two-phase solvo-thermal method was used to synthesize ultrafine $Li_4Ti_5O_{12}$

precursors. In a typical reaction, an aqueous solution (30 mL) containing $LiOH•H_2O$ (g) and *tert*-butylamine (mL) was transferred into a 100 mL Teflon-lined stainless steel autoclave. Subsequently, titanium n-propoxide (mL) and oleic acid (mL) were dissolved in toluene (30 mL) in air and the solution was transferred into the autoclave without any stirring. The autoclave was sealed and maintained at 180 ºC for 8 hrs. The resulted white precipitates were rinsed with ethanol and dried at 80 ºC for future use.

Synthesis of Graphene-$Li_4Ti_5O_{12}$ Nanocomposites: The graphene-$Li_4Ti_5O_{12}$ nanocomposites were synthesized through an aerosol process. In a typical reaction, GO (mg) and ultrafine $Li_4Ti_5O_{12}$ precursors (mg) as well as carbon black (mg) were homogeneously dispersed in DI water (80 mL) by ultrasonicating for 30 min and stirring overnight. The homogenous solution was sent through an atomizer using nitrogen as a carrier gas. The atomizer dispersed the solution into aerosol droplets, which were then passed through a ceramic tube that was heated to 450 Continuous solvent evaporation at the air/liquid interface of the aerosol droplets resulted in the formation of spherical nanocomposite particles. The particles were then collected on a membrane filter, and then sintered at 600 under N_2 in order to reduce the GO to graphene and form highly crystalline $Li_4Ti_5O_{12}$.

Material Characterization: X-ray diffraction (XRD) experiments were conducted on a X'Pert Pro X-ray diffractometer (Panalytical B.V.). Nitrogen sorption isotherms were measured at 77 K with a Micromeritics ASAP 2020 analyzer. The samples were degassed in vacuum at 200 ºC for 3 hrs. The specific surface areas were calculated by the Brunauer-Emmett-Teller (BET) method using adsorption branch in a relative pressure range from 0.04 to 0.25. The pore size distributions were derived from the adsorption branches of isotherms using the Barrett-Joyner-Halenda (BJH) model. Scanning electron microscopic (SEM) experiments were conducted on a JEOL JSM-6700 FE-SEM (JEOL); transmission electron microscopic (TEM) experiments were conducted on a Philips T12 cryo-electron microscope operated at 120 kV (Philips/FEI).

Electrode Fabrication: A conventional slurry-coating process was used to fabricate the electrodes. The graphene-$Li_4Ti_5O_{12}$ nanocomposite powder and polyvinylidenedifluoride (PVDF) binder were mixed in a mass ratio of 90:10 without any addition of extra carbon back and homogenized in *N*-methylpyrrolidinone (NMP) to form slurries. The homogeneous slurries were coated onto copper foil substrates and dried at 100 ºC for 2 hrs under vacuum. As formed electrodes were then pressed at a pressure of 2 MPa and further dried under vacuum at 100 ºC for another 6 hrs.

Electrochemical Measurements: To test electrodes, 2032-type coin cells were assembled in an argon-filled glovebox, using Celgard 2500 membrane as the separator, lithium foils as the counter electrodes, 1 M LiPF6 in a 1:1 (v/v) mixture of ethylene carbonate and diethyl carbonate as the electrolyte. Cyclic voltammetric (CV) measurements were carried out on a VMP3 potentiostat/galvanostat (Bio-Logic LLC, Knoxville, TN) using cutoff voltages of 3.0 and 1.0 V versus Li/Li^+ at different scan rates. The galvanostatic charge/discharge measurements were performed on LAND CT2000 (Wuhan Jinnuo Electronics, Ltd., Wuhan, China) at different current densities. Electrochemical impedance spectroscopy measurement was conducted on a Solartron 1860/1287 Electrochemical Interface. The Nyquist plots were recorded potentiostatically by applying an AC voltage of 10 mV amplitude in the frequency range of 0.01 to 100k Hz. All electrochemical measurements were carried out at room temperature.

References:

[1] A. S. Arico, P. Bruce, B. Scrosati, J.-M. Tarascon, W. V. Schalkwijk, *Nat. Mater.* **2005**, *4*,

366.

[2] P. Simon, Y. Gogotsi, *Nat. Mater.* **2008**, *7*, 845.

[3] A. Burke, *J. Power Sources* **2000**, *91*, 37.

[4] J. R. Miller, P. Simon, *Science* **2008**, *321*, 651.

[5] R. Kötz, M. Carlen, *Electrochim. Acta* **2000**, *45*, 2483.

[6] J. Chmiola, G. Yushin, Y. Gogotsi, C. Portet, P. Simon, P. L. Taberna, *Science* **2006**, *313*, 1760.

[7] C. C. Hu, W. C. Chen, K. H. Chang, *J. Electrochem. Soc.* **2004**, *151*, A281.

[8] M. Toupin, T. Brousse, D. Belanger, *Chem. Mater.* **2002**, *14*, 3946.

[9] J. W. Lang, L. B. Kong, W. J. Wu, Y. C. Luo, L. Kang, *Chem. Commun.* **2008**, 4213.

[10] G. G. Amatucci, F. Badway, A. D. Pasquier, T. Zheng, *J. Electrochem. Soc.* **2001**, *148*, A930.

[11] J. P. Zheng, *J. Electrochem. Soc.* **2003**, *150*, A484.

[12] T. Brezesinski, J. Wang, J. Polleux, B. Dunn, S. H. Tolbert, *J. Am. Chem. Soc.* **2009**, *131*, 8.

[13] T. Brezesinski, J. Wang, S. H. Tolbert, B. Dunn, *Nat. Mater.* **2010**, *9*, 146.

[14] A. E. Fischer, K. A. Pettigrew, D. R. Rolison, R. M. Stroud, J. W. Long, *Nano Lett.* **2007**, *7*, 281.

[15] S. W. Lee, N. Yabuuchi, B. M. Gallant, S. Chen, B. S. Kim, P. T. Hammond, Y. Shao-Horn, *Nat. Nano.* **2010**, *5*, 531.

[16] Z. Chen, Y. C. Qin, D. Weng, Q. F. Xiao, Y. T. Peng, X. L. Wang, H. X. Li, F. Wei, Y. F. Lu, *Adv. Funct. Mater.* **2009**, *19*, 3420.

[17] J. Livage, *Chem. Mater.* **1991**, *3*, 578.

[18] W. Dong, A. N. Mansour, B. Dunn, *Solid State Ionics* **2001**, *144*, 31.

[19] Y. S. Hu, X. Liu, J.-O. Müller, R. Schlögl, J. Maier, D. S. Su, *Angew. Chem. Int. Ed.* **2009**,

48, 210.

[20]K. Naoi, ‘Nanohybrid Capacitor’: The Next Generation Electrochemical Capacitors, *Fuel Cells* **2010**, 10, 825-833.

[21]S.-I. Pyun, J.-S. Bae, *J. Power Sources* **1997**, *68*, 669.

[22]W. Dong, J. Sakamoto, B. Dunn, *J. Sol-Gel Sci. Technol.* **2003**, *26*, 641.

[23]A. M. Cao, J. S. Hu, H. P. Liang, L. J. Wan, *Angew. Chem. Int. Ed.* **2005**, *44*, 4391.

[24]S. C. Pang, M. A. Anderson, T. W. Chapman, *J. Electrochem. Soc.* **2000**, *147*, 444.

[25]S. Passerini, J. J. Ressler, D. B. Le, B. B. Owens, W. H. Smyrl, *Electrochim. Acta* **1999**, *44*, 2209.

[26]F. Montilla, E. Morallon, A. De Battisti, J. L. Vazquez, *J. Phys. Chem. B* **2004**, *108*, 5036.

[27]Advanced Capacitor Techonologies, Inc., http://www.act.jp/-eng/premlis/- premlis.htm.

[28]Telcordia Energy Research group: http://www.argreenhouse.com/ESR/ah- main.html.

[29]A. F. Burke, Proc. IEEE Veh. Power Propulsion Conf. (VPPC"05), **2005**, 356.

[30]S. Eaves, J. Eaves, *J. Power Sources* **2004**, *130*, 208.

[31]G. B. Appetecchi, P. P. Prosini, *J. Power Sources* **2005**, *146*, 793.

[32]V. Khomenko, E. Raymundo-Piñero, F. Béguin, *J. Power Sources* **2006**, *153*, 183.

7. Preparation of Niobium and Vanadium Oxide Nanocomposites with Improved Rate Performance and Cycling Stability

7.1. Introduction

Lithium-ion batteries are essential power devices for portable systems, automotive applications and renewable energy storage.[1-3] Most commercial lithium-ion batteries utilize graphite as the anode with relatively high capacity (~372 mA h g^{-1}) and long cycling life.[4] However, its relatively low lithium-intercalation potential (~ 0.2 V versus Li/Li^+) may lead to lithium plating and dendrite growth, which brings significant safety concerns.[5] Moreover, carbon materials often exhibit low volumetric energy density resulted from low packing density.[6] By comparison, transition-metal oxides, such as lithium titanate ($Li_4Ti_5O_{12}$),[7, 8] and titanium oxide (TiO_2),[9] possess higher lithium-intercalation potentials and packing densities, which are of great interest of lithium-ion battery applications. Niobium pentoxide (Nb_2O_5), in particular, has a comparable working potential (~1.5 V *vs.* Li^+/Li) to titanium-based oxides and reasonable specific capacity (~ 201 mA h g^{-1}),[10-12] which makes it a highly promising material candidate. The implementation of Nb_2O_5-based electrode, however, has been intrinsically limited by its poor electric conductivity ($\sigma \sim 3\times10^{-6}$ S cm^{-1})[13] and slow ion diffusion, which results in low rate performance. Moreover, the capacity decay caused by volume expansion[14] during lithiation also brings certain concerns on its cycle life in practical application.

To date, several methods have been explored to improve the rate capability of Nb_2O_5, most of which mainly focus on forming effective path for ion migration or building network for electron transportation.[15, 16] The first approach involves the formation of mesoporous

Nb_2O_5 thin film on conductive substrates.[17] Compared with the bulk counterpart, such a thin film reduces the resistance for both electron and ion transport, leading to an outstanding rate performance. However, low mass loading of the active material results in low energy density. The second approach relies on combining Nb_2O_5 nanoparticles with conductive agents (e.g., carbon black[10] and carbon nanotubes[18]). Although the conductive agents form a continuous conductive network while the nanoparticles shorten the ion-diffusion pathway, the Nb_2O_5/carbon interface may be destructed easily during charge-discharge process, which results in poor cycling life. On the other hand, it has also been reported that doping Nb_2O_5 with other elements or forming Nb_2O_5-based solid solutions can improve either the rate capability or the cyclability of Nb_2O_5.[19, 20] Compared with pure Nb_2O_5, the introduction of foreign atoms changes the local structure and electronic property around Nb atoms.[21] For example, the conductivity of Cs-doped Nb_2O_5[22] can be increased to 10^{-5} S cm^{-1}, while Ta-doped Nb_2O_5[20] shows a superior stability. Recently, Goodenough group utilized $TiNb_2O_7$ solid solution with much higher reversible specific capacity (~285 mA h g^{-1}) as anode material.[12, 23] The rate performance, however, is still not satisfactory unless extra carbon coating is adopted.

Herein, we report a synthesis of Nb_2O_5–based nanocomposites with significantly improved rate performance and cycling stability using a facile sol-gel process. By introducing vanadium (V) into Nb_2O_5, the rate performance was greatly improved. Furthermore, such composite electrodes show enhanced cycling stability, which cannot be reached in Nb-doped V_2O_5 composites.[24] Possible synergistic mechanism between the constituent components of the nanocomposites that leads to such rate and cyclic stability were also proposed. This work provides a new material design concept towards better electrode materials with improved energy and power density.

7.2. Results and discussion

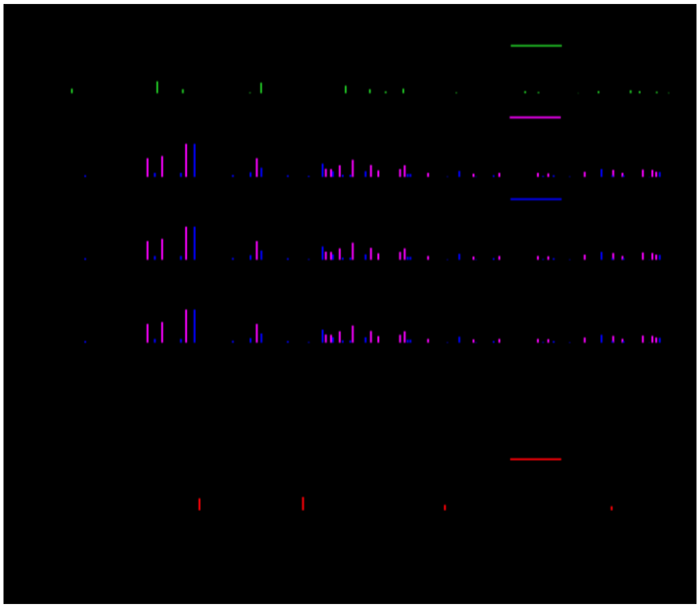

Figure 7.1 XRD patterns of as-synthesized Nb_2O_5, V_2O_5, and nanocomposites with different V compositions.

Figure 1 shows the X-ray diffraction (XRD) patterns of as-synthesized Nb_2O_5, V_2O_5, and Nb_2O_5-based composites. The pure Nb_2O_5 (**Fig.1**, bottom curve) exhibits a highly crystalline structure (pseudo-hexagonal structure, JCPDS No. 07-0061),[25] while the patterns of the V_2O_5 (**Fig.1**, top curve) could be indexed to an orthorhombic phase (JCPDS No.09-0387). The diffraction patterns of the VNb composites suggest that they are composed of Nb_2O_5 and solid solutions of $NbVO_5$ (orthorhombic structure, JCPDS No. 46-0046) and $Nb_{18}V_4O_{55}$ (orthorhombic structure, JCPDS No. 46-0087) (see **Fig.2**), with no obvious indications of V_2O_5 or other impurities. More specifically, Nb_2O_5 is the dominant phase in VNb-2 and VNb-10. The content of the solid solutions increases with increasing V content, accompanying by decreasing Nb_2O_5 content. For VNb-30, nearly all of the Nb_2O_5 is present in the form of solid solutions. Moreover, a slight shift of (001) peak from Nb_2O_5 can be observed with increasing V content, indicating an increase in lattice spacing. This phenomenon is also reported in reference,[26] which is attributed to a certain amount of V atoms doping into Nb_2O_5 crystal structure, rather than partial replacement of Nb atoms with V atoms.

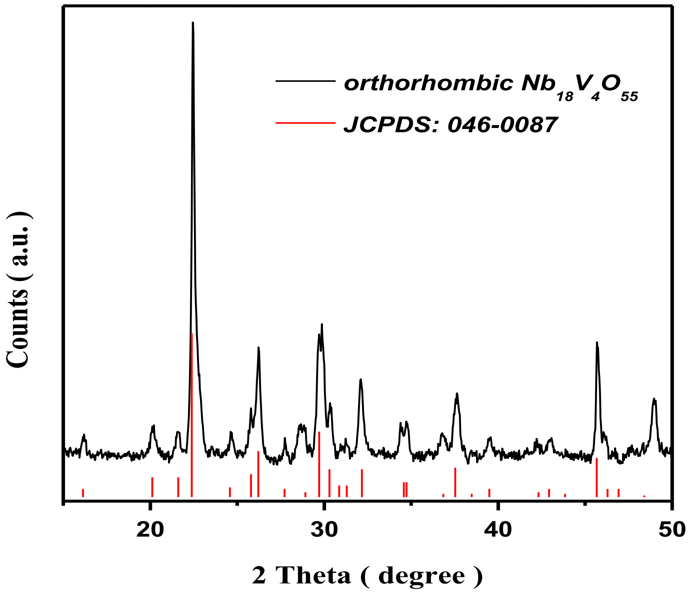

Figure 7.2 XRD pattern of as-synthesized $Nb_{18}V_4O_{55}$ an orthorhombic structure (JCPDS No. 46-0087).

The morphology of the composites was characterized by SEM (see **Fig.3 and Fig.4**). **Figure 3** shows the representative low and high magnification SEM images of the pure Nb_2O_5, pure V_2O_5 and VNb-10. Homogeneous particle morphology can be observed for the pure Nb_2O_5 (**Fig.3, (a) and (b)**) with particles size varying around tens of nanometers with agglomeration. The V_2O_5 are found to be bar-like crystals of submicron size (**Fig.3, (e) and (f)**). Particulate morphology with agglomeration is maintained for composite VNb-10, as shown in **Figure 3, (c) and (d)**. The particle sizes fall between Nb_2O_5 and V_2O_5, implying the interactively restraining during the formation of nanocomposite. This size-increase trend is also found in all composites (see **Fig.3**), as increasing the vanadium composition, reflecting the increase in crystallinity, which is confirmed by XRD results.

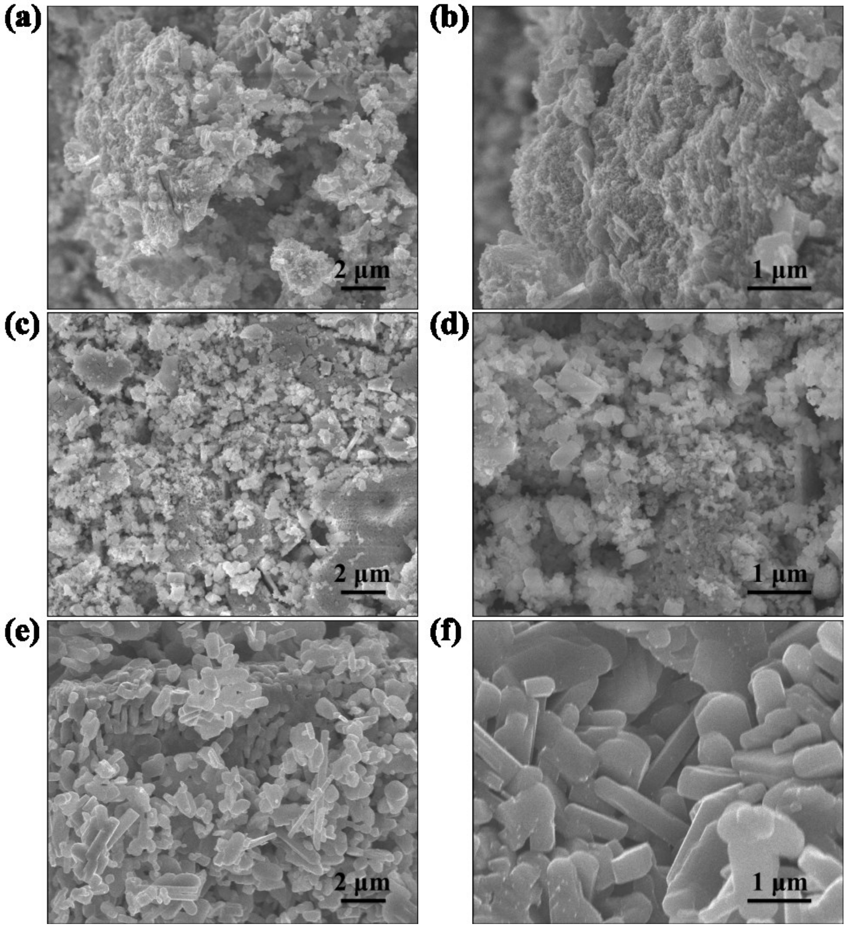

Figure 7.3 Low- and high-resolution SEM images of the as-synthesized (a), (b) Nb_2O_5 and (c), (d) V_2O_5 and (e), (f) VNb-10.

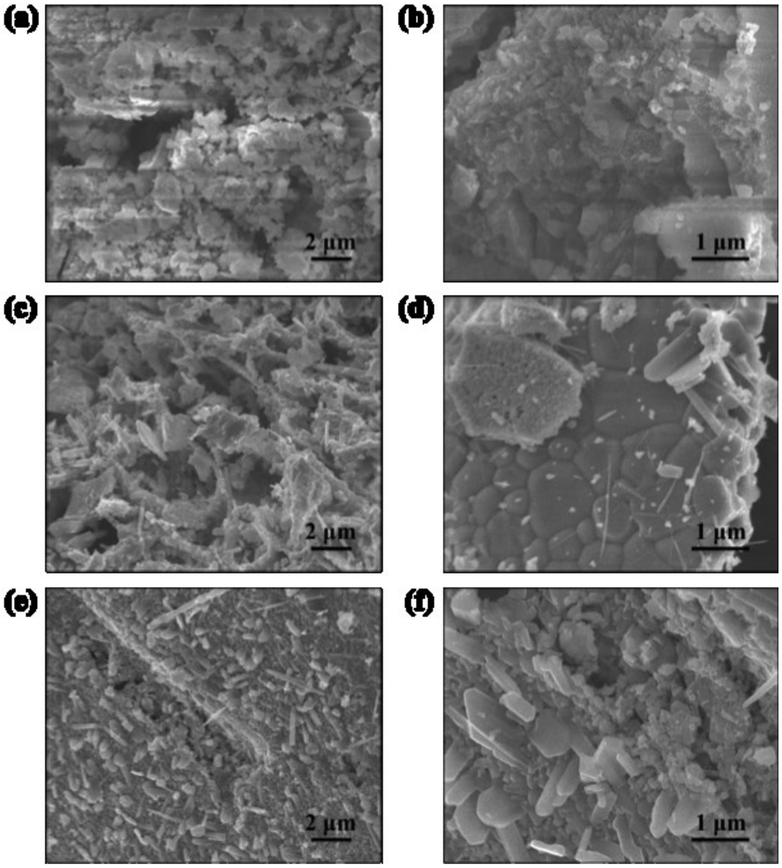

Figure 7.4 Low- and high-resolution SEM images of the as-synthesized (a), (b) VNb-2, (c), (d) VNb-20, and (e), (f) VNb-30.

TEM images also confirm the shape and size of the crystals. As shown in **Figure 5**, the Nb_2O_5 particles have an average size of around 40 nm with agglomeration; the V_2O_5 bars are 300 ~ 400 nm in diameter and around 1 μm in length. The high-resolution images show high crystalline feature of the pure compounds, as well as the composites (**Fig.5, (c) and (d); Fig.6**).

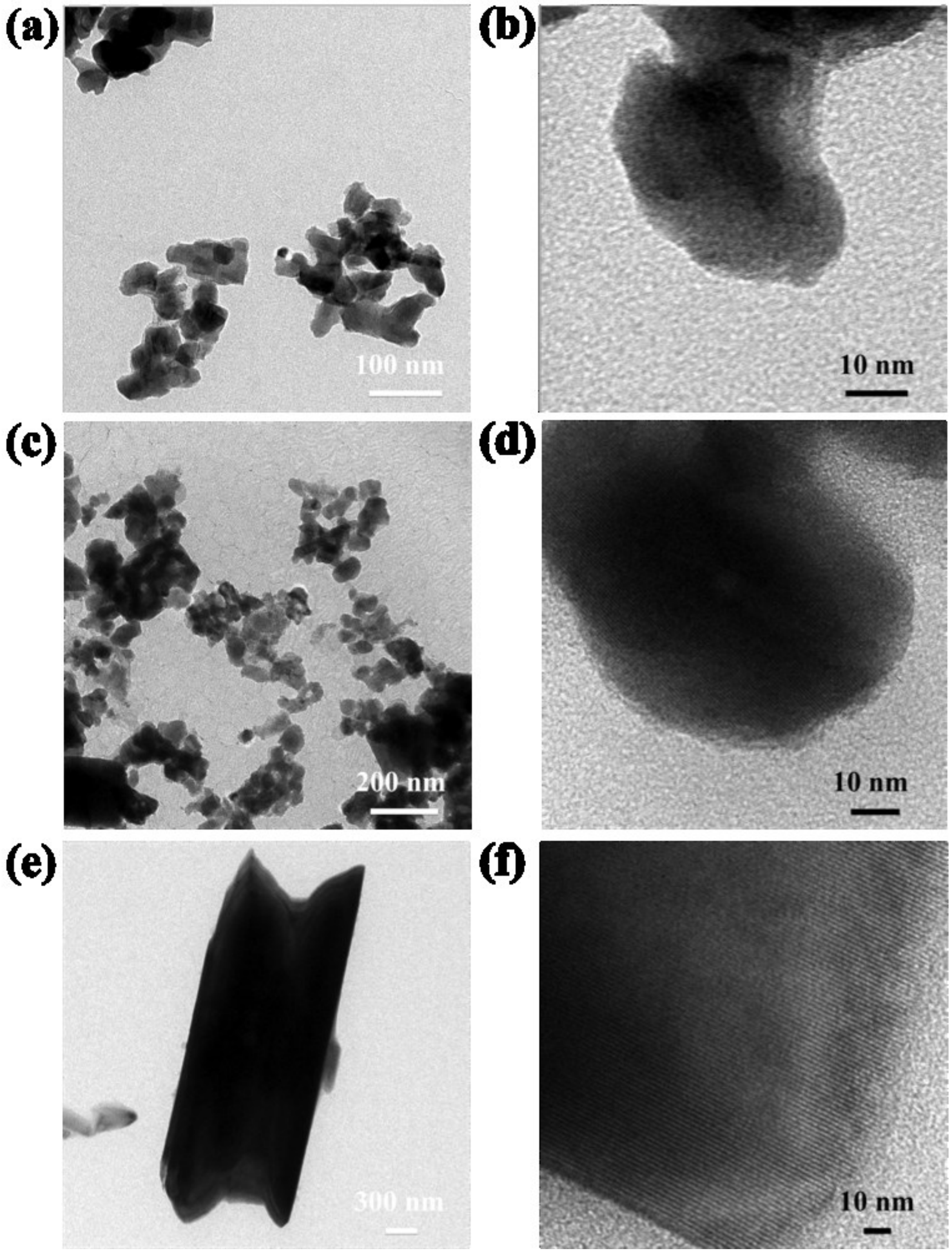

Figure 7.5 Low- and high-resolution TEM images of the as-synthesized (a), (b) Nb_2O_5 and (c), (d) VNb-10 and (e), (f) V_2O_5.

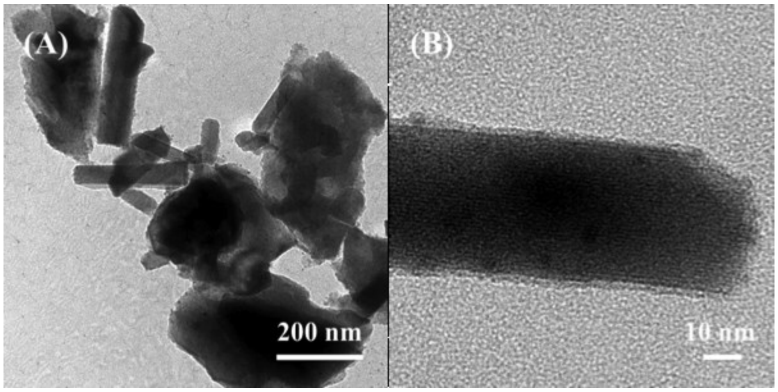

Figure 7.6 (A) Low- and (B) high-resolution TEM image of the as-synthesized VNb-30.

Electrochemical behavior of the samples was examined using cyclic voltammetric (CV) measurements. Generally, electrochemical Li^+ insertion in Nb_2O_5 can be described by $Nb_2O_5 + xLi^+ + xe^- \leftrightarrow Li_xNb_2O_5$.[14, 27, 28] **Figure 7** compares the first- and second- cycle CV curves of Nb_2O_5, V_2O_5 and VNb-10 normalized with respect to the active mass using a sweeping rate of 0.2 mV s^{-1} at room temperature. The Nb_2O_5 shows two distinct anodic peaks located at potential of 1.75 and 1.45 V, where the reduction of Nb_2O_5 from Nb^{5+} to Nb^{4+} by two Li^+ ions occurs at two lithium-intercalation sites with different reaction energies. In contrast, a broad cathodic peak can be observed in the Li^+ de-intercalation process, showing that lithium extraction takes place at sites of a wide distribution of energies.[13] Compared with Nb_2O_5, V_2O_5 often works at high potential as a LIB cathode.[29] Within this potential region, it shows two sharp anodic peaks at around 2.12 and 1.70 V for the first cycle (**Fig.7A**), corresponding to the formation of γ-$Li_2V_2O_5$ and ω-$Li_3V_2O_5$, respectively.[30, 31] These two peaks disappear in the second cycle (**Fig. 7B**), and the V_2O_5 shows a low capacity based on the area under the CV curve, which is consistent with the irreversible Li^+ insertion/de-insertion into ω-$Li_3V_2O_5$.[31]

[redacted]

Figure 7.7 (A) First and (B) second cyclic voltammograms of electrodes made from Nb_2O_5, V_2O_5 and VNb-10 with a potential range of 3.0~1.0 V at potential scanning rate of 0.2 $mV \cdot s^{-1}$ at room temperature.

By comparison, VNb-10 exhibits a similar CV curve as that of the pure Nb_2O_5. However, the better-defined redox peaks at 1.65 and 1.82 V suggest a more pronounced redox capacity, which is further revealed in the galvanostatic cycling discussed below. Furthermore, the shift of the anodic and cathodic peaks to the lower and higher potentials, respectively, indicates a decreased electrode polarization. Note that no obvious redox peaks from V_2O_5 in VNb-10 could be observed, ruling out the formation of V_2O_5 phase, which agrees with the XRD result.

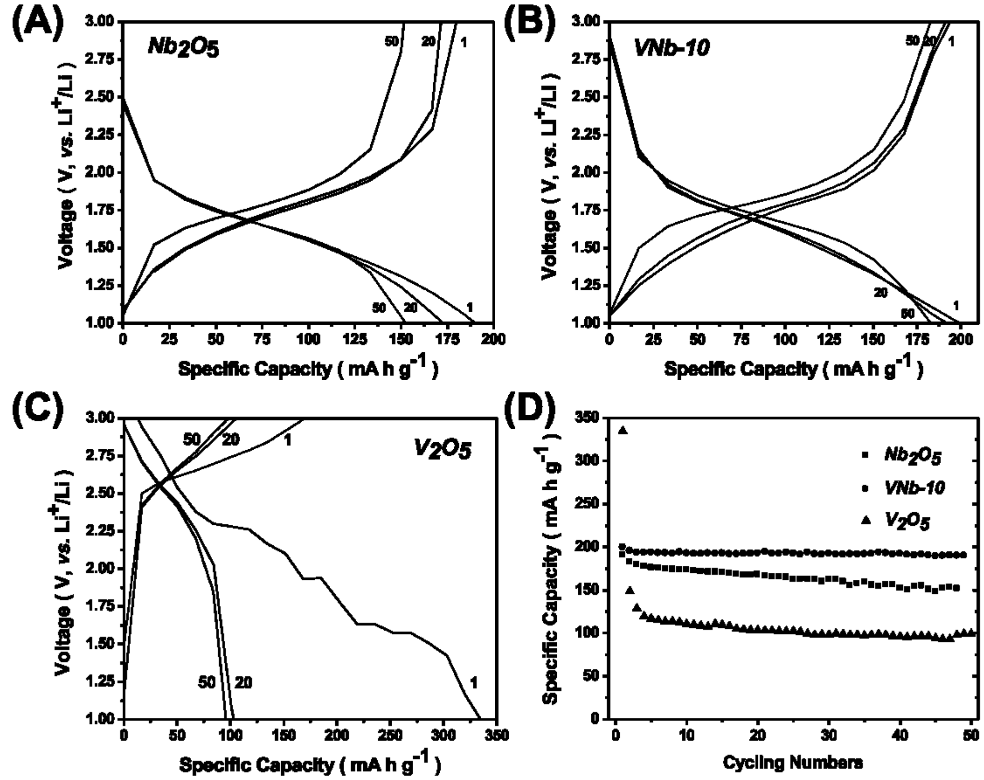

Figure 7.8 Galvanostatic charge-discharge profiles of (A) Nb_2O_5, (B) VNb-10, and (C) V_2O_5 at a current rate of 50 mA g^{-1} in the voltage range of 3.0~1.0 V at room temperature. The numbers indicate cycle number. (D) Comparison of cycling performance of Nb_2O_5, VNb-10, and V_2O_5 at a current density of 50 mA g^{-1} in the voltage range of 3.0~1.0 V at room temperature.

Figure 8 shows the representative galvanostatic charge-discharge profiles of the Nb_2O_5, V_2O_5, and VNb-10 at different cycle numbers in the voltage range of 3.0~1.0 V. The first discharge curve of Nb_2O_5 exhibits a slope curve, indicating a reversible lithium intercalation-type electrochemical single-phase reaction.[13] The specific capacity is 191 mA h g^{-1}, corresponding to 1.9 mol of Li^+ intercalating into one mole of Nb_2O_5, and remains 172 mA h g^{-1} after 20 cycles (**Fig.8A**). The V_2O_5 exhibits a high initial specific capacity of 335 mA h g^{-1}; however, it dramatically decreases during cycling (**Fig.8C**) due to large irreversible structure change.[32, 33] By comparison, all VNb nanocomposites shows similar discharge profiles to that of Nb_2O_5 (**Fig.9A, B and C**). As shown in **Figure 8B**, VNb-10 possesses an initial capacity of 200 mA h g^{-1}, and well maintains during the following cycling (~190 mA h g^{-1} after

20 cycles). Such a difference of cycling stability is further shown in **Figure 8D**. Both Nb_2O_5 and V_2O_5 have pronounced capacity decay after 50 cycles; V_2O_5, in particularly, shows dramatic capacity decrease after the initial cycle, which is consistent with the CV measurement. Compared with Nb_2O_5 and V_2O_5, VNb-10 shows significantly improved cycling stability. Even after 50 cycles, the VNb-10 electrode still remains 95% of its initial capacity. Interestingly, all VNb composites electrodes show improved cycling stability (see **Fig.9D**), except that VNb-30 shows more dramatic capacity drop after the initial cycle.

Figure 7.9 Galvanostatic charge-discharge profiles of (A) VNb-2, (B) VNb-20, and (C) VNb-30 at a current rate of 50 mA g^{-1} in the voltage range of 3.0~1.0 V at room temperature. The numbers indicate cycle number. (D) Comparison of cycling performance of VNb-2, VNb-20, and VNb-30 at a current density of 50 mA g^{-1} in the voltage range of 3.0~1.0 V at room temperature.

In addition to the enhanced cycling stability, the VNb composites electrodes also show outstanding rate capability. **Figure 10** compares the rate performance of the electrodes of Nb_2O_5, V_2O_5 and VNb-10. As expected, both Nb_2O_5 and V_2O_5 electrodes exhibit moderate rate capability, which is attributed to their intrinsically poor electron conductivities and slow ion mobility. Introducing vanadium into Nb_2O_5 system leads to a dramatic enhancement of the rate capability. As shown in **Fig.10**, the capacity retention of VNb-10 at 5 C-rate (1 A g^{-1}) in comparison to that at 0.25 C-rate (50 mA g^{-1}) is around 50%. Even at a higher C-rate (2 A g^{-1}), VNb-10 still possesses a capacity of 65 mA h g^{-1}, which is comparable to those carbon-based Nb_2O_5 composite materials,[18] but with much higher volumetric energy density. Such a superior rate capability can be observed for all VNb composites electrodes, except that VNb-30 only shows a moderate improvement (Fig.S3†).

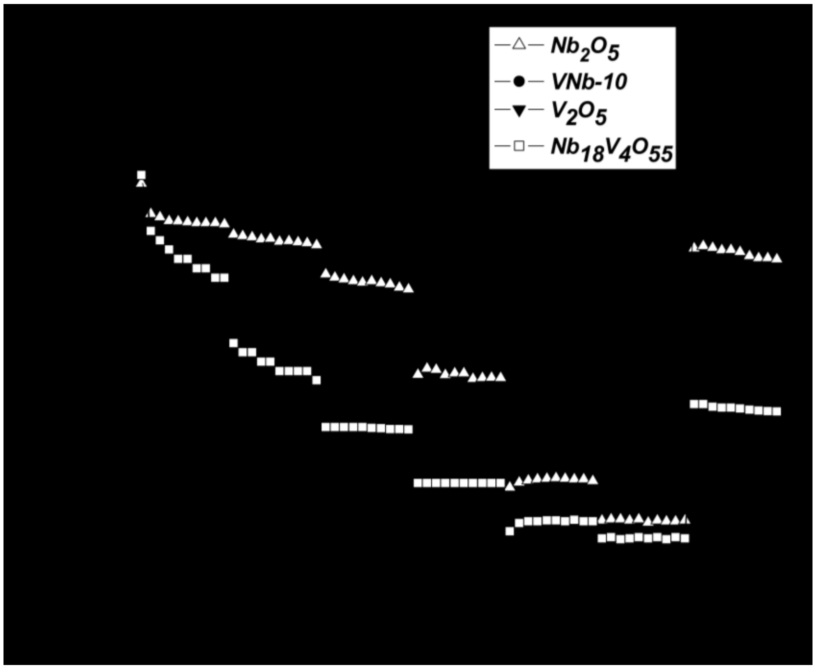

Figure 7.10 Rate performance of the electrodes based on Nb_2O_5, VNb-10, and V_2O_5 over multiple current densities in the voltage range of 3.0~1.0 V at room temperature.

It is essential to probe the mechanism leading to the outstanding rate performance and cyclic stability observed in such composites. As mentioned above, such VNb composites are consisted of Nb_2O_5 and solid solutions of $Nb_{18}V_4O_{55}$ and $NbVO_5$. Thus, it is necessary to distinguish the contribution from each component. Towards this aim, pure solid solutions were synthesized. It was found that $Nb_{18}V_4O_{55}$ could be formed with a Nb/V molar ratio of 9:2

following the same procedure as VNb composites but a longer reaction time of 12 hours (**Fig.2**). As shown in **Figure 10**, the specific capacity of $Nb_{18}V_4O_{55}$ decreases dramatically with increasing the current density. For example, at 200 mA g^{-1}, the capacity is around 70 mA h g^{-1}, only 35% of the initial capacity of 199 mA h g^{-1} at a current density of 50 mA g^{-1}, showing that the rate performance is only moderate and comparable with that of V_2O_5. On the other hand, the synthesis of $NbVO_5$ could not be achieved using such a sol-gel process, we noticed that VNb-30 contains the highest ratio of $NbVO_5$ among the composites, but only shows a moderate rate capability (**Fig.11**), indicating a poor rate performance of $NbVO_5$. Other approaches have been reported to synthesize $NbVO_5$,[34-36] however, the good rate capability was not found.

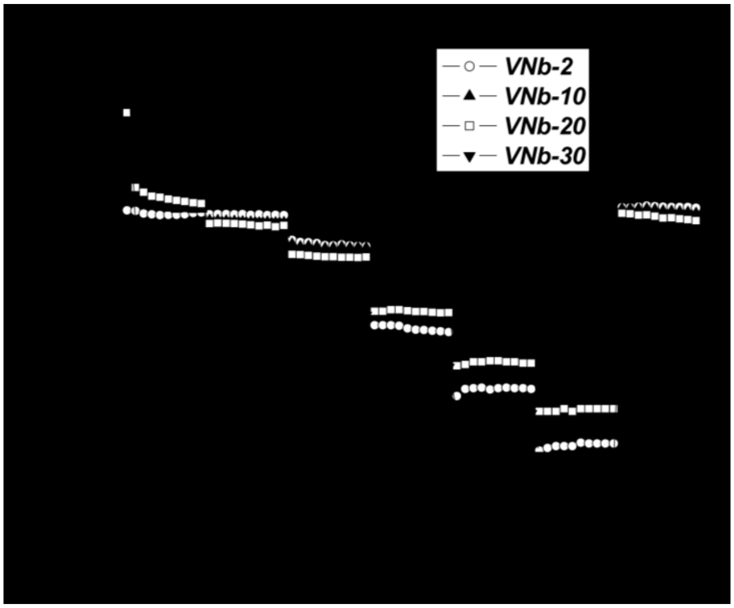

Figure 7.11 Comparison of rate performance of the electrodes based on VNb-2, VNb-20, and VNb-30 over multiple current densities in the voltage range of 3.0~1.0 V at room temperature.

We believe that the improvement in both rate capability and stability observed for VNb composites is mainly attributed to the synergistic effect between Nb_2O_5 and the solid solution constituents. It has been reported that reduced domain size in nanocomposite, as well as improved intimate contact between grains boundaries facilitate Li^+ diffusion and charge transfer.[37, 38] It is found that the domain sizes of Nb_2O_5 in VNb-10 and VNb-20 are ~19.1

and ~15.4 nm, respectively, estimated from the Scherrer's equation, which is smaller than that of Nb_2O_5 of ~30 nm. Furthermore, note that such nanocomposites were formed during a sol-gel process, where homogenous amorphous constituents are gradually converted into the nanocrystalline composites in a subsequent heating process. During this process, continuous reaction between the niobium- and the vanadium- constituents builds intimate contacts between the domains of Nb_2O_5 and the solid solutions. Besides, such a synthesis process also creates a large number of local disorders enhancing charge transfer of the resultant composites. However, with increasing the vanadium content, as-formed nanocomposites mainly contain solid solutions with larger grain size. For example, VNb-30 shows an average domain size of ~33.7 nm according to the Scherrer's equation, which may result in deteriorated rate performance and capacity stability.

7.3. Conclusion

In summary, Nb_2O_5-based nanocomposites with various niobium and vanadium contents were synthesized using a simple sol-gel process, and applied to anode materials of lithium-ion batteries with outstanding rate capability and enhanced cycling performance. The improved conductivity and stability mainly arise from the introduction of V atoms into Nb_2O_5 system and the synergistic effect between the Nb_2O_5 and the two solid solutions. In addition, such composites of transition metal oxides possesses a high packing density, thus ensures a high volumetric energy density of a device based on the composite electrode.

7.4. Experimental Section

Synthesis and Characterization of Nb_2O_5 nanocomposites: a simple sol-gel technique was applied to synthesize the Nb_2O_5-based nanocomposites. In a typical synthesis, ammonium niobate (V) oxalate hydrate (3.26 mmol, 0. 989 g) and ammonium metavanadate (0.52 mmol, 0.610 g) were dissolved in DI-water (30 mL) under ultrasonication for 30 minutes, followed by adding HCl solution (2.0 M, 0.5 mL) under stirring. The clear and transparent solution was transferred to a petri-dish and kept overnight at room temperature to allow the evaporation of the solvent. The colorless gel was then sintered at 550 °C in air for 5 hours with a ramp rate of 1 °C min^{-1} from room temperature to 350 °C, and 5 °C min^{-1} from 350 to 550 °C. The product was then collected and denoted as VNb-*X*, where *X* corresponds to the weight percentage of V_2O_5 in the whole composite. The pure V_2O_5 and Nb_2O_5, and composites with different ratios were also synthesized following the same procedure. The color of the composites is from white to yellow-brown with increasing the V_2O_5 content.

X-ray diffraction (XRD) experiments were conducted on a X'Pert Pro X-ray diffractometer (Panalytical B.V.); scanning electron microscopic (SEM) experiments were conducted on a JEOL JSM-6700 FE-SEM (JEOL); transmission electron microscopic (TEM) experiments were conducted on a Philips CM120 operated at 120 kV (Philips/FEI).

Electrode Fabrication and Characterization: A certain amount of the composite was dispersed in *N*-methylpyrrolidinone (NMP) by ultrasonication and stirring to form homogeneous and stable slurries, where 10 wt-% poly(vinylidene fluoride) (PVDF) and 10 wt-% carbon black were also added. The composites electrodes were prepared by coating the slurries onto nickel foil current collector and dried at 100 °C overnight. The mass loading was controlled to be ~5 mg cm^{-2} on each current collector.

Cyclic voltammetry measurements were carried out on a VMP3 potentiostat/galvanostat (Bio-Logic LLC, Knoxville, TN). $LiClO_4$ in propylene carbonate (PC) (1 M) was used as the electrolyte, and lithium foils were used as both the counter and reference electrodes. Cyclic voltammetric (CV) measurements were carried out in an argon-filled glove box using cutoff voltages of 3.0 and 1.0 V versus Li^+/Li at different scan rates. The charge and discharge measurements were carried out on standard 2032-type coin cells by LAND CT2000 (Wuhan Jinnuo Electronics, Ltd., Wuhan, China) at different current densities. The cells were assembled in a glovebox under an argon atmosphere, where 1 M $LiPF_6$ in EC/DMC (1:1) was used as the electrolyte. Electrochemical impedance spectroscopy (EIS) tests were carried out on a Solartron 1860/1287 Electrochemical Interface.

References

[1] B.E. Conway, Journal of The Electrochemical Society, 138 (1991) 1539-1548.

[2] J.M. Tarascon, M. Armand, Nature, 414 (2001) 359-367.

[3] A.S. Arico, P. Bruce, B. Scrosati, J.-M. Tarascon, W. van Schalkwijk, Nat Mater, 4 (2005) 366-377.

[4] M. Winter, R.J. Brodd, Chemical Reviews, 104 (2004) 4245-4270.

[5] P.G. Bruce, B. Scrosati, J.-M. Tarascon, Angewandte Chemie International Edition, 47 (2008) 2930-2946.

[6] Y.-G. Guo, J.-S. Hu, L.-J. Wan, Advanced Materials, 20 (2008) 2878-2887.

[7] S.-H. Kang, D.P. Abraham, W.-S. Yoon, K.-W. Nam, X.-Q. Yang, Electrochimica Acta, 54 (2008) 684-689.

[8] H.-G. Jung, S.-T. Myung, C.S. Yoon, S.-B. Son, K.H. Oh, K. Amine, B. Scrosati, Y.-K. Sun, Energy & Environmental Science, 4 (2011) 1345-1351.

[9] K. Saravanan, K. Ananthanarayanan, P. Balaya, Energy & Environmental Science, 3 (2010) 939-948.

[10] M. Wei, K. Wei, M. Ichihara, H. Zhou, Electrochemistry Communications, 10 (2008)

980-983.

[11] J.-T. Han, D.-Q. Liu, S.-H. Song, Y. Kim, J.B. Goodenough, Chemistry of Materials, 21 (2009) 4753-4755.

[12] J.-T. Han, Y.-H. Huang, J.B. Goodenough, Chemistry of Materials, 23 (2011) 2027-2029.

[13] A.L. Viet, M.V. Reddy, R. Jose, B.V.R. Chowdari, S. Ramakrishna, The Journal of Physical Chemistry C, 114 (2009) 664-671.

[14] R. Kodama, Y. Terada, I. Nakai, S. Komaba, N. Kumagai, Journal of The Electrochemical Society, 153 (2006) A583-A588.

[15] J.Z. Ou, R.A. Rani, M.-H. Ham, M.R. Field, Y. Zhang, H. Zheng, P. Reece, S. Zhuiykov, S. Sriram, M. Bhaskaran, R.B. Kaner, K. Kalantar-zadeh, ACS Nano, 6 (2012) 4045-4053.

[16] K. Lee, Y. Yang, M. Yang, P. Schmuki, Chemistry – A European Journal, 18 (2012) 9521-9524.

[17] K. Brezesinski, J. Wang, J. Haetge, C. Reitz, S.O. Steinmueller, S.H. Tolbert, B.M. Smarsly, B. Dunn, T. Brezesinski, Journal of the American Chemical Society, 132 (2010) 6982-6990.

[18] X. Wang, G. Li, Z. Chen, V. Augustyn, X. Ma, G. Wang, B. Dunn, Y. Lu, Advanced Energy Materials, 1 (2011) 1089-1093.

[19] X. Lu, Z. Jian, Z. Fang, L. Gu, Y.-S. Hu, W. Chen, Z. Wang, L. Chen, Energy & Environmental Science, 4 (2011) 2638-2644.

[20] A. Le Viet, M.V. Reddy, R. Jose, B.V.R. Chowdari, S. Ramakrishna, Electrochimica Acta, 56 (2011) 1518-1528.

[21] A.V. Rosario, E.C. Pereira, Electrochimica Acta, 46 (2001) 1905-1910.

[22] E.P. Kharitonova, V.I. Voronkova, V.K. Yanovskii, S.Y. Stefanovich, Journal of Crystal Growth, 237-239, Part 1 (2002) 703-706.

[23] J.-T. Han, J.B. Goodenough, Chemistry of Materials, 23 (2011) 3404-3407.

[24] A. Sakunthala, M.V. Reddy, S. Selvasekarapandian, B.V.R. Chowdari, P.C. Selvin, Energy & Environmental Science, 4 (2011) 1712-1725.

[25] N. Noma, M. Hamano, Journal of Sol-Gel Science and Technology, 64 (2012) 297-303.

[26] K. V. R. Chary, G. Kishan, T. Bhaskar, Chemical Communications, (1999) 1399-1400.

[27] N. Ozer, D.-G. Chen, C.M. Lampert, Thin Solid Films, 277 (1996) 162-168.

[28] M.A.B. Gomes, L.O. de Sousa Bulhoes, Electrochimica Acta, 35 (1990) 765-768.

[29] P. Liu, S.H. Lee, C.E. Tracy, Y. Yan, J.A. Turner, Advanced Materials, 14 (2002) 27-30.

[30] J. Galy, Journal of Solid State Chemistry, 100 (1992) 229-245.

[31] C. Delmas, H. Cognac-Auradou, J.M. Cocciantelli, M. Menetrier, J.P. Doumerc, Solid State Ionics, 69 (1994) 257-264.

[32] S. Wang, Z. Lu, D. Wang, C. Li, C. Chen, Y. Yin, Journal of Materials Chemistry, 21 (2011) 6365-6369.

[33] Y. Liu, M. Clark, Q. Zhang, D. Yu, D. Liu, J. Liu, G. Cao, Advanced Energy Materials, 1 (2011) 194-202.

[34] N. Krins, J.D. Bass, D. Grosso, C. Henrist, R. Delaigle, E.M. Gaigneaux, R. Cloots, B. Vertruyen, C. Sanchez, Chemistry of Materials, 23 (2011) 4124-4131.

[35] N. Krins, L. Lepot, R. Cloots, B. Vertruyen, Solid State Ionics, 180 (2009) 848-852.

[36] J. Wang, J. Deng, R. Yu, J. Chen, X. Xing, Dalton Transactions, 40 (2011) 3394-3397.

[37] K. Lee, G. Cao, The Journal of Physical Chemistry B, 109 (2005) 11880-11885.

[38] D. Liu, G. Cao, Energy & Environmental Science, 3 (2010) 1218-1237.

8. Conclusion

Energy storage performance of current batteries and ECs are constrained by poor material properties. The work in this dissertation is to address the limitation of current energy storage materials by rational structure designs according to well-recognized principles and criteria. The overall research strategy is to design and fabricate multifunctional architectures by integrating distinct material structures and properties to create a new family of high-performance energy materials with desired performance.

Different types of energy storage architectures were investigated and compared with conventional structures to demonstrate such design concepts. First, Nb_2O_5 nanocrystals with low dimensions were synthesized, and Nb_2O_5/CNTs nanocomposites electrode architecture was designed and fabricated by a physically mixing method. By comparison with pure Nb_2O_5 materials, it was found that such architecture could create more accessible outer surface, which was very important in fast lithium storage. Synergistic effects obtained between Nb_2O_5 nanocrystals and CNTs resulted in an optimal composition with the highest storage performance. Secondly, to eliminate the contact resistance resulting from aggregation of nanocrystals and to further enhancing the electrode stability, an *in-situ* growth of Nb_2O_5 nanocrystals on the CNTs framework was also developed to ensure the intimate contact between the two components. Compared with physically mixed composites electrode, such an electrode architecture showed superior cycling stability, while the excellent rate performance and high specific capacitance remained. Thirdly, various architectures were designed and fabricated using ultrafine $LiMn_2O_4$ nanocrystals as a model system. Electrodes were fabricated by directly coating thin film $LiMn_2O_4$ on conductive Indium-Tin-Oxide (ITO) glass, and by conformably coating nanocrystals on pre-formed CNT papers. Last, electrode architecture obtained by integrating nanocrystals and highly conductive graphene sheets was also designed and fabricated through an aerosol-assisted process using $Li_4Ti_5O_{12}$ nanocrystals as a model system. The pomegranate-like architecture enables the electrode with outstanding rate capability, as well as good electrode stability. It was demonstrated that thick electrodes with high charge capacity, high rate performance and cycling stability rely on functional architecture that simultaneously provides high electronic conductivity, easy ion diffusion, abundant surface active sites and robust structure and interfaces.

The general conclusion derived from these studies is that the energy storage performance of electrode materials can be significantly improved by constructing rational architectures that provide effective ion diffusion, good electronic conductivity, fast electrode reaction, robust structure and a stable interface, which normally cannot be obtained with conventional materials. This strategy also can be extended to other devices, such as batteries and fuel cells, providing a general design platform for high performance energy materials. Further exploration in this research direction will ultimately lead to high energy, high power, and long life energy storage devices for many applications, including portable electronics, EVs and grid-scale energy storage.